UNIVERSITY OF OKLAHOMA

GRADUATE COLLEGE

# AFRICAN EASTERLY WAVE TRACKS AS SIMULATED BY CMIP5 MODELS

A THESIS

SUBMITTED TO THE GRADUATE FACULTY

in partial fulfillment of the requirements for the

Degree of

MASTER OF SCIENCE IN METEOROLOGY

By

ALLISON LYNN BRANNAN
Norman, Oklahoma
2017

Downloaded from SHAREOK. Persistent Handle URL: https://hdl.handle.net/11244/51838

AFRICAN EASTERLY WAVE TRACKS AS SIMULATED BY CMIP5 MODELS

A THESIS APPROVED FOR THE
SCHOOL OF METEOROLOGY

BY

Dr. Elinor Martin, Chair

Dr. Jason Furtado

Dr. Xuguang Wang

© Copyright by ALLISON LYNN BRANNAN 2017
All Rights Reserved.

# Acknowledgments

The completion of this study, along with my master's degree, would not have been possible without the support of my advisor, my colleagues, and my family and friends. I extend many thanks to Dr. Elinor Martin for broadening my horizons to a new aspect of tropical meteorology. Thank you for giving me creative freedom to shape a project I was excited about while also challenging me to become a better scientific thinker. Thank you to my committee, Dr. Jason Furtado and Dr. Xuguang Wang for the advice and suggestions in finishing and polishing this work. This study would have not been possible without the help from Alan Brammer and Shawn Riley. Thank you Alan for working with me to adapt this tracking algorithm to use within climate models. And Shawn, I am sorry I always came to you with the most annoying computer problems— thank you for also being so patient and working to solve them.

I also must thank the School of Meteorology for funding this project, especially Dr. Parsons who persistently emailed and called me until I decided to commit to undertaking the master's program at the University of Oklahoma. Thank you to Christie Upchurch who works out every glitch in registration and orientation and is always happy to listen to any problem and respond in such a caring manner. I cannot express enough gratitude towards Veronica Fall. It has been such a privilege to be in the same research group. Thank you for passing down your wisdom in the form of ideas, class notes, flashcards, and especially LaTex guidance.

I would also like to thank the University of Oklahoma's gymnastics program—specifically Taqiy Abdullah-Simmons, John DeJulio, and Riley Adams for welcoming me into the gym. The everyday stress of school and research could only be offset by a few hours dedicated to being upside down. Thanks for all the encouragement and thanks for picking me up when I fell.

Thank you to my friends. I never imagined I would get as close to people in two years as I did with Kenzie Krocak, Matt Flournoy, Josh Gebauer, and Sarah Borg. The Friday nights at the Mont and the endless rounds of card games never ceased to cleanse my mind and rejuvenate me for the next week. You are amazing friends and amazing scientists that I will always look up to. Jackson Anthony, I cannot thank you enough for always being by my side. Thank you for putting up with my stressful nights and bringing out my inner smile and silly dance moves. Also, thank you all so much for taking care of me when I was broken. Your kindness in driving me to doctor's appointments, pushing my grocery cart, and helping me re-learn to walk is priceless.

Finally, thank you to my family— mom, dad, and Daniel. Thanks for believing in me and encouraging me to chase my dreams, but always welcoming me back to Florida with a boat ride and a key lime pie.

# Table of Contents

**Acknowledgments** **iv**

**List of Tables** **viii**

**List of Figures** **ix**

**Abstract** **xviii**

**1 Introduction and Background** **1**

1.1 African Easterly Wave Genesis . . . . . 2

1.2 African Easterly Wave Characteristics . . . . . 5

1.3 African Easterly Waves within Global Climate Models . . . . . 9

1.4 Research Goal . . . . . 13

**2 Data and Methodology** **15**

2.1 Data . . . . . 15

2.2 African Easterly Wave Identification Techniques . . . . . 18

2.2.1 Objective Tracking . . . . . 19

**3 Results** **23**

3.1 African Easterly Jet . . . . . 23

3.2 Historical Simulations of African Easterly Waves . . . . . 26

3.2.1 Frequency . . . . . 26
3.2.2 Track Characteristics . . . . . 30
3.2.3 Intensity . . . . . 38
3.3 Accumulated Historical Biases . . . . . 44
3.4 Future Simulations of African Easterly Waves . . . . . 50
3.4.1 Frequency . . . . . 50
3.4.2 Track Characteristics . . . . . 56
3.4.3 Intensity . . . . . 60

**4 Summary and Conclusions** **70**

**Reference List** **76**

**Appendices** **82**

**A Sensitivity Tests for Objective Tracking Algorithm** **83**

**B Net Longitude Distance** **86**

**C Monthly Distribution of Average CV** **87**

**D Distribution of Future AEW Characteristics** **88**

# List of Tables

2.1 List of CMIP5 models used in this study, including their horizontal resolution. Only one ensemble member was used for each model. . . 16

3.1 Average frequency of northern track AEWs during the historical and future periods for each model along with the raw difference (future − historical) and the percent change. . . . . 52

3.2 As in Table 3.1, but for southern track AEWs. . . . . 53

3.3 Average CV (x$10^{-5}$ $s^{-1}$) of northern track AEWs during the historical and future periods for each model along with the raw difference (future − historical) and the percent change. . . . . 62

3.4 As in Table 3.3, but for southern track AEWs. . . . . 63

3.5 Average maximum CV (x$10^{-5}$ $s^{-1}$) of northern track AEWs during the historical and future periods for each model along with the raw difference (future − historical) and the percent change. . . . . 64

3.6 As in Table 3.5, but for southern track AEWs. . . . . 65

# List of Figures

1.1 Topography (contours) of the African domain utilized in this study from the ETOPO2v2 dataset (National Geophysical Data Center, 2006). . . . . 3

2.1 Average spectrum of daily mean meridional wind for the summer months (June-September) of 1980-2000, for a region concentrated over the African continent (between 0°N-30°N and 20°W-40°E). The red line is a marker for a 6-day period. The smooth lines represent the 95% confidence interval with the solid line showing the mean power and the dotted lines representing the upper and lower 2.5% bounds. . . . . 19

2.2 Hovmöller of curvature vorticity contours (averaged between 0°N and 30°N) for the year 2000. Black lines are AEW tracks from the objective tracking method. Vertical grey line represents the approximate West African coastline. Blue symbol represents the genesis location of Hurricane Alberto from the IBTrACS dataset (Knapp et al., 2010). . . . . 20

2.3 Number of waves resolved by the objective tracking algorithm for six years between 1980 and 2000 using four different grid spacings of the JRA-55 reanalysis. . . . . 21

3.1 Latitude location of the AEJ by month for the historical period (a) and future − historical (b). The May-October average AEJ location is compared between the historical and future periods in (c) with the grey line representing a constant AEJ location, the black diamonds representing the average AEJ location in the reanalyses, and the star as the model mean. The patterned black lines (a) represent the reanalyses, the solid black line shows the model mean (a,b) and the colored lines (a,b) or dots (c) indicate individual models. Warm (cool) colors correspond to finer (coarser) resolution models. . . . . 24

3.2 The northern (southern) track AEWs will be identified throughout the latitude band represented by the solid (dotted) portion of the line corresponding to each colored model for the historical period (top) and for the future (bottom). The boundary between the solid and dotted line represents the average summertime location of the AEJ in each model. . . . . 25

3.3 Yearly frequency of AEWs (left column; a,c) and monthly frequency normalized by the total number of AEWs resolved by each model individually (right column; b,d) during the historical period (1980-2000). Northern track values are displayed in the top row (a,b) with southern track values on the bottom (c,d). Patterned black lines represent each reanalysis. Solid black line is the model mean. Colors are representative of each CMIP5 model with warm (cool) colors corresponding to finer (coarser) resolution models. . . . . 27

3.4 Box plots of the frequency of AEW genesis (left column; a,d), dissipation (middle column; b,e), and time duration (right column; c,f) in the CMIP5 models in each 5° longitude bin, normalized by the total number of AEWs resolved by each model individually during the historical period (1980-2000). Northern track values are displayed in the top row (a,b,c) with southern track values on the bottom (d,e,f). Diamond markers represent each reanalysis. . . . . 31

3.5 Frequency of the average speed of each AEW, normalized by the total number of AEWs resolved by each model individually during the historical period (1980-2000). Northern track values are displayed in (a) with southern track values in (b). Patterned black lines represent each reanalysis. Solid black line is the model mean. Colors are representative of each CMIP5 model with warm (cool) colors corresponding to finer (coarser) resolution models. . . . . 37

3.6 Frequency of the average CV (left column; a,c) and maximum CV (right column; b,d) of each AEW, normalized by the total number of AEWs resolved by each model individually during the historical period (1980-2000). Northern track values are displayed in the top row (a,b) with southern track values on the bottom (c,d). Patterned black lines represent each reanalysis. Solid black line is the model mean. Colors are representative of each CMIP5 model with warm (cool) colors corresponding to finer (coarser) resolution models. . . . 39

3.7 Yearly average CV (left column; a,c) and yearly maximum CV (right column; b,d) of each AEW, during the historical period (1980-2000). Northern track values are displayed in the top row (a,b) with southern track values on the bottom (c,d). Patterned black lines represent each reanalysis. Solid black line is the model mean. Colors are representative of each CMIP5 model with warm (cool) colors corresponding to finer (coarser) resolution models. . . . . 42

3.8 Historical biases of northern track AEW characteristics (see text for descriptions), calculated by subtracting the reanalysis mean from each model and converting to a percent error. The sum of the absolute value of each error is shown in the bottom row. Errors in monthly characteristics are calculated by root mean square error from the reanalysis mean. Models are listed with the finest resolutions on the left and coarsest resolutions on the right. Positive errors (reds) correspond to a value that is greater in the models than the reanalyses. Negative errors (blues) correspond to a model value that is less than the reanalysis mean. Colors near white indicate a good representation of the reanalyses by the model. . . . . 46

3.9 As in Fig. 3.8 but for southern track AEWs. . . . . 48

3.10 Average number of AEWs for each model in the historical and future periods is shown in the left column (a,c) with the grey line representing no change in frequency between the time periods, the black diamonds representing the reanalysis averages, and the stars representing model means. The difference in normalized monthly AEW frequencies (future − historical) is shown on the right (b,d) with the solid black line representing the overall model mean and the patterned black lines representing the least/most biased model mean. Northern track values are displayed in the top row (a,b) with southern track values on the bottom (c,d). Colors are representative of each CMIP5 model with warm (cool) colors corresponding to finer (coarser) resolution models. . . . . 51

3.11 Difference in normalized frequencies of AEW genesis (left column; a,d), dissipation (middle column; b,e), and time duration (right column; c,f) in the CMIP5 models in each 5° longitude bin between the historical (1980-2000) and future (2080-2100) periods (future − historical). Black dots representing the overall model mean and stars represent the average of the most/least biased models. Northern track values are displayed in the top row (a,b,c) with southern track values on the bottom (d,e,f). Colors are representative of each CMIP5 model with warm (cool) colors corresponding to finer (coarser) resolution models. . . . . 57

3.12 Difference in normalized frequencies of AEW speed (future − historical) with the the solid black line representing the overall model mean and the patterned black lines representing the model mean of those with most/least bias. Northern track values are displayed in (a) and southern track values in (b). Colors are representative of each CMIP5 model with warm (cool) colors corresponding to finer (coarser) resolution models. . . . . 59

3.13 Difference in yearly average CV (left column; a,c) and yearly average maximum CV (right column; b,d) between the historical (1980-2000) and future (2080-2100) periods (future − historical) with the grey line representing no change in intensity between the time periods, the black diamonds representing the reanalysis averages, and the stars representing model means. Northern track values are displayed in the top row (a,b) with southern track values on the bottom (c,d). Colors are representative of each CMIP5 model with warm (cool) colors corresponding to finer (coarser) resolution models. . . . 61

3.14 Difference in normalized frequency of average CV (left column; a,c) and maximum CV (right column; b,d) between the historical (1980-2000) and future (2080-2100) periods (future − historical). Northern track values are displayed in the top row (a,b) with southern track values on the bottom (c,d). The solid black line represents the overall model mean and the patterned black lines represent the model mean of those with most/least bias. Colors are representative of each CMIP5 model with warm (cool) colors corresponding to finer (coarser) resolution models. . . . . 67

A.1 Sensitivity test to determine the threshold CV that yields 30-40 AEWs per season (May-October) (Thorncroft and Hodges, 2001; Fink and Reiner, 2003; Hopsch et al., 2010; Bain et al., 2014) between 1980 and 2000 within JRA-55 reanalysis. . . . . 84

A.2 Sensitivity test to determine the setting of minimum longitude distance that yields 30-40 AEWs per season (May-October) (Thorncroft and Hodges, 2001; Fink and Reiner, 2003; Hopsch et al., 2010; Bain et al., 2014) between 1980 and 2000 within JRA-55 reanalysis. 84

A.3 Sensitivity test to determine the longitude error limit that yields 30-40 AEWs per season (May-October) (Thorncroft and Hodges, 2001; Fink and Reiner, 2003; Hopsch et al., 2010; Bain et al., 2014) between 1980 and 2000 within JRA-55 reanalysis. . . . . 85

A.4 Sensitivity test to determine the combination of minimum longitude distance and longitude error limit that yield 30-40 AEWs per season (May-October) (Thorncroft and Hodges, 2001; Fink and Reiner, 2003; Hopsch et al., 2010; Bain et al., 2014) between 1980 and 2000 within JRA-55 reanalysis. . . . . 85

B.1 Box plots (a,b,d,e) of the frequency of AEW net longitude in each 5° longitude bin, normalized by the total number of AEWs resolved by each model individually during the historical period (left) and future period (middle). The difference in normalized frequencies (future − past) is shown on the right (c,f). Northern track values are displayed in the top row with southern track values on the bottom. Diamond markers (a,d) represent each reanalysis. Colored dots (c,f) are representative of each CMIP5 model with warm (cool) colors corresponding to finer (coarser) resolution models. . . . . 86

C.1 Average CV of AEWs resolved each month during the historical period (left) and future period (middle). The percent change from the past to the future is shown on the right. Northern track values are displayed in the top row with southern track values on the bottom. Patterned black lines represent each reanalysis. Solid black line is the model mean. Colors are representative of each CMIP5 model with warm (cool) colors corresponding to finer (coarser) resolution models. . . . . 87

D.1 Yearly frequency of AEWs (left column; a,c) and monthly frequency normalized by the total number of AEWs resolved by each model individually (right column; b,d) during the future period (2080-2100). Northern track values are displayed in the top row (a,b) with southern track values on the bottom (c,d). Solid black line is the model mean. Colors are representative of each CMIP5 model with warm (cool) colors corresponding to finer (coarser) resolution models. . . . 89

D.2 Box plots of the frequency of AEW genesis (left column; a,d), dissipation (middle column; b,e), and time duration (right column; c,f) in the CMIP5 models in each 5° longitude bin, normalized by the total number of AEWs resolved by each model individually during the future period (2080-2100). Northern track values are displayed in the top row (a,b,c) with southern track values on the bottom (d,e,f). 90

D.3 Frequency of the average speed of each AEW, normalized by the total number of AEWs resolved by each model individually during the future period (2080-2100). Northern track values are displayed in (a) with southern track values in (b). Solid black line is the model mean. Colors are representative of each CMIP5 model with warm (cool) colors corresponding to finer (coarser) resolution models. . . . 91

D.4 Frequency of the average CV (left column; a,c) and maximum CV (right column; b,d) of each AEW, normalized by the total number of AEWs resolved by each model individually during the future period (2080-2100). Northern track values are displayed in the top row (a,b) with southern track values on the bottom (c,d). Solid black line is the model mean. Colors are representative of each CMIP5 model with warm (cool) colors corresponding to finer (coarser) resolution models. . . . . 92

D.5 Yearly average CV (left column; a,c) and yearly maximum CV (right column; b,d) of each AEW, during the future period (2080-2100). Northern track values are displayed in the top row (a,b) with southern track values on the bottom (c,d). Patterned black lines represent each reanalysis. Solid black line is the model mean. Colors are representative of each CMIP5 model with warm (cool) colors corresponding to finer (coarser) resolution models. . . . . 93

# Abstract

African Easterly Waves (AEWs) impact Sahel rainfall and serve as trigger disturbances for tropical cyclones (TCs) in the North Atlantic Ocean. So far, there has been very little investigation into future changes in intensity and location of AEWs and how these changes would impact the TC activity of the Atlantic Basin and rainfall across the Sahel. Gaining a more detailed understanding of AEW behavior within global climate models will reduce the uncertainty surrounding these TC precursors, potentially yielding higher confidence in future Sahel rainfall and TC trends.

This study uses a Hovmöller tracking technique to identify and track AEWs at 850 hPa. The magnitude, frequency, location, and speed of the AEWs is compared between reanalysis products (e.g. JRA-55, CFSR, ERA-Interim) and the coupled historical simulations from the fifth phase of the Coupled Model Intercomparison Project (CMIP5) to establish historical biases. Results show the resolution of the models is more important in reducing biases in the northern track AEWs compared to the southern. The tracking technique is then applied to future simulations (Representative Concentration Pathway 8.5) within the CMIP5 experiments. It is found that the CMIP5 models project an average increase of 1.5 AEWs per year in the northern track, including an increase in higher intensity waves. The signals from the southern track AEWs in the future simulations are more varied compared to the northern track models, consistently resulting in a disagreement regarding future changes. However, there is indication of a shift in seasonality of southern track AEWs towards the later summer months, which may impact the

timing of the Atlantic TC season. Future work will include a 3D tracking technique in order to definitively determine the two distinct AEW tracks. This may provide a clearer distinction between the northern and southern regions which could result in more significant changes in future AEW characteristics within each region.

# Chapter 1

# Introduction and Background

African Easterly Waves (AEWs) have a substantial influence on the large-scale weather patterns over Northern Africa (Martin and Thorncroft, 2015), including their modulation of rainfall across the Sahel (Fink and Reiner, 2003) and their role as trigger disturbances for tropical cyclones (TCs) in the North Atlantic Ocean (Landsea and Gray, 1992; Pasch and Avila, 1994). These atmospheric waves are synoptic-scale disturbances that travel westward across North Africa and into the Atlantic Basin with wavelengths ranging from 2,000-4,000 km (Burpee, 1974; Hopsch et al., 2010), phase speeds of 7-9 m/s (Burpee, 1974), and periods between 2-10 days (Martin and Thorncroft, 2015; Burpee, 1972). AEWs exist in the mid- to lower-troposphere, where their amplitudes peak near 600-700 hPa (Hopsch et al., 2007; Martin and Thorncroft, 2015; Burpee, 1972).

AEWs are extremely important synoptic features that contribute to the rainfall variability over Western Africa, and the Sahel in particular. Anomalously rainy summer seasons have been linked to seasons of longer-lived, more intense AEWs (Grist, 2002). Further studies have shown that AEWs generate and organize mesoscale convective systems and squall lines (Carlson, 1969; Mekonnen et al., 2006; Skinner and Diffenbaugh, 2013). In fact, 42% of the West African squall lines can be described as "AEW-forced" as they form in either a region west of the AEW trough or in the area of maximum southerly wind (Fink and Reiner,

2003). With mesoscale convective systems and squall lines contributing to nearly 90% of the Sahel's yearly rainfall (Mathon et al., 2002), a better understanding of the future projections in AEW characteristics will also provide insight into the future of West African rainfall.

## 1.1 African Easterly Wave Genesis

The unique geography of the African continent (Fig. 1.1) is responsible for the formation of the African Easterly Jet (AEJ). The Gulf of Guinea coast resides near 5°N, moderating the seasonal surface temperature variations at the coast and near the equator. The Sahara desert, however, is situated within Northern Africa where surface temperatures reach more extreme values. In fact, this Northern Hemispheric region of Africa has reported changes in mean monthly surface temperature as drastic as 10°C across 10° latitude (Burpee, 1972). The distribution of vegetation in Africa creates a soil moisture gradient as the northern latitudes correspond to dry, desert regions and the Gulf of Guinea coast near 5°N enhances the soil moisture (Cook, 1999). The latitudinal differences in sensible heating activate a thermal wind relation that induces easterly vertical wind shear over the westerly wind at the surface. Aloft, there is deep, moist convection near the equatorial region creating heating in the upper troposphere near the equator and acting to reverse the upper tropospheric potential temperature gradient and create westerly shear of the zonal wind near 600-400 hPa (Burpee, 1972). The baroclinic zone at the surface in tandem with the reversal of the potential temperature gradient aloft yields a maximum in easterly zonal wind in the mid-troposphere, typically near 600-700 hPa (Burpee, 1972). This phenomenon is known as the AEJ. The AEJ is typically located around 10°N-15°N in the summer months (Cook, 1999; Thorncroft and Hodges, 2001; Grist, 2002; Hall et al., 2006; Skinner and Diffenbaugh, 2013).

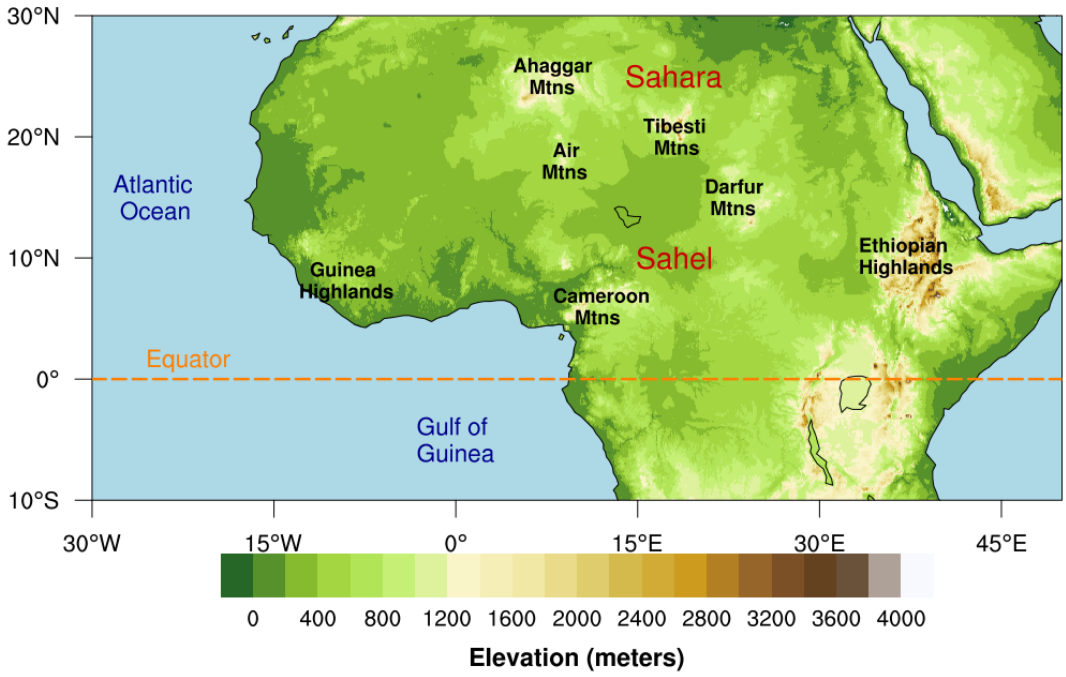



Figure 1.1: Topography (contours) of the African domain utilized in this study from the ETOPO2v2 dataset (National Geophysical Data Center, 2006).

Due to their proximity to the Atlantic Ocean (Fig. 1.1) as well as the Gulf of Guinea, the equatorial regions remain more moist than the desert regions to the north, enabling the equatorial regions to maintain a more consistent maximum daily surface temperature throughout the year. The Saharan region experiences more extreme temperature fluctuations, with surface temperatures peaking during July and August, creating the greatest meridional surface temperature gradient during the summer season (Burpee, 1972). Therefore, the AEJ is observed to be strongest during the summer months and shifted furthest poleward. Note that the AEJ is a year-round phenomenon positioned in the western part of Northern Africa, just above the surface baroclinic zone, but it shows a significant increase in strength and organization during April through November (Burpee, 1972).

The pioneering genesis theory of AEW development was spearheaded by Burpee (1972). He describes the ageostrophic, thermally direct circulations which exist above and below the AEJ level that provide a reservoir of kinetic energy essential

to the maintenance of the jet. The lower (upper) level circulation is composed of warm air rising in the northern (southern) sector and cool air sinking in the southern (northern) sector.

The temperature distribution across latitude and height provides a setup conducive to unstable zonal flow on the equatorward side of the AEJ core (Burpee, 1972). Therefore, the baroclinic instabilities of the AEJ foster the intensification of AEWs over land as AEWs withdraw energy from the vertical shear of the basic-state. As the AEWs move into the Atlantic, the environment becomes increasingly barotropic and the waves must attain their energy at the expense of the horizontal shear (Hall et al., 2006).

This original genesis theory rests on the idea that the natural state of the AEJ is unstable, yielding baroclinic-barotropic instabilities with the ability to form AEWs. However, Hall et al. (2006) show that damping at low levels extracts energy from the AEJ, diminishing growth rates and stabilizing the system. Therefore, solely baroclinic-barotropic instabilities of the AEJ cannot be held responsible for the genesis of AEWs— a large, finite amplitude perturbation is also required.

In the study by Thorncroft et al. (2008), a model configuration incorporates low-level damping in order to neutralize the AEJ. This allows the hypothesis to be tested regarding whether AEWs form subsequently following an upstream deep, shallow, or stratiform heating event near the AEJ entrance region. All three heating profiles generate an initial trough that moves westward along the AEJ, with each succeeding wave becoming stronger than the previous. The shallow heating profile produces the most intense AEWs due to the concentration of the intense heating near the entrance region of the AEJ and the deep heating profile results in the smallest amplitude waves. Hence, upstream convection can trigger an easterly wave train, and the heating profile itself is important in controlling the amplitudes of the downstream waves.

## 1.2 African Easterly Wave Characteristics

Previous studies (Thorncroft and Hodges, 2001; Hopsch et al., 2007; Chen et al., 2008) have hypothesized the possibility of the existence of two distinct AEW storm tracks—one to the north and one to the south of the AEJ.

The southern track AEWs are typically located south of 15°N. With their existence at latitudes near the Inter-tropical Convergence Zone, southern AEWs increase convection and enhance moisture in the region. These AEWs exist at lower levels, but their amplitudes peak in the mid-levels near 600-700 hPa. The genesis region of these southern AEWs has been disputed. Carlson (1969) argues that southern track AEWs form over the African continent at eastern longitudes near the mountainous region of Ethiopia. However, the eastern-most longitudes of AEW genesis as detected by Burpee (1972) only trace back to 15°E. More recently, the studies by Thorncroft and Hodges (2001), as well as Hopsch et al. (2007), place the dominant genesis region near the West African coast (15°W), with the peak slightly offshore. This idea, though, is inconsistent with genesis theory since AEWs are believed to initiate over land and intensify in conjunction with the AEJ, so perhaps the AEWs are initiated over the African continent, but their amplitudes are too weak to be identified until they reach the West African coast. After leaving the West African coast, there is a prominent protrusion of the southern track AEWs into and across the Atlantic Ocean, making these waves of primary importance for tropical cyclogenesis.

Kiladis et al. (2006) first identify westward moving, southern track waves near Sudan (30°E). For AEWs existing over land and east of the Greenwich Meridian, the convection is situated in the 850 hPa northerly flow on the west side of the trough. As the AEW propagates near 0° longitude, the trough and convection align. The trough's phase speed continues to travel slightly faster than the convection so that the convection resides in the southerlies east of the trough when

the AEW reaches the Atlantic. At 200 hPa, the convection is positioned in the northerlies to the east of the ridge as the wave travels across the continent and into the ocean, modifying the vertical tilt of the AEW as they propagate (Kiladis et al., 2006). These waves exhibit less vertical tilt which can be linked to weaker baroclinicity due to more significant contributions of convection (Reed et al., 1977). The convergence peaks at low-levels, near 925 hPa, with two peaks in divergence and upward motion. The 400 hPa peak in vertical motion is likely associated with the deeper convection present over land whereas the 700 hPa peak corresponds to waves over the ocean (Kiladis et al., 2006).

The northern track waves have their strongest amplitudes at lower levels, near 850 hPa. They are situated north of 15°N, positioning them in close proximity to the Sahara where convection is weaker, generally giving northern track waves drier characteristics. Lacking moisture compared to the southern track waves (Hopsch et al., 2007; Chen et al., 2008), these AEWs play less of a role in rainfall variability and tropical cyclogenesis, but become important in the transport of Saharan dust (Skinner and Diffenbaugh, 2014). The northern track AEWs do not possess a clear, horizontal track extending from the African continent, past the coast, and into the Atlantic. Instead, track densities [Fig. 6 of Thorncroft and Hodges (2001)] show the northern track AEWs moving westward across the continent until they reach the coast, where the tracks shift toward the southwest and precede westward closer to 10°N on the maritime side of the coast. This track density is composed of AEWs which exhibit a bimodal distribution in genesis location. The continental peak in genesis occurs near 25°N, 10°E in conjunction with both the Hoggar mountains and the maximum in the continental temperature gradient (Thorncroft and Hodges, 2001). The secondary genesis peak is located on the maritime side of the African coast, but at equatorward latitudes compared to the continental peak. This suggests that these lower-level AEWs either form over

land in the northern region and track westward until their demise as they reach the coast, or they form in the more southern region over the Atlantic Ocean near the African coast. However, they do not typically originate along the poleward track and shift towards the southwest as they traverse the African coast.

The northern track waves show a different horizontal and vertical structure compared to the southern waves, as the convection is consistently situated in the 850 hPa southerly flow east of the trough regardless of the wave's location. At upper levels, the convection is located along the anticyclonic ridge creating more vertical tilt than observed in the southern waves (Kiladis et al., 2006). There is also a distinctly different vertical motion distribution. The level of maximum convergence is near 700 hPa, with sinking motion below and divergence at the surface, as well as rising motion above resulting in another peak in divergence at 300 hPa (Kiladis et al., 2006).

While the the northern and southern track waves have different structures and appear to have two distinct paths over land, they both contribute to one main storm track over the Atlantic Ocean—with maximums at 850 hPa and 600-700 hPa. TC genesis just offshore of the West African coast could be attributed to the latent heat release expected in this rainy zone (Thorncroft and Hodges, 2001).

Although only approximately 60% of minor TCs and tropical storms are initiated by AEWs (Chen et al., 2008), close to 85% of major TCs (greater than category 3 on the Saffir-Simpson Scale) originate from AEWs (Landsea, 1993). Since the northern track AEWs are drier with weaker convection, they must travel a greater westward distance across the Atlantic to attain sufficient moisture before undergoing tropical cyclogenesis. However, the majority of northern track AEWs have limited westward propagation after traversing the coast, leaving only 20% of the northern AEW tracks traveling into the main development region for North Atlantic TCs (Hopsch et al., 2007). While there are fewer total southern track

AEWs, the track density of these waves illustrates the propensity of the southern waves to travel further across the Atlantic Basin. Nearly 75% of the southern track AEWs reach the main development region (Hopsch et al., 2010) and they are roughly twice as effective in initiating TCs (Chen et al., 2008) when compared to the northern track waves.

The peak in the number of waves propagating along the southern storm track occurs in September, which is also the month of the highest Atlantic TC activity (Hopsch et al., 2007). However, there are consistently more southern track AEWs propagating into the main development region than there are named Atlantic tropical cyclones, giving rise to the idea that the number of southern track AEWs could supply an upper bound for the number of named tropical cyclones (Hopsch et al., 2007). The intensity of the AEWs and the relationship with tropical cyclogenesis has also been examined. The results of Hopsch et al. (2007) support those from Thorncroft and Hodges (2001) in that the number of AEWs with amplitudes exceeding a certain threshold may be more important than the total number of AEWs in hypothesizing downstream tropical cyclogenesis.

Hopsch et al. (2010) diagnosed differences in the AEW structure and environment of AEWs which developed into TCs and those that did not. Developing AEWs move westward across the African continent, increasing their convection as they approach the Guinea Highlands. During their transition to a warm-core system, the low-level vorticity is enhanced within the trough. The developing AEWs move into an ocean environment with high sea surface temperatures and low vertical wind shear, allowing the convection to sustain and increase, resulting in tropical cyclogenesis. The non-developing AEWs undergo a similar genesis; however, their amplitudes, convection, and low-level vorticity typically remain weaker. Aloft, there also appears to be a region of dry air downstream of a non-developing AEW trough. Though, there are some non-developing AEWs that possess greater

vorticity and more intense convection than developing AEWs. In these cases, the suppression of convection as the AEW moves over the ocean can be attributed to the dry air aloft and downstream of the AEW trough.

## 1.3 African Easterly Waves within Global Climate Models

Recent studies have begun to understand AEWs within a variety of global climate models to determine how accurately the models simulate AEWs compared to reality. McCrary et al. (2014a) and McCrary et al. (2014b) compared the different representations of the AEJ and AEWs within the standard Community Climate System Model, version 3 (CCSM3) and the superparameterized Community Climate System Model (SP-CCSM). The main differences between the two models stem from the convective schemes—the CCSM3 contains traditional cloud parameterizations, whereas the SP-CCSM utilizes a two-dimensional cloud resolving model. Eddy kinetic energy (EKE) is used to quantify AEW activity, as it is regarded as a reliable measurement of AEW location and intensity. Results show that the simulation of the AEJ is too strong in the CCSM3 whereas the AEWs are barely resolved and far too weak. Within the SP-CCSM, the AEWs are too intense compared to observations and are associated with an AEJ that is too weak. This dichotomy is explained by the hypothesis that AEWs grow by withdrawing energy from the baroclinic-barotropic instabilities along the AEJ, so the presence of AEWs acts to weaken the jet. A similar pattern is shown through the AEW structure; the horizontal and vertical structures depicted by the SP-CCSM are a much closer match to observations (though still too strong) when compared to the spatial representation of AEWs within the CCSM3.

Skinner and Diffenbaugh (2013) identify AEWs using spectral analysis (discussed in further detail in section 2.2) of the 700 hPa meridional wind field of the Coupled Model Intercomparison Project, Phase 3 (CMIP3) ensemble. The spectrum of seven of the CMIP3 models show a peak in the frequency of both meridional wind and precipitation that corresponds to the expected period of AEWs. Six of these seven models produce AEWs with stronger intensity than that of the ERA-Interim reanalysis. The models that simulate the weakest AEWs also show weaker precipitation than the reanalysis. Taking the full CMIP3 ensemble into account highlights the lack of agreement regarding the future projections of AEW activity and African rainfall—by the year 2100, half of the models predict an increase in rainfall over West Africa and the rest of the models anticipate decreasing precipitation (Skinner and Diffenbaugh, 2013).

EKE has been previously used to compare AEWs within CMIP5 models (Taylor et al., 2012) to several reanalyses (Martin and Thorncroft, 2015). The EKE in the historical models (1980-2000) shows AEWs that are too weak in the northern region and too strong, but too dry along the southern region when compared to the reanalyses. The same EKE biases are present within the atmosphere only (AMIP) models, establishing that the errors are not linked to sea surface temperature biases, but rather with AEW forcing, simulation of the AEJ, or convective parameterizations (Martin and Thorncroft, 2015). Another explanation of the biases could stem from a possible inability of the models to resolve the two distinct northern and southern tracks of AEWs. Seasonal biases are also shown within the EKE associated with AEWs. During the summer months, there is excessive EKE over land with a distinct reversal to deficient EKE over the ocean (Martin and Thorncroft, 2015). This highlights the struggles of the models to either traverse the AEWs across the coast or to produce a secondary peak in genesis near the coast. This weakness may be due to the model resolutions. Ventrice et al. (2012)

emphasizes the importance of the Guinea Highland topography in initiating convection to enhance existing AEWs or form new AEWs. The Guinea Highlands, however, can not be reproduced at grid spacings coarser than 2.8° (Martin and Thorncroft, 2015).

Bain et al. (2014) performed a comparison between the representation of AEW tracks using curvature vorticity and an objective tracking algorithm within ERA-Interim reanalysis and the MetUM (Global Atmosphere 3.0) model, as opposed to using EKE as a measure of AEW activity. The AEWs simulated by the MetUM model exhibited weaker intensity corresponding to an overall fewer number of waves resolved each season. There were also differences in the seasonality of the waves. The reanalysis showed a distinct peak in vorticity around August/September, but the MetUM model shows a much more constant strength in AEWs throughout the season. Differences in AEW strength show substantial improvement after increasing the model's horizontal resolution.

It is also important to note a common theme throughout several studies utilizing climate models. Increasing the model's horizontal and vertical resolution is commonly thought to improve simulations of AEWs including their track characteristics (Hodges et al., 2003), their role in generating and interacting with clouds (McCrary et al., 2014b) and precipitation (Vellinga et al., 2016), and their average and maximum intensity (Bain et al., 2014). Improvements in resolution can also enhance the detail regarding the topography of Africa. For example, the Guinea Highlands cannot be accurately resolved in models with grid spacing coarser than 2.8° (Martin and Thorncroft, 2015). Without this topographic feature, the models fail to simulate the genesis or the reinvigoration of AEWs before leaving the African coast, often resulting in dissipation too early compared to reanalyses. Many of these same studies also stress the importance of the model

physics on the representation of AEWs. The planetary boundary layer parameterizations, the convective parameterizations, and the simulation of the AEJ all have a significant impact on the strength and life-cycle of the AEWs (Hodges et al., 2003; Ruti and Dell'Aquila, 2010; Bain et al., 2014; McCrary et al., 2014b; Vellinga et al., 2016).

The need to establish past and future trends of Atlantic TCs and Sahel rainfall has motivated several studies to analyze AEWs within future time periods of global climate models using EKE. There are distinct differences in future changes between the northern and southern AEWs. The drier waves of the northern region are projected in increase in total frequency in the future (2080-2100), with the largest increases occurring for the most intense AEWs (Martin and Thorncroft, 2015; Skinner and Diffenbaugh, 2014). Therefore, the mean strength of northern track AEWs is projected to increase. EKE within the northern region is expected to increase during the mid-summer months, peaking at 30% increases in August (Martin and Thorncroft, 2015), and resulting in a more distinct seasonal cycle. The future of the southern track AEWs remains ambiguous as there is a lack of consensus among the models regarding changes in frequency and strength (Martin and Thorncroft, 2015; Skinner and Diffenbaugh, 2014). The southern region does however exhibit a slight decrease in AEW activity in May which may cause a later start to the AEW and TC season in the future (Martin and Thorncroft, 2015). While EKE is a bulk measurement proven useful in determining biases in AEW strength and location, its primary intention is not aimed at tracking individual AEWs. Therefore, conclusions cannot be reported regarding past and future trends of the frequency of AEWs or their track characteristics.

These discrepancies regarding trends for southern track AEWs translate into disagreement among the models in the future of Atlantic TCs. Camargo (2013) found no robust signal for future changes in TC frequency within CMIP5 models.

This study is contradicted by Emanuel (2013) who revealed evident increases in TC frequency in the North Atlantic within CMIP5 models, but also recognized that CMIP3 models predict decreases in future TC frequency. Dwyer et al. (2015) examined changes to future lengths of the TC season, but found no consensus among the models regarding changes to the season length. The most notable result is the projected shift in Atlantic TC season towards later months (Dwyer et al., 2015) which is consistent with the seasonal shift in southern track AEWs (Martin and Thorncroft, 2015).

## 1.4 Research Goal

The goal of this study is to gain a detailed understanding of future changes in AEW behavior in order to reduce the uncertainty surrounding these TC precursors, yielding higher confidence and more reliable projections of future Sahel rainfall and TC trends. There is not currently an agreement regarding the projected TC, Sahel rainfall, or AEW trends for the future. With AEWs often acting as precursor cyclonic circulations to initiate Atlantic TCs, it has been proposed that variations in AEW intensity, frequency, location, and other physical characteristics can impact the TC itself (Martin and Thorncroft, 2015). However, there has been very little investigation into past and future changes in intensity, location, and physical characteristics of AEWs and how these changes impact TC activity in the Atlantic Basin and rainfall across the Sahel.

This study addresses an important gap within tropical meteorological research and is beneficial to society. Identifying the extent to which AEW track characteristics are changing will provide a better understanding of the future projections for Sahel rainfall and Atlantic TCs. Agriculture in the Sahel is dependent on the rainfall associated with AEWs. Crops can be decimated by seasons of too little or too much rainfall (Wang and Gillies, 2011); thus, understanding AEWs now and

in the future will be important in improving the socio-economic stability of the Sahel. For the United States, extreme rainfall, severe wind gusts, and storm surge are just a few of the consequences that occur in association with Atlantic TCs, all of which have large societal impact including fatalities and property destruction (Rappaport, 2014).

# Chapter 2

# Data and Methodology

## 2.1 Data

To determine how AEWs are changing in the future, it is imperative to first have an accurate depiction of AEWs in the past. Unfortunately, atmospheric observations are sparse in tropical Africa (Diaconescu et al., 2015) but reanalysis datasets are available over Africa for extended historical time periods. Each reanalysis is sensitive to its own model physics and method of data assimilation which introduce error and inconsistencies between them. Therefore, this study and previous studies (Hodges et al., 2003; Diaconescu et al., 2015; You et al., 2015) use the average of multiple reanalysis products to represent past atmospheric variables in observationally-sparse regions. Three reanalyses are used, including ERA-Interim (ERA-I) (Simmons et al., 2007) data from the European Centre for Medium-range Weather Forecasts (1979-present; 0.75° resolution), Climate Forecast System Reanalysis (CFSR) (Saha et al., 2010) data from the National Centers for Environmental Prediction (1979-present; 0.5° resolution), and JRA-55 (Kobayshi et al., 2015) data from the Japanese Meteorological Agency (1958-present; 1.25° resolution). Extensive use is made of output from historical (1979-2005) and future (2006-2100) simulations from the CMIP5 ensemble (see Table 2.1). The highest radiative forcing experiment, Representative Concentration Pathway 8.5 (RCP8.5),

Table 2.1: List of CMIP5 models used in this study, including their horizontal resolution. Only one ensemble member was used for each model.

| **Model** | **Hist.** | **Fut.** | **Horizontal Resolution (Lat x Lon)** | **Reference** |
|---|---|---|---|---|
| ACCESS1-0 | ✓ | ✓ | 1.25 x 1.88 | Bi et al. (2013) |
| ACCESS1-3 | ✓ | ✓ | 1.25 x 1.88 | Bi et al. (2013) |
| CNRM-CM5 | ✓ | ✓ | 1.41 x 1.41 | Voldoire et al. (2013) |
| CSIRO-Mk3-6-0 | ✓ | ✓ | 1.88 x 1.88 | Rotstayn et al. (2010) |
| FGOALS-g2 | ✓ | ✓ | 3.00 x 2.81 | Zhou et al. (2013) |
| GFDL-CM3 | ✓ | ✓ | 2.00 x 2.50 | Donner et al. (2011) |
| GFDL-ESM2G | ✓ | ✓ | 2.00 x 2.50 | Dunne et al. (2012) |
| GFDL-ESM2M | ✓ | ✓ | 2.00 x 2.50 | Dunne et al. (2012) |
| inmcm4 | ✓ | ✓ | 1.50 x 2.00 | Volodin et al. (2010) |
| MIROC-ESM | ✓ | ✓ | 2.81 x 2.81 | Watanabe et al. (2010) |
| MIROC-ESM-CHEM | ✓ | ✓ | 2.81 x 2.81 | Watanabe et al. (2010) |
| MIROC4h | ✓ | | 0.56 x 0.56 | Watanabe et al. (2010) |
| MIROC5 | ✓ | ✓ | 1.41 x 1.41 | Watanabe et al. (2010) |
| MPI-ESM-LR | ✓ | ✓ | 1.88 x 1.88 | Giorgetta et al. (2013) |
| MPI-ESM-MR | ✓ | ✓ | 1.88 x 1.88 | Giorgetta et al. (2013) |
| MPI-ESM-P | ✓ | | 1.88 x 1.88 | Giorgetta et al. (2013) |
| MRI-CGCM3 | ✓ | ✓ | 1.13 x 1.13 | Yukimoto et al. (2012) |
| MRI-ESM1 | ✓ | ✓ | 1.13 x 1.13 | Adachi et al. (2013) |
| NorESM1-M | ✓ | ✓ | 1.88 x 2.50 | Bentsen et al. (2013) |

is investigated for the future period. Nineteen CMIP5 models are examined in the historical period, with seventeen of those models available for comparisons with future simulations. Notice that several models fall within model "groups"(ACCESS, GFDL, MIROC, MPI-ESM, MRI). Therefore, it is assumed that the nineteen models are not completely independent and similarities in results are expected within each model "group." The atmospheric variables within the CMIP5 models are reported on a horizontal grid ranging from 0.5° to 4.0°, where the majority of the models have a resolution finer than a 1.3° grid (Taylor et al., 2012). This is a significant improvement from the CMIP3 ensemble which included only one model with grid spacing smaller than 1.3°. Other improvements implemented within the CMIP5 ensemble include a more comprehensive earth system of aerosols, carbon, and biochemical cycles as well as an increased number of variables and more complete documentation.

To quantify low-level (850 hPa) AEW activity, six-hourly zonal and meridional wind data from each reanalysis product and CMIP5 model is used to calculate curvature vorticity (CV). CV is desirable for tracking AEWs, especially in models, as it eliminates the background shear vorticity associated with the proximity of the AEWs to the AEJ and removes any bias related to the strength of the jet. Previously, AEW studies have identified waves using meridional wind (Burpee, 1974; Diedhiou et al., 1998; Fink and Reiner, 2003; Berry and Thorncroft, 2005; Ruti and Dell'Aquila, 2010; Skinner and Diffenbaugh, 2013, 2014), outgoing longwave radiation (Kiladis et al., 2006; McCrary et al., 2014b), brightness temperature (Mekonnen et al., 2006), 2-6 day filtered streamfunction (Hopsch et al., 2010), EKE (McCrary et al., 2014a; Martin and Thorncroft, 2015), relative vorticity (Thorncroft and Hodges, 2001; Hodges et al., 2003; Hopsch et al., 2007), and more recently CV (Bain et al., 2014; Brammer and Thorncroft, 2015).

As AEWs and rainfall are most prevalent during the summer, the analysis extends from May 1 to November 1 of each year within the historical period (defined as 1980-2000) and the future period (defined as 2080-2100). The region where the AEW tracking algorithm is applied is confined to the longitude band extending from 40°W to 45°E in order to capture a range of topographic features that have been shown to impact AEWs (see Fig. 1.1)—the Atlantic Ocean (west of approximately 15°W), the West African Coast (15°W), the Guinea Highlands (near 10°W), the Tibesti Mountains (near 18°E), the Darfur Mountains (near 23°E), and the Ethiopian Highlands (near 40°E). The latitude band of interest is divided into a section 15° north of the AEJ for the northern track waves and 15° south of the AEJ for the southern track waves. The location of the AEJ, and therefore the latitude band, differs slightly in each model (see Fig. 3.2).

## 2.2 African Easterly Wave Identification Techniques

Previous studies have used spectral analysis to understand AEWs. Spectral analysis techniques create Fourier spectra to identify the period of AEWs (Kiladis et al., 2006). Figure 2.1 shows the spectral analysis for the summer months (June-September) of 1980-2000 using JRA-55 reanalysis data of 850 hPa daily mean meridional wind. Any local maxima or local minima falling outside the dashed lines are considered significant at the 95% confidence level. The highest power for the average of all of these years is shown near 0.215 cycles/day (corresponding to a period of 4.65 days) and near 0.27 cycles/day (corresponding to a period of 3.7 days), clearly within the 2-10 day range cited in Chapter 1. These spectral peaks give confidence in the presence of AEWs within the JRA-55 reanalysis dataset. This spectral analysis method can identify the presence of AEWs according to the meridional wind frequencies; however, it is less practical for short time scales

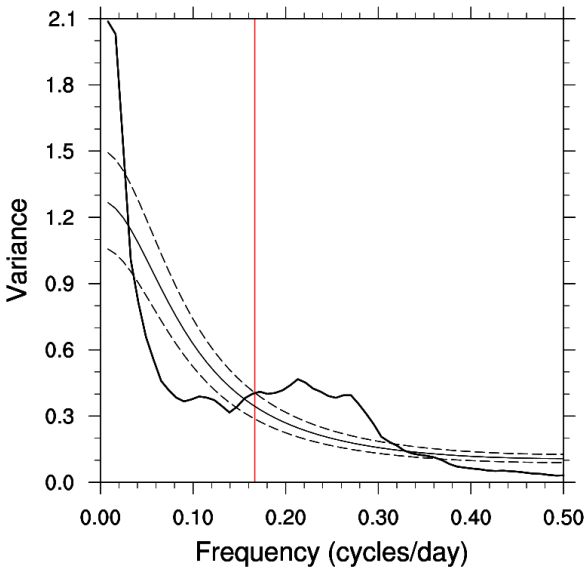



Figure 2.1: Average spectrum of daily mean meridional wind for the summer months (June-September) of 1980-2000, for a region concentrated over the African continent (between 0°N-30°N and 20°W-40°E). The red line is a marker for a 6-day period. The smooth lines represent the 95% confidence interval with the solid line showing the mean power and the dotted lines representing the upper and lower 2.5% bounds.

and does not track individual AEW events. Hence, spectral analysis will not be sufficient for this study and a tracking method is required.

Manual tracking methods typically analyze streamlines near the level of the AEJ to identify individual waves near the western coast of Africa and trace them into the Atlantic or back to their genesis (Chen et al., 2008; Fink and Reiner, 2003). These resulting tracks provide information about the latitude and longitude of the AEW, which becomes useful if comparing AEWs along the northern and southern tracks. Manual methods are typically most successful within case studies, but the process is subjective and labor intensive, making it difficult to utilize this method for large datasets, such as the CMIP5 ensemble.

### 2.2.1 Objective Tracking

This study will employ an objective tracking method stemming from Hovmöller plots (time vs. longitude) of CV (e.g. Fig. 2.2), similar to the algorithm employed by Bain et al. (2014) and modified from Brammer and Thorncroft (2015). This technique, however, has not been applied to tracking AEWs in global climate

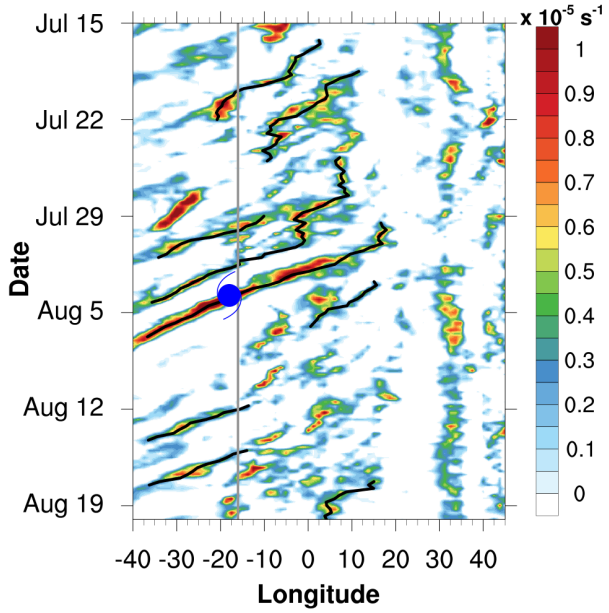



Figure 2.2: Hovmöller of curvature vorticity contours (averaged between 0°N and 30°N) for the year 2000. Black lines are AEW tracks from the objective tracking method. Vertical grey line represents the approximate West African coastline. Blue symbol represents the genesis location of Hurricane Alberto from the IBTrACS dataset (Knapp et al., 2010).

models. Throughout a chosen latitude band (between the latitude of the AEJ core and either 15° to the north or 15° to the south), a meridional average of CV is calculated for each longitude between 40°W and 45°E. The derivative of CV in the longitude and time directions represents the troughs and ridges of the AEWs. The second derivative then masks out the ridges. The longitudinal "track" of an AEW is pieced together through linear extrapolation—connecting neighboring centers of local CV maxima when the location at the later time step matches the location estimated by the mean speed parameter within the acceptable range of error.

The tracking algorithm only considers CV maxima with magnitudes greater than or equal to 0.15x10$^{-5}$ s$^{-1}$. Waves traveling less than 15° longitude or lasting less than two days are removed. The expected phase speed of the AEWs is set to 7 ms$^{-1}$ with a 6° longitude error limit for estimating the AEW's location at the following time step. These settings were determined after a series of sensitivity tests using the JRA-55 reanalysis data (see Appendix A).

The results from this tracking algorithm were compared to a test case of the AEW that triggered the genesis of Hurricane Alberto (2000), which was analyzed in detail by Berry and Thorncroft (2005). They used a comparable method of

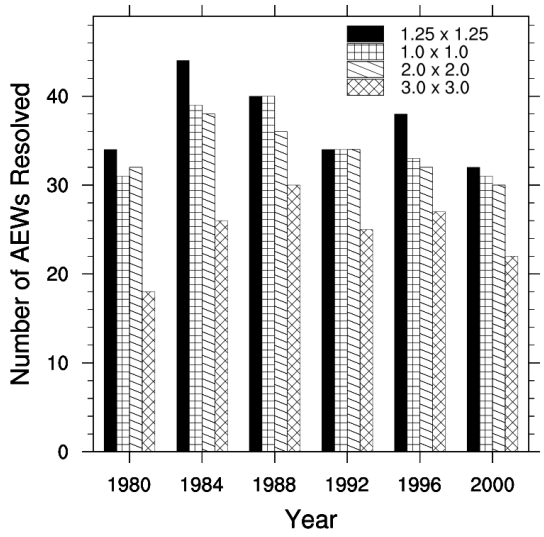



Figure 2.3: Number of waves resolved by the objective tracking algorithm for six years between 1980 and 2000 using four different grid spacings of the JRA-55 reanalysis.

tracking which stemmed from Hovmöller diagrams of 700 hPa meridional wind. The longitudinal tracks are extremely similar between this study and that done by Berry and Thorncroft (2005)— the AEW forms near 16°E on August 1, reaches the West African coast on August 4, and 30°W on August 6. The consistency among the location, time, and speed of the AEWs between the two tracking methods yields confidence in the AEW tracking algorithm executed throughout this study.

As shown by Table 2.1, the CMIP5 models have a grid spacings that range from 0.56° to 3.00°. Several studies have noted the impact the model resolution may have on AEW tracks (Hodges et al., 2003; Bain et al., 2014). This notion is tested for the yearly frequency of AEW tracks using the JRA-55 reanalysis. JRA-55 reanalysis data is regridded from its original 1.25° resolution to a 1.0°, 2.0°, and 3.0° grid and the objective tracking algorithm is applied at each resolution. The number of waves identified at each resolution, for six years in the historical period is shown in Fig. 2.3. Between 1980 and 2000, the average number of AEWs resolved by JRA-55 at the original 1.25° resolution is 34.9; whereas the 1.0° grid resolved 32.9, the 2.0° grid resolved 32.3, and 3.0° grid resolved 23.2. Regridding the original data does not drastically alter the number of waves resolved by the objective tracking algorithm at 1.0° and 2.0°, but the number of waves significantly decreases on a 3.0° grid.

This result forms the expectation that CMIP5 models with horizontal resolutions greater than 2.0° will underestimate the number of AEWs, which could create unfair comparisons between models at different resolutions. To be certain that the differences in AEW characteristics are not solely due to the model resolution, models will be compared to each other using normalized frequencies (dividing the frequency by the total number of waves resolved in each model individually). Strict frequencies will only be reported when making comparisons between the historical and future model simulations, but within an individual model.

# Chapter 3

# Results

## 3.1 African Easterly Jet

The separation of northern and southern track waves in the objective tracking analysis depends on the location of the AEJ. The AEJ latitude location is determined by the location of the 700 hPa maximum zonal wind averaged over the African continent (from 10°W to 30°E). The reanalyses and CMIP5 historical models show the AEJ shifting towards its most poleward location during the summer months, peaking near August (Fig. 3.1a). This supports the findings from Grist (2002) who also documented a seasonal shift in the AEJ with the August peak residing at 12°N within the NCEP reanalysis. The peak summertime latitude of the AEJ ranges from 7°N to 21°N in both the historical and future analysis periods.

To compare the changes in the location of the AEJ between the historical period and a future period, the difference by month is shown in (Fig. 3.1b). Contrasting changes are observed in the models, especially at the beginning of the summer. From May to August, seven of the models show that the AEJ shifts towards the south in the future, whereas five models simulate a northward shift of the AEJ, and five models show no change. From August to October, there is more agreement for future changes with nine models indicating a poleward shift, two models showing an equatorward shift, and six models remaining constant. These future changes in

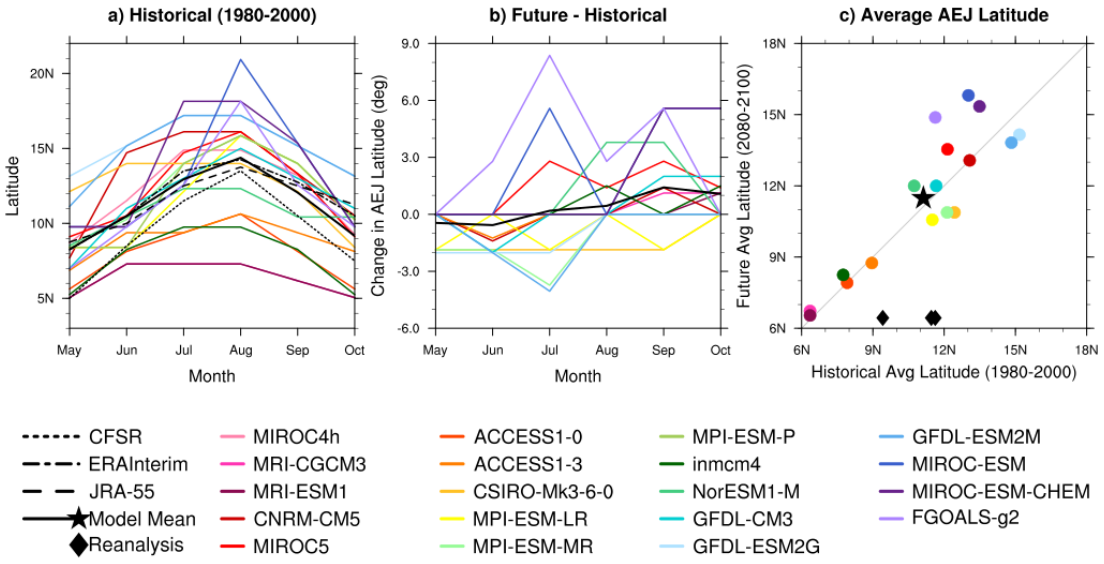



Figure 3.1: Latitude location of the AEJ by month for the historical period (a) and future − historical (b). The May-October average AEJ location is compared between the historical and future periods in (c) with the grey line representing a constant AEJ location, the black diamonds representing the average AEJ location in the reanalyses, and the star as the model mean. The patterned black lines (a) represent the reanalyses, the solid black line shows the model mean (a,b) and the colored lines (a,b) or dots (c) indicate individual models. Warm (cool) colors correspond to finer (coarser) resolution models.

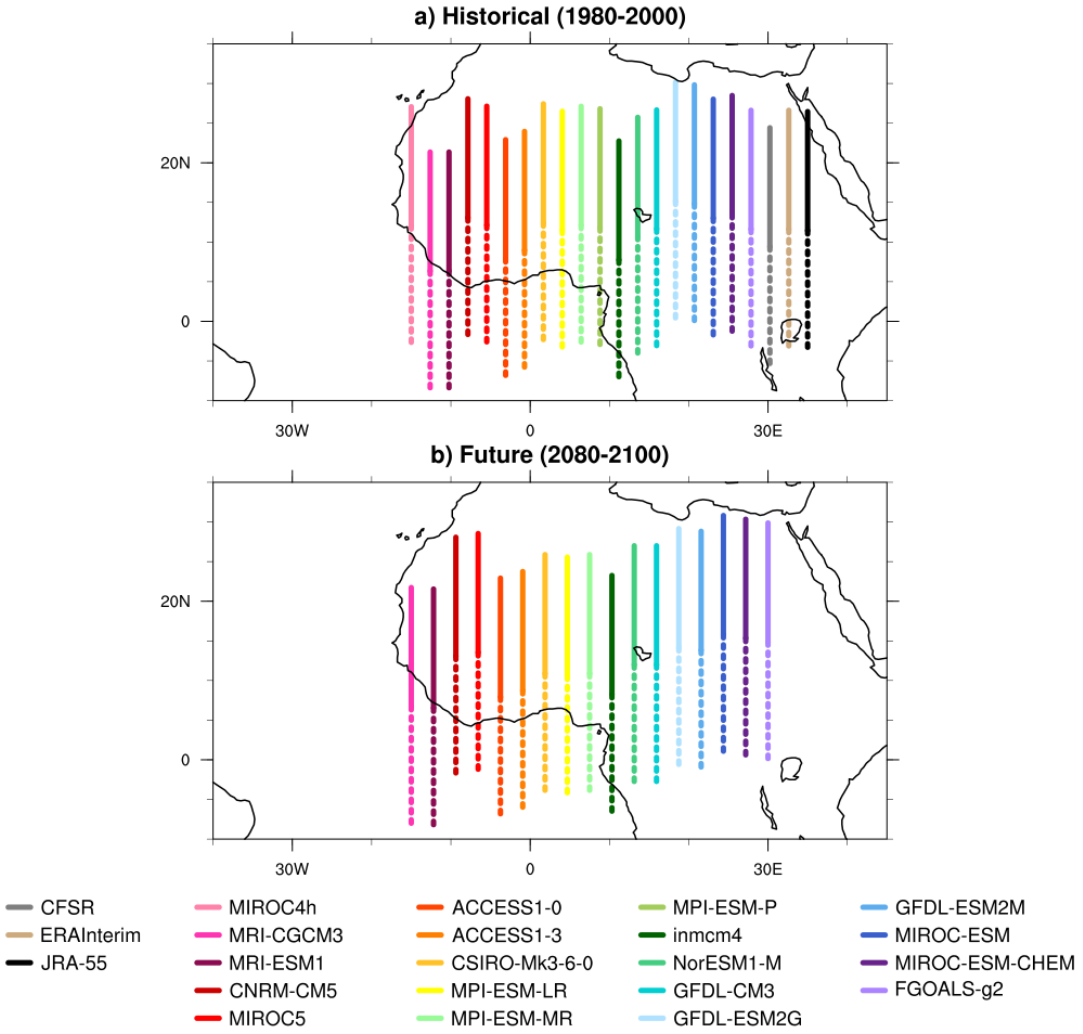



Figure 3.2: The northern (southern) track AEWs will be identified throughout the latitude band represented by the solid (dotted) portion of the line corresponding to each colored model for the historical period (top) and for the future (bottom). The boundary between the solid and dotted line represents the average summertime location of the AEJ in each model.

average monthly AEJ latitude are contained within 8° northward and 4° southward of the AEJ for each month.

Changes in the AEJ's average summertime latitude between the historical and future comparison periods are shown in Fig. 3.1c. Two models (ACCESS1-0 and CNRM-CM5) exhibit no latitudinal changes, six models shift to the south by 0.2°-1.6°, and nine models shift to the north by 0.2°-3.3°. The models are clustered into two groups which are separated by the mean latitude location of the AEJ within the reanalyses. It is interesting to note that the models possessing a more southern (below 10°N) average AEJ location in the historical simulations are more likely to retain a consistent AEJ latitude in the future. The models that show more variation from the past to the future are those located further north in the historical period.

Though the latitude of the AEJ changes throughout the summer months, this study will use the average summertime latitude of the AEJ in each model to separate the northern and southern AEW regions. This average AEJ location, and hence the northern and southern AEW regions, are adjusted between the historical and future simulations and illustrated by Fig. 3.2. Both the future and the historical average summertime AEJ latitude locations fall between the range of 6°N and 16°N, which is comparable to range typically cited in the literature, 10°N-15°N (Cook, 1999; Thorncroft and Hodges, 2001; Grist, 2002; Hall et al., 2006; Skinner and Diffenbaugh, 2013).

## 3.2 Historical Simulations of African Easterly Waves

### 3.2.1 Frequency

To establish the ability of the CMIP5 models to simulate the characteristics of AEWs, the number of AEWs each year of the historical period is shown in Fig.

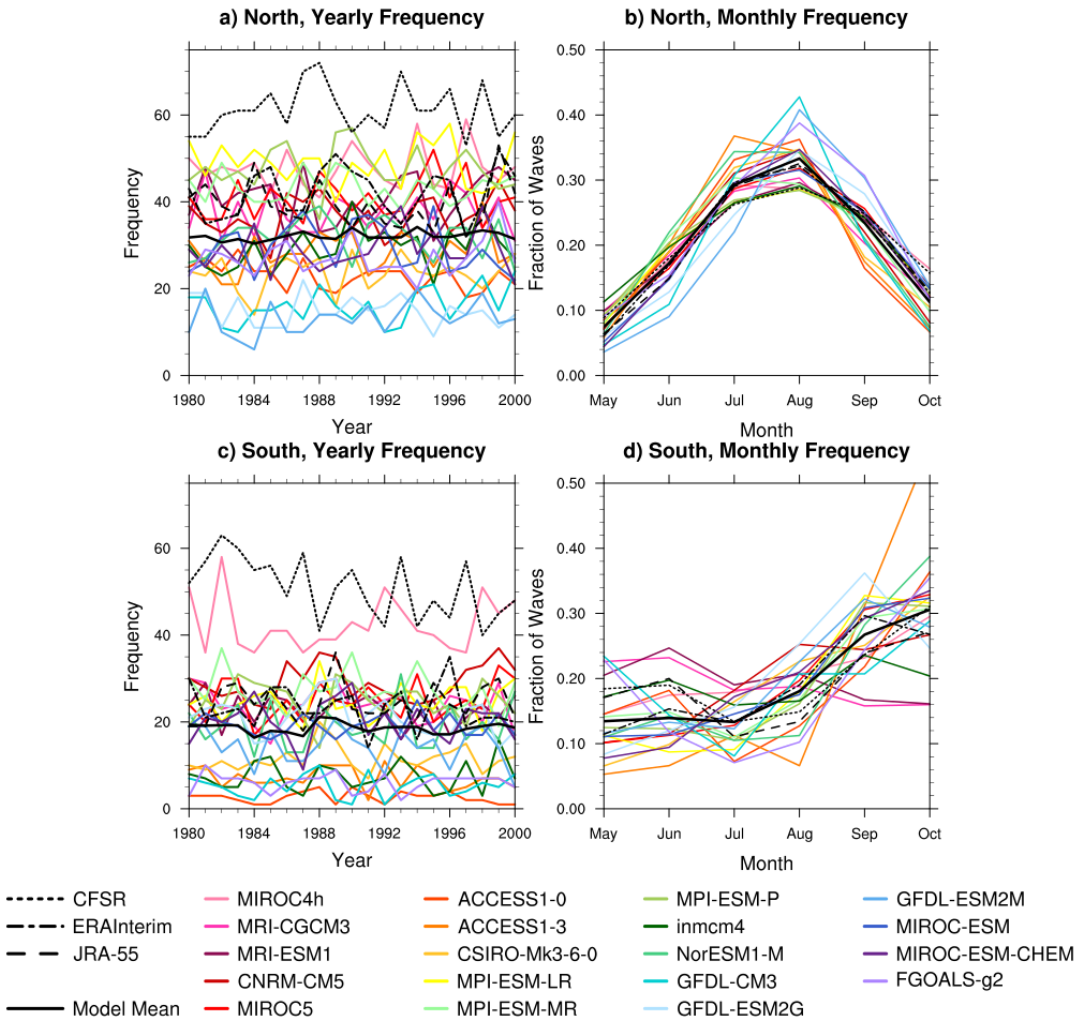



Figure 3.3: Yearly frequency of AEWs (left column; a,c) and monthly frequency normalized by the total number of AEWs resolved by each model individually (right column; b,d) during the historical period (1980-2000). Northern track values are displayed in the top row (a,b) with southern track values on the bottom (c,d). Patterned black lines represent each reanalysis. Solid black line is the model mean. Colors are representative of each CMIP5 model with warm (cool) colors corresponding to finer (coarser) resolution models.

3.3 for the northern (a) and southern (c) tracks, as well as for the reanalyses. In both the northern and southern historical tracks, the ERA-Interim and JRA-55 reanalyses fall very close to each other with their average number of waves resolved per year being 42.2 and 39.4, respectively, for the northern track and 23.3 and 24.5 for the southern track. The CFSR reanalysis resolves more waves than the other two reanalyses and more than most of the models, with an average 61.3 waves per year in the northern track and 50.9 in the southern track. This result could be due to the finer resolution of CFSR (0.5°) compared to ERA-Interim (0.75°) and JRA-55 (1.25°). This yields a multi-reanalysis average of 47.6 AEWs per year in the northern track and 32.9 in the southern track. The mean number of waves resolved per year within the CMIP5 models is 32.1 in the northern track and 18.6 in the southern track. The CMIP5 averages are less than the total reanalysis mean, however, they are closer to the yearly average number of waves when only considering the ERA-Interim and JRA-55 reanalyses, which have a more comparable resolution.

There is yearly variability in the frequency of AEWs, but also a spread between the models. Throughout the historical period, the number of waves detected each year in the models ranges from 6 to 72 for the northern waves (Fig. 3.3a) and 1 to 63 for the southern waves (Fig. 3.3c). The northern track waves have a tendency to fall in the range of 25-40 waves each year and the southern track waves have two modes, one around 5-10 waves per year and the second near 20-30.

The only model that ever observes more AEWs than the CFSR reanalysis is MIROC4h, which is the highest resolution CMIP5 model in this study (0.56°). This result supports those by Hodges et al. (2003) who discuss the benefits of increased resolution on track characteristics. Though, it is important to note that there is no clear relationship across all of the models between the resolution and the number of waves resolved. The finest resolution model (MIROC4h) is in the

upper bracket of number of waves resolved and many of the coarsest resolution models fall at the lower end of the number of waves resolved. However, there are also models that fall outside of this order. For example, FGOALS-g2 has the largest grid spacing, but it falls in the middle of the spread of models on the basis of average yearly frequency.

The overall average in the number of AEWs throughout the historical period remains consistent. This is an important result considering the Sahel drought in the 1980s and the association between AEWs and rainfall (see section 1). Fig. 3.3 (a,c) does not indicate a decreased number of AEWs in the 1980s compared to the 1990s. Therefore, the drought must have been due to other factors, such as a decreased supply of moisture (Hagos and Cook, 2008).

Frequency of AEWs are also examined as a function of month to establish the simulation of the seasonal cycle of the number of AEWs by the models. The northern track waves (Fig. 3.3b) show a steady increase in monthly frequency from June to August in both the reanalyses and the models, with peak frequency in August (ranging from 28.8% to 32.5% in reanalyses and 28.4% and 42.8% in the models), and a steady decrease in frequency from August to October. The monthly frequency of the southern track waves (Fig. 3.3d) show a much different pattern than those to the north. The southern track waves exhibit a fairly constant frequency from May to June, a decrease in frequency from June to July, and an increase from July to October in the reanalyses. Again, the reanalyses are consistent with each other and fairly close to the mean of the models— the only discrepancy comes from June to July where the model mean shows July frequencies consistent with May and June instead of decreasing as in the reanalyses.

### 3.2.2 Track Characteristics

The genesis location of an AEW track is defined at the initial longitude of the resolved/tracked AEW. The distribution of AEW genesis by longitude location shows distinct differences between the northern and southern track AEWs which can be partly due to the different topographic features in each region (Thorncroft and Hodges, 2001).

There are relatively few northern track AEWs forming in the furthest east longitudes (25°E - 45°E) the reanalyses and in the historical period of the models (Fig. 3.4a). The first sign of a favored genesis region occurs between 20°E and 25°E. This location coincides with the position of the Darfur mountains (15°N, 25°E; Fig. 1.1) and is cited by Mekonnen et al. (2006) and Thorncroft et al. (2008) as a location of orographic lift and frequent AEW initiation due to its proximity to the AEJ entrance region. A more broad peak in genesis occurs and extends from 20°E to the African coast, near 15°W. This peak is in conjunction with the Tibesti mountains (17°E), the Aïr Mountains (8°E), and the Ahaggar mountains (7°E), all of which exist at latitudes poleward of the AEJ (Fig. 1.1). Downstream of the Tibesti mountains, near 15°E, is actually considered the most successful region for triggering northern track AEWs (Thorncroft et al., 2008). This region's effectiveness in sparking AEW genesis is captured within the ERA-Interim and JRA-55 reanalyses, but not within CFSR or many of the models, which indicate similar abilities to initiate AEWs in this region compared to those just to its west.

The distribution from the models is generally consistent with the reanalysis mean except in the region between 5°E and 25°W. These contradictions align with the continental (5°E-15°W) and maritime (15°W-25°W) sides of the African coast. On the continental side, the models overestimate the propensity of AEW genesis compared to the reanalysis. This lack of genesis in the reanalyses is supported by Thorncroft and Hodges (2001) who show this region to be one of general northern

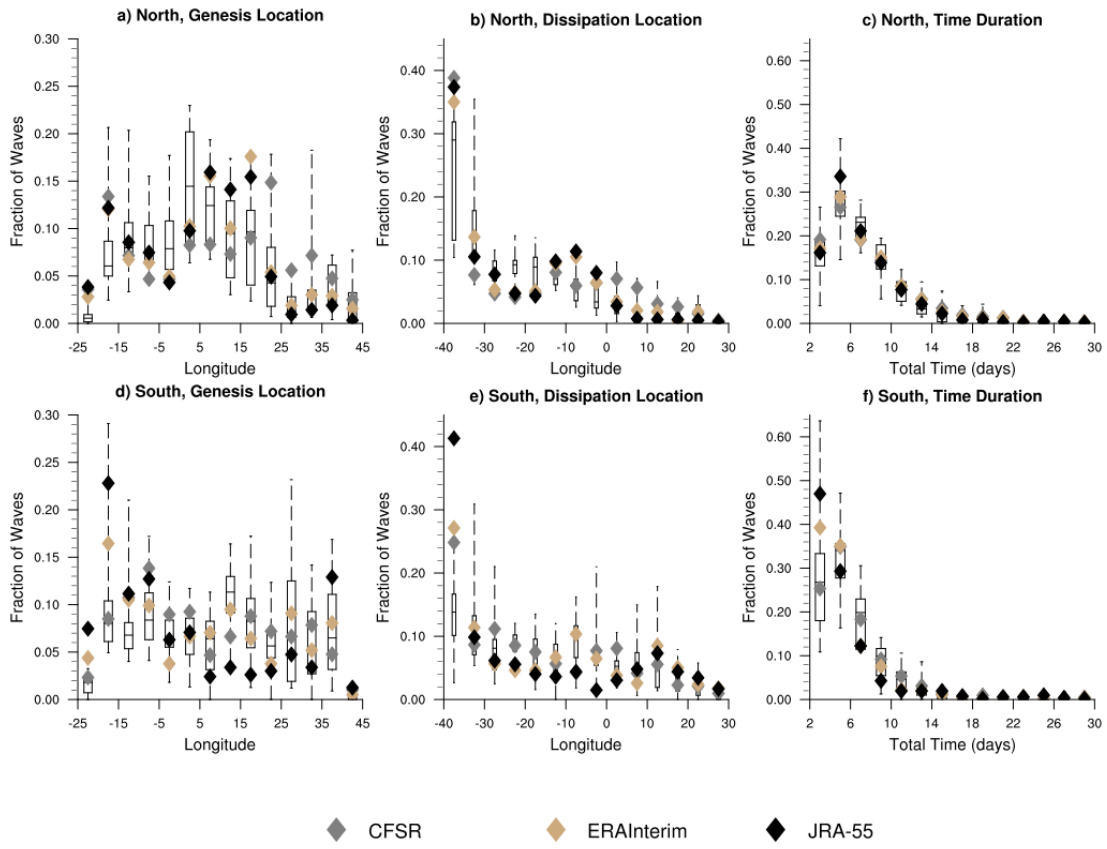



Figure 3.4: Box plots of the frequency of AEW genesis (left column; a,d), dissipation (middle column; b,e), and time duration (right column; c,f) in the CMIP5 models in each 5° longitude bin, normalized by the total number of AEWs resolved by each model individually during the historical period (1980-2000). Northern track values are displayed in the top row (a,b,c) with southern track values on the bottom (d,e,f). Diamond markers represent each reanalysis.

track dissipation as opposed to genesis. This bias is reversed on the maritime side of the coast, where the models underestimate genesis compared to reanalysis. It appears that the reanalyses capture a peak in AEW genesis just offshore (west of 15°W), whereas the models can not simulate this feature. The offshore peak in northern AEW genesis is one also described by Thorncroft and Hodges (2001).

The southern track AEWs in the historical simulation show increased genesis further east, near 35°E (Fig. 3.4d), when compared to the northern waves. This is consistent with the location of the Ethiopian Highlands (10°N, 35°E; Fig. 1.1), which is documented to be a main region of AEW genesis by Mekonnen et al. (2006). The longitude bins west of 35°E-40°E extending to the coast show an approximately constant median in normalized frequency, that then drops off over the water. Discrepancies between the CMIP5 models and the reanalyses occur between 15°E to 10°E, where the reanalysis mean resides in the lower quartile of the model spread, and between 5°W to 25°W, where the reanalysis mean of each longitude bin falls in the upper quartile of the distribution of the models. The Cameroon Mountains lie at 6°N, 12°E (Fig. 1.1) and could be responsible for the genesis peak within the models between 15°E to 10°E. The increased genesis near the western longitudes seen within the reanalyses can be attributed to the Guinea Highlands and the West African coast. The Guinea Highlands are situated near 8°N, 9°W and have been shown to increase convection that either strengthens existing AEWs or generates new ones (Ventrice et al., 2012; Martin and Thorncroft, 2015). The ERA-Interim and JRA-55 reanalyses show 16.4% and 22.7% of AEWs forming just offshore between 25°W and 15°W, which is consistent with the enhanced genesis region cited by Thorncroft and Hodges (2001) and Hopsch et al. (2007). The median of the CMIP5 models only simulates 8.0% of AEWs initiating in this offshore longitude bin. It is interesting to note that the models seem to be

able to detect favorable genesis regions due to African mountains, but they are less successful in handling the effects of the West African coast/Guinea Highlands.

The dissipation point of the simulated AEW tracks is valuable in determining the ability of the CMIP5 models to traverse the coast, which has shown to be a weakness (Martin and Thorncroft, 2015). AEW dissipation location also gives an idea about the distance the AEWs propagate into the Atlantic Ocean yielding implications for TC cyclogenesis (Hopsch et al., 2010).

The dissipation point of the AEW is defined by the longitude at the last time step in the resolved AEW track. In general, the greatest dissipation location of AEWs resides in the longitude bins furthest west (Fig. 3.4b,e). As the longitude domain of this study only extends to 40°W, the westernmost longitude bin from 40°W to 35°W also includes those tracks that continue westward beyond this longitude limit.

For the northern track waves (Fig. 3.4b), the reanalyses indicate a mean of 37% of the AEWs dissipating west of 35°W, while the historical simulations indicate a median of 29%. In the bins to the east, the fraction of AEWs dissipating in each longitude bin lessens, as expected from westward moving features. The main differences between the reanalyses and the historical CMIP5 models occur near the coastal longitudes. The model spread is small between 30°W and 10°W, showing about 9% of the total waves dissipate in each longitude bin. On the maritime side of the coast (west of 15°W), the models are consistently above the reanalyses in percentage of dissipation. On the continental side of the coast (east of 15°W), the models fall below the dissipation percentage within the reanalyses. The increased dissipation of AEWs before reaching the coast in the reanalyses is also shown through the track densities presented by Thorncroft et al. (2008).

Within the reanalyses, the northern track AEWs form in the eastern, continental longitudes and propagate across the continent, but dissipate before reaching the

coast. There is increased northern track AEW genesis just offshore (Fig. 3.4a), connected to a decrease in AEW dissipation in this area. New northern track AEWs form offshore that yield more dissipation in the westernmost longitudes compared to the models.

The models still show genesis in the eastern, continental longitudes, but instead of exhibiting coastal dissipation and regeneration, the models show more dissipation than the reanalyses in the longitudes immediately off the coast (15°W-30°W). In addition to a moderate frequency of dissipation just offshore, the models also display their largest peak in AEWs dissipation in the westernmost longitudes, with medians of 13% from 30°W to 35°W and 29% west of 35°W. Considering there is not a peak in offshore genesis within the models, in combination with a median of 68.3% of simulated AEWs dissipating on the ocean-side of the coast, promotes the idea that the models are able to traverse the AEWs across the coast, which has not been shown previously. There are still model biases in dissipation location, though, because after the AEWs traverse the coast, too many waves dissipate too soon as opposed to reaching the further west longitudes. These differences could be due to the simulated sea surface temperatures or the model representations of convection and latent heat release.

The dissipation location distribution of the southern track AEWs (Fig. 3.4e) is similar to the northern track distribution in its general increasing trend in dissipation as longitude bins are positioned further to the west. The magnitude of the frequency within westernmost longitude bins, though, is much different within the models. The reanalyses exhibit a distinct increase in dissipation west of 35°W, with an average of 31% of their AEWs dissipating in the furthest west longitude bin. However, all three reanalyses have a greater normalized frequency of dissipation in this longitude bin compared to every CMIP5 model. The CMIP5 models only show a median of 12% of AEWs dissipating west of 35°W. Hopsch et al. (2010) show a

majority of southern track AEWs traveling further into the Atlantic where they often initiate TCs. It seems the models, however, experience difficulties propagating the southern track AEWs into the longitudes of the mid-Atlantic. To the east, the models match up well with the reanalyses. They show very minor increases from 10°W to 5°W and from 10°E to 15°E, which are possibly in conjunction with the Guinea Highlands and the Cameroon Mountains, respectively.

The total time each AEW exists is a measure of the duration of the disturbance. A comparison of the duration between the reanalyses and the historical simulations can provide insight into the ability of the models to sustain the AEWs. This metric is related to both the genesis and dissipation locations, as the waves that travel a greater longitude distance will most likely exist for a longer time period. It is expected that time duration will carry analogous trends to those found within net longitude (shown in Appendix B). Note, the time duration of an AEW is restrained by the tracking algorithm's settings which mandate that it must propagate for at least two consecutive days.

The total time of existence for AEW tracks within the northern historical simulations mimics the distribution of the reanalyses (Fig. 3.4c). AEWs lasting from 2 to 4 days account for an average of 17.2% and 16.4% of the AEWs within the reanalyses and models, respectively. The frequency of AEW duration peaks between 4 and 6 days—encompassing an average of 29.5% of AEWs in the reanalyses and 26.5% within the models. Frequencies of AEWs lasting longer than 4-6 days steadily decrease and approach zero past 20 days of existence.

The time span of the southern track AEWs (Fig. 3.4f) peaks from 2 to 6 days. While the models generally follow the pattern of the reanalyses, there are discrepancies in the 2-4 day bin. The CFSR reanalysis falls within the interquartile range of the models, but ERA-Interim and JRA-55 detect a higher frequency of AEWs

with the 2-4 day lifetime, 39.1% and 46.8% respectively within the reanalyses and a median of 26.8% in the models.

The southern track waves agree with the northern AEWs in that fewer AEWs exist with the longer time durations. The southern track waves approach zero earlier, though, near 16 days of survival. The inconsistencies in skewness are also apparent through the differences in mean time durations between the northern (7.3 days in the reanalyses and 7.2 days in the models) and southern (6.7 days in the reanalyses and 6.4 days in the models) track AEWs. This conclusion is similar to the net longitude results (Appendix B) which show that more northern track AEWs are simulated to traverse a greater longitude distance, hence also extending their life time. This is a surprising result since the southern track AEWs are most commonly associated with tropical cyclogenesis (discussed further in section 1.2).

The average speed of AEWs is cited to be from 7-9 $ms^{-1}$ (Burpee, 1974, e.g.). The northern track AEWs in this study are found to have a mean average speed of 5.9 $ms^{-1}$ in the reanalyses and 5.8 $ms^{-1}$ in the CMIP5 models during the historical period. The normalized frequency distributions of average speed for the historical period (Fig. 3.5a) are similar between the CMIP5 model mean and the reanalyses, with peaks at 5.5 $ms^{-1}$ and 4.5 $ms^{-1}$ respectively and nearly symmetric shaped distributions, with small right skew. The majority of the models display distributions similar to the model mean, with FGOALS-g2 and inmcm4 being the exceptions that peak at $3ms^{-1}$.

For the average speed of the southern track waves (Fig. 3.5b), the reanalyses are shifted towards higher values compared to the speeds of the northern track waves, with a peak at 6.0 $ms^{-1}$ and a mean of 6.2 $ms^{-1}$. The model mean distribution of average speed is still nearly symmetric with a slight right skew. The average of the models has a distribution much like the northern track AEW speed distribution, peaking at 5.5 $ms^{-1}$ and averaging 5.9 $ms^{-1}$—lower than the southern

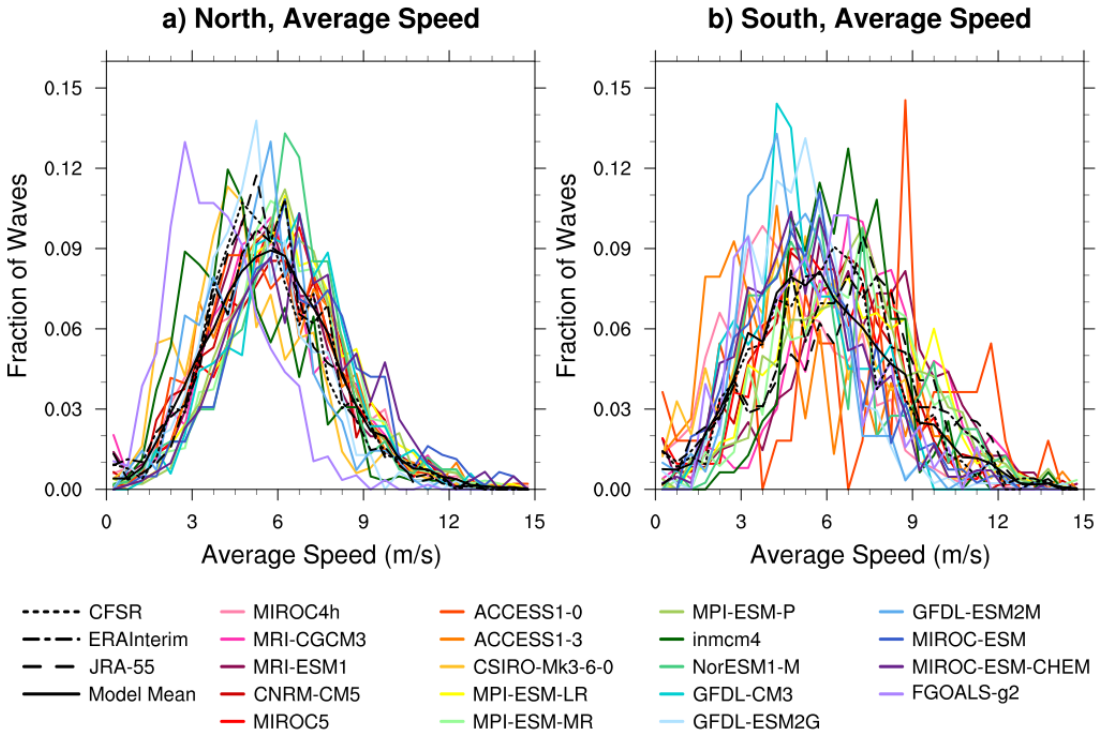



Figure 3.5: Frequency of the average speed of each AEW, normalized by the total number of AEWs resolved by each model individually during the historical period (1980-2000). Northern track values are displayed in (a) with southern track values in (b). Patterned black lines represent each reanalysis. Solid black line is the model mean. Colors are representative of each CMIP5 model with warm (cool) colors corresponding to finer (coarser) resolution models.

track reanalysis mean. When analyzing the average speeds of the southern track AEWs, inconsistencies between the models are documented within the historical simulation. The models are spread around the mean, showing peaks in frequency at distinctively higher and lower speeds compared to the model mean.

### 3.2.3 Intensity

The intensity of AEWs, whether measured by average CV or maximum CV, is an important characteristic to calibrate the models with the reanalyses and measure in the future due to the association between anomalously wet African summers and strong AEWs (Grist, 2002).

The average CV metric is calculated by averaging the CV over each time step that the AEW exists. Keep in mind that the tracking algorithm only considers AEWs with vorticity centers greater than $0.15\text{x}10^{-5}$ $s^{-1}$.

The normalized frequency distribution of average CV is shown for the historical period in Fig. 3.6; (a) shows the northern track and (c) shows the southern track, both of which exhibit a right skewed distribution. In the northern region, the reanalyses show a peak in frequency close to $0.70\text{x}10^{-5}$ $s^{-1}$, however the model mean distribution is shifted towards lower values and the majority of the models possess an average CV near $0.55\text{x}10^{-5}$ $s^{-1}$. This difference is also seen through the difference in the mean CV—$0.82\text{x}10^{-5}$ $s^{-1}$ for the reanalyses and $0.76\text{x}10^{-5}$ $s^{-1}$ for the ensemble of models. Disregarding the shift of the peak, the distributions appear to be of largely similar shapes. However, the skewness of the model mean is 1.00 indicating moderate skewness and the mean skewness of the reanalyses is 2.23, displaying high skewness. The skewness values demonstrate that even the right tail of the mean reanalysis distribution extends to more extreme average CV values compared to the mean distribution of the models.

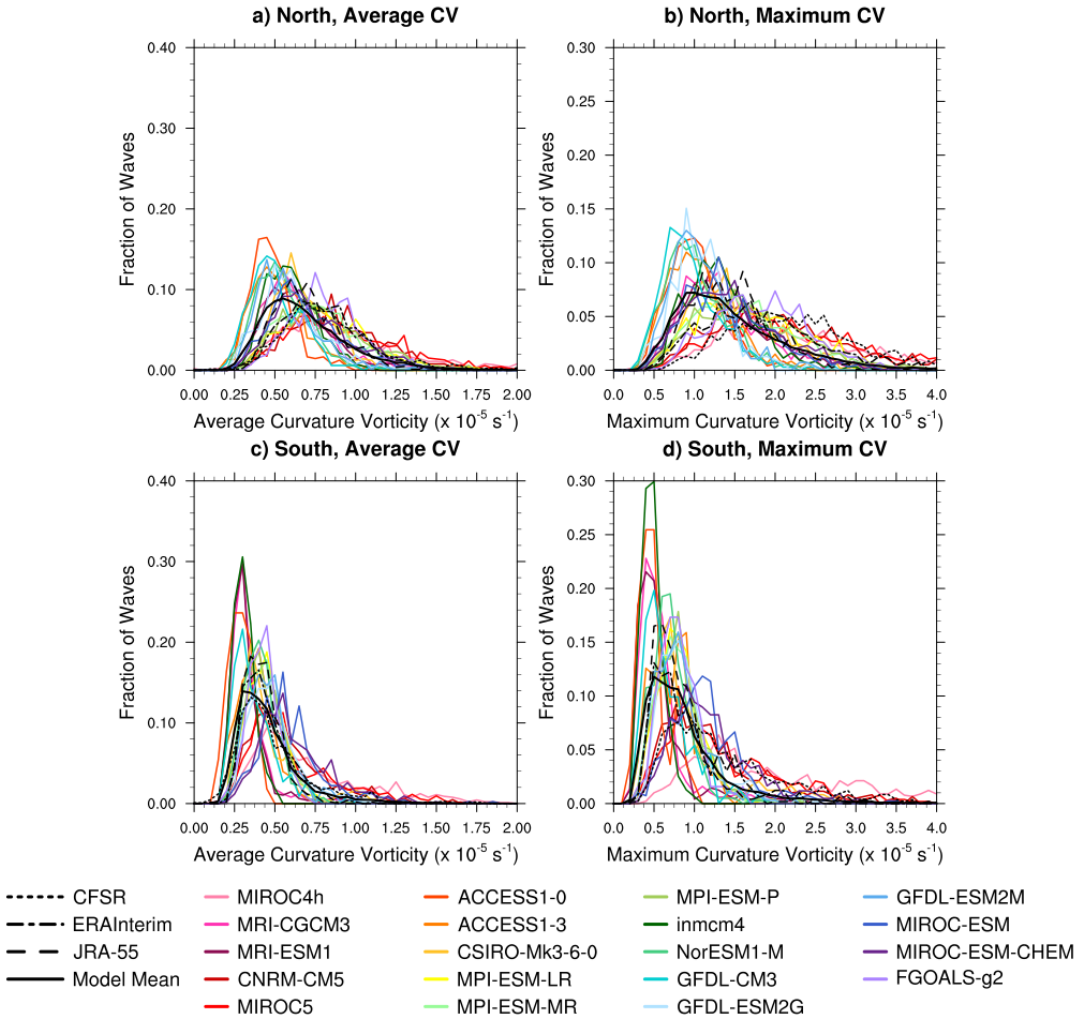



Figure 3.6: Frequency of the average CV (left column; a,c) and maximum CV (right column; b,d) of each AEW, normalized by the total number of AEWs resolved by each model individually during the historical period (1980-2000). Northern track values are displayed in the top row (a,b) with southern track values on the bottom (c,d). Patterned black lines represent each reanalysis. Solid black line is the model mean. Colors are representative of each CMIP5 model with warm (cool) colors corresponding to finer (coarser) resolution models.

The average CV distribution of the southern track historical AEWs (Fig. 3.6c) has an even more extreme right skew compared to the northern track. The CMIP5 models peak at a lower average CV ($0.30\text{x}10^{-5}$ $s^{-1}$) compared to the reanalyses which have their waves peaking in frequency at $0.40\text{x}10^{-5}$ $s^{-1}$ in average CV. The mean of all of the models gives an average CV of $0.52\text{x}10^{-5}$ $s^{-1}$ whereas the reanalysis mean is $0.49\text{x}10^{-5}$ $s^{-1}$. These findings can be compared to those in Bain et al. (2014) where CV is compared between ERA-Interim and the MetUM model. The ERA-Interim reanalysis mean CV falls at $0.41\text{x}10^{-5}$ $s^{-1}$ which is comparable to these results. The MetUM model, however, exhibits a peak in frequency at $0.15\text{x}10^{-5}$ $s^{-1}$—lower than the ERA-Interim reanalysis and also lower than the CMIP5 model mean in these results. In this study, the skewness values are 1.71 for the model mean distribution and 1.37 for the reanalysis mean distribution. The means and the skewness reveal the models must resolve more AEWs in the high end of average CV compared to the reanalyses, which is the opposite bias compared to the northern track.

The maximum CV is a measure of the maximum strength of each AEW which is linked to the propensity of AEWs to develop into TCs in the Atlantic Basin. Previous studies have noted the correlation between the low-level strength of the AEW as it leaves the African continent and it's ability to trigger the formation of a TC (Thorncroft and Hodges, 2001).

The distributions of the normalized frequencies of maximum CV (Fig. 3.6b,d) share many similar features to those of average CV (Fig. 3.6a,c). The model mean distribution of the northern track AEWs in the historical period possesses a peak frequency at $1.00\text{x}10^{-5}$ $s^{-1}$, which resembles the JRA-55 reanalysis closer than the other two reanalyses. CFSR and ERA-Interim have peaks shifted towards higher maximum CV values, hence they also attain higher means and smaller skewness. Therefore, the average peak in the models ($1.00\text{x}10^{-5}$ $s^{-1}$) is lower

than the average peak of the reanalysis mean which lies near 1.5x10$^{-5}$ s$^{-1}$. The overall mean maximum CV follows this trend as well, falling at 2.02x10$^{-5}$ s$^{-1}$ in the reanalyses and 1.67x10$^{-5}$ s$^{-1}$ in the models.

The distribution of the maximum intensity of the southern track AEWs in the historical simulations (Fig. 3.6d) shows a large, distinct peak at 0.50x10$^{-5}$ s$^{-1}$ and a right skew. There also appears to be a secondary peak of five models (MIROC4h, CNRM-CM5, MIROC5, MIROC-ESM, MIROC-ESM-CHEM) near 1.0x10$^{-5}$ s$^{-1}$. The JRA-55 and ERA-Interim reanalyses show their peak frequency at 0.50x10$^{-5}$ s$^{-1}$, aligning with the primary peak, whereas CFSR resembles the shape of the models comprising the secondary peak. The overall mean maximum CV for the CMIP5 models is 1.13x10$^{-5}$ s$^{-1}$ and 1.21x10$^{-5}$ s$^{-1}$ for the reanalyses.

The most noticeable difference between the maximum strength of the northern and southern track AEWs is the value of the primary peak within the models—1.0x10$^{-5}$ s$^{-1}$ for the northern AEWs and 0.5x10$^{-5}$ s$^{-1}$ for the southern AEWs. Consistent with the northern track AEWs displaying greater strength through the location of their peak frequencies, the increased strength of the northern AEWs is also highlighted through the right tails. The right tail of the northern track extends out to near 3.5x10$^{-5}$ s$^{-1}$ and the tail of the southern track only reaches 2.5x10$^{-5}$ s$^{-1}$, accentuating the greater range of maximum intensity for the northern AEWs.

The yearly average intensity of AEWs (measured by average CV or maximum CV; Fig. 3.7) can be useful in linking years of abnormally high/low rainfall and years with more/less Atlantic TC. In both the northern (Fig. 3.7a) and southern (Fig. 3.7c) track AEWs, yearly averages of CV vary slightly between years but the general trend across the historical and future periods shows consistent average CV over the 20 year historical period. This is significant since much of the 1980's was dominated by a Sahel drought. As shown previously (section 3.2.1), the drought was not caused by a lack of AEWs, and Fig. 3.7 shows shows it is also not

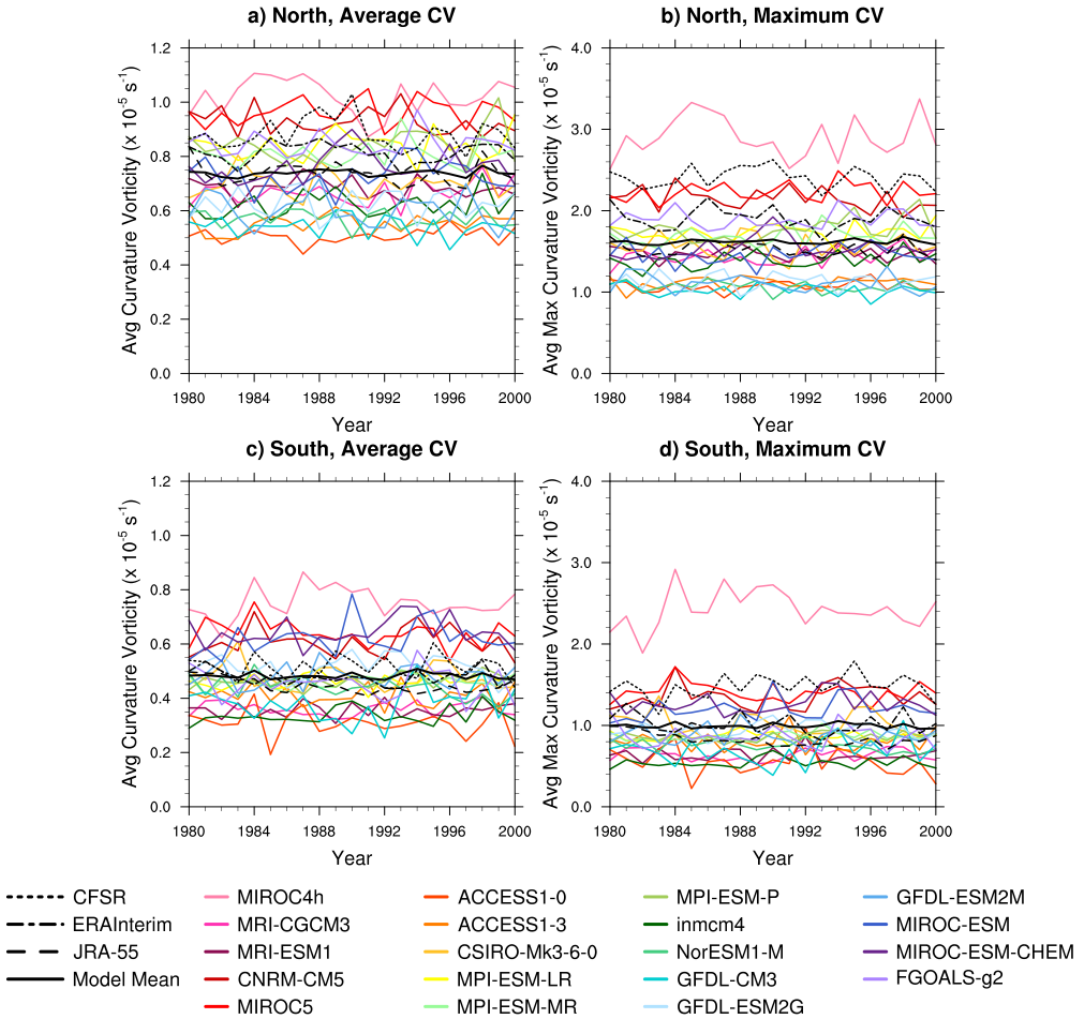



Figure 3.7: Yearly average CV (left column; a,c) and yearly maximum CV (right column; b,d) of each AEW, during the historical period (1980-2000). Northern track values are displayed in the top row (a,b) with southern track values on the bottom (c,d). Patterned black lines represent each reanalysis. Solid black line is the model mean. Colors are representative of each CMIP5 model with warm (cool) colors corresponding to finer (coarser) resolution models.

related to AEWs of less intensity. Therefore, the Sahel drought of the 1980's must be attributable to other factors, such as a lack of moisture (Hagos and Cook, 2008). The AEWs within the reanalyses in the northern (southern) track fluctuate above and below a mean of 0.81x10$^{-5}$ s$^{-1}$ (0.48x10$^{-5}$ s$^{-1}$). The CMIP5 models in each region are equally spread above and below the reanalyses. In the northern region, the CMIP5 models have a yearly average CV ranging from 0.51x10$^{-5}$ s$^{-1}$ to 1.02x10$^{-5}$ s$^{-1}$ with a mean of 0.73x10$^{-5}$ s$^{-1}$. The southern track range in average intensity is smaller than in the northern track, spanning from 0.31x10$^{-5}$ s$^{-1}$ to 0.75x10$^{-5}$ s$^{-1}$ around a mean of 0.48x10$^{-5}$ s$^{-1}$. The greater magnitude of the average yearly CV in the northern AEWs compared to the southern AEWs is expected after the discussion regarding average CV frequency distribution in Fig. 3.6.

The final measure of changing AEW intensity involves the average maximum CV each year. This metric is important as it may provide support for years experiencing anomalous Sahel rainfall or Atlantic TC activity. The reanalyses simulate northern and southern AEWs that have a mean maximum CV of 1.94x10$^{-5}$ s$^{-1}$ and 1.11x10$^{-5}$ s$^{-1}$, respectively, during the historical period (Fig. 3.7b,d). The majority of the historical models fall below the reanalysis mean, with only three models above the reanalysis mean in the northern track and five above in the southern track. The three models with waves of higher average maximum intensity compared to the reanalyses are MIROC4h, CNRM-CM5, and MIROC5 in the northern track. These models are among the top five finest resolutions models. In the southern track, the five models producing AEWs of higher average maximum intensity compared to the reanalyses are MIROC4h, CNRM-CM5, MIROC5, MIROC-ESM, and MIROC-ESM-CHEM. While the first three models are among the finest resolution models, MIROC-ESM and MIROC-ESM-CHEM are grouped in the three coarsest resolution models. This suggests that the ability to resolve

the strongest AEWs is more heavily dependent on resolution in the northern track, but other factors, such as convective parameterizations, are of more importance in the southern track. The models cluster around each other within the range of 1.02x$10^{-5}$ $s^{-1}$ to 2.23x$10^{-5}$ $s^{-1}$ for the northern track waves and 0.55x$10^{-5}$ $s^{-1}$ to 1.41x$10^{-5}$ $s^{-1}$ for the southern track waves. MIROC4h falls above the cluster in both the northern and southern distributions, averaging a maximum CV of 2.91x$10^{-5}$ $s^{-1}$ and 2.43x$10^{-5}$ $s^{-1}$ respectively. MIROC4h is the finest resolution model, which may be the key factor in its ability to resolve the most intense AEWs. Consistent with the discussion involving the frequency distribution of maximum CV, the yearly distributions of maximum CV also resolve southern track AEWs with maximum intensities less than those of northern track AEWs.

## 3.3 Accumulated Historical Biases

It is often assumed that the models that best simulate the past will be most representative of future simulations. Following this theory, we create a comprehensive objective measure of AEW bias in historical simulations using the characteristics presented so far. A summary of the historical biases is illustrated in Fig. 3.8 for the northern track waves and Fig. 3.9 for the southern track waves. The biases are calculated as the deviation from the mean of the three reanalyses (model − reanalysis mean). Therefore, positive errors (reds) correspond to a value that is greater in the model than the reanalyses. Negative errors (blues) correspond to a model value that is less than the reanalysis mean. Colors near white indicate a good representation of the reanalyses by the model.

The individual characteristics and biases shown in the tables are as follows from top to bottom: yearly mean frequency, standard deviation of the yearly frequency, root mean square error of monthly frequency, ratio of normalized frequency of AEW genesis occurring on the ocean side of the coast (between 20°W and 15°W)

to that on the continental side of the coast (between 15°W and 10°W) [e.g., the reanalyses have a high ocean:land genesis ratio in the northern track since they show a peak in AEW genesis on the ocean side of the coast], ratio of normalized frequency of AEW dissipation occurring on the ocean side of the coast (between 20°W and 15°W) to that on the continental side of the coast (between 15°W and 10°W) [e.g., the reanalyses have a low ocean:land genesis dissipation ratio in the northern track since they show a peak in AEW dissipation on the continental side of the coast], sum of the normalized dissipation frequencies occurring at longitudes over the African continent, mean of AEW duration, skewness of AEW duration, mean of AEW net longitude (Appendix B), skewness of AEW net longitude (Appendix B), AEW average CV, skewness of average CV, average of AEW maximum CV, skewness of AEW maximum CV, root mean square error of the monthly distribution of average CV (Appendix C), AEW mean average speed, and standard deviation of the average speed. The absolute values of each column of biases are summed (and divided by 8 for use with this colorbar) and displayed in the bottom row. Models with the lowest total error are considered the least biased and models with the highest total error are the most biased.

First considering the northern track waves, the characteristics in which the models replicate the reanalyses the closest are the distribution of monthly normalized frequency and the average AEW duration (measured by both net longitude and total time). The mean and standard deviation of average speed are also well replicated with only some evidence of overestimation in the models compared to the reanalyses. There are large differences regarding the genesis and dissipation locations of AEWs, particularly near the coast. The models have too few waves forming and too many waves dissipating on the ocean side of the coast compared to the reanalyses which tend to have increased dissipation on the continental side of the coast and increased genesis just offshore. The distributions of average CV and

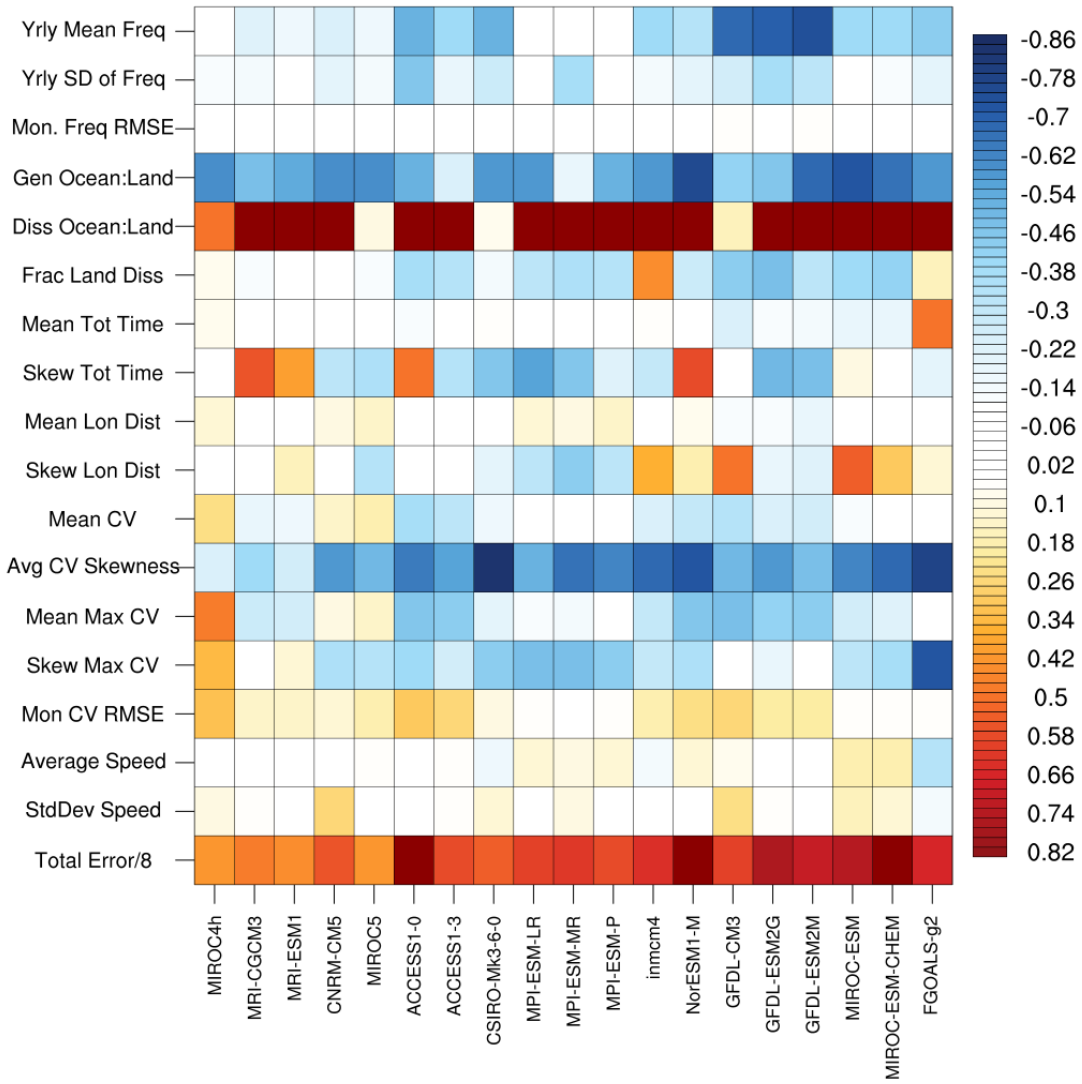



Figure 3.8: Historical biases of northern track AEW characteristics (see text for descriptions), calculated by subtracting the reanalysis mean from each model and converting to a percent error. The sum of the absolute value of each error is shown in the bottom row. Errors in monthly characteristics are calculated by root mean square error from the reanalysis mean. Models are listed with the finest resolutions on the left and coarsest resolutions on the right. Positive errors (reds) correspond to a value that is greater in the models than the reanalyses. Negative errors (blues) correspond to a model value that is less than the reanalysis mean. Colors near white indicate a good representation of the reanalyses by the model.

average maximum CV have less right tailed skewness than the reanalyses. This signalizes a greater frequency of the most intense waves in the reanalyses. Only moderate differences exist between the mean yearly frequency of AEWs resolved within the models and the reanalyses. The models simulate fewer waves per year and underestimate the standard deviation of the frequency of AEWs. The intensity of the AEWs (mean CV and max CV) is most often underestimated by the models, but some models indicate overestimation, and some replicate similar intensities to the reanalyses. The remaining characteristics show disagreeing biases among the models.

The magnitude of the total error (bottom row of Fig. 3.8) shows the five models with the overall best representation of AEWs compared to the reanalyses are MIROC5, MIROC4h, MRI-ESM1, MRI-CGCM3, and CSIRO-Mk3-6-0. Four of five of these models fall within the top five finest resolution models, supporting the hypothesis that increased resolutions increases the models ability to simulate realistic AEWs (Hodges et al., 2003; Bain et al., 2014). As future data for MIROC4h was not available, the least biased northern track models to be used in section 3.4 will also include CNRM-CM5. The models with the highest aggregated bias in the northern track are ACCESS1-0, NorESM1-M, MIROC-ESM-CHEM, GFDL-ESM2G, and MIROC-ESM. These highly biased models are generally those with coarser model grid spacings; however, FGOALS-g2 has the coarsest resolution and is not included in the five models with the highest biases.

Contrasting the northern track waves where most of the models possess biases of the same sign for an individual characteristic, the southern track waves have much more disagreement on both the sign and the magnitude of the model biases. Like the northern track, though, the southern track historical simulations of the models are best at replicating the monthly normalized frequency and the mean duration (mean net longitude or mean total time) of the AEWs. The models are

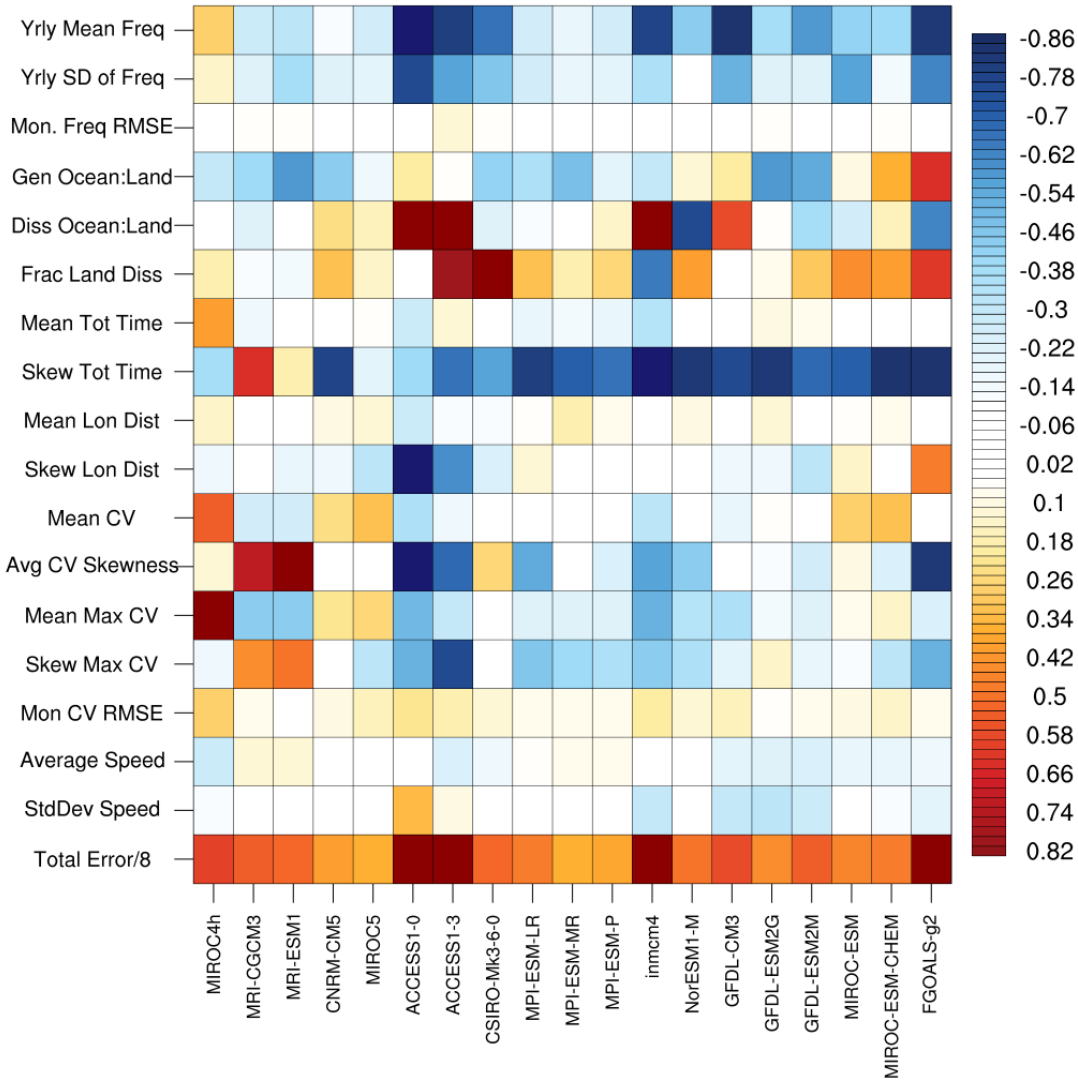



Figure 3.9: As in Fig. 3.8 but for southern track AEWs.

moderately successful in representing the skewness of the total longitude distribution, the average CV, and the monthly distribution of CV—in that, many of the models align with the reanalyses, but a few fall above and a few fall below. The most distinct biases are found in the mean and standard deviation of yearly frequency, the skewness of total time, the mean and skewness of maximum CV, and the mean and standard deviation of average speed. Similar to the northern track waves, the yearly frequency and standard deviation of the southern track waves are underestimated by the models compared to the reanalyses. MIROC4h is the only model showing a positive bias for yearly frequency. The largest biases are exhibited in the skewness of the time duration. The negative magnitudes indicate the reanalyses have a greater right skew attributed to a greater frequency of AEWs that exist for the longest lifetimes. The mean and skewness of the maximum CV show predominantly negative biases, associated with AEWs in the reanalyses having stronger maximum intensities and a greater frequency of AEWs with maximum CV in the most intense categories. Average speeds of the southern track waves in the models are not too different from the reanalysis mean; however, they do show slight tendencies to underestimate the mean and standard deviation. The remaining characteristics (involving genesis/dissipation locations and the skewness of average CV) display both positive and negative biases making it difficult draw a specific conclusion regarding the model biases.

The models with the smallest total error are MIROC5, MPI-ESM-MR, MPI-ESM-P, CRNM-CM5, and GFDL-ESM2G. Future data for MPI-ESM-P was not available, so the five least biased southern track models used in section 3.4 will also include MIROC-ESM. As opposed to the models with the best representation of the northern track waves, these top five models do not have the finest resolutions, but they fall in the mid-range among the spread of model resolutions. The models

containing the highest overall bias compared to the reanalysis mean are ACCESS1-0, ACCESS1-3, inmcm4, FGOALS-g2, and MIROC4h. Future data for MIROC4h was not available, so the five most biased southern track models to be used in section 3.4 will also include GFDL-CM3. The highest bias models in the southern track also span the range of grid spacings, including FGOALS-g2, the coarsest resolution model of this study, and MIROC4h, the finest resolution model.

## 3.4 Future Simulations of African Easterly Waves

To determine the extent to which the characteristics presented in section 3.2 are changing in the future, this section will focus on the net change in those characteristics from 1980-2000 to 2080-2100. The distributions of each characteristic in the future can be found in Appendix D.

### 3.4.1 Frequency

The changes between the historical and future periods are displayed in Fig. 3.10 (a,c) and Tables 3.1 and 3.2. The yearly frequencies during the future period show less clustering and a more consistent distribution in an average range of 18.0 to 46.3 waves per year for the northern track and 3.0 to 36.5 waves per year for the southern track.

For the northern track waves, four models (MRI-ESM1, MIROC5, MIROC-ESM-CHEM, and MRI-CGCM3) show the average number of AEWs in the past and future changes by less than 1 AEW. Three models (MIROC-ESM, MPI-ESM-LR, and inmcm4) show decreases in the frequency of future AEWs ranging from 1.3 to 5.0 less waves on average (percent changes ranging from $-4.52\%$ to $-16.83\%$). The remaining ten models show increases between an average of 1.6 and 7.6 additional waves in the future (percent changes ranging from $+6.87\%$ to $+51.28\%$).

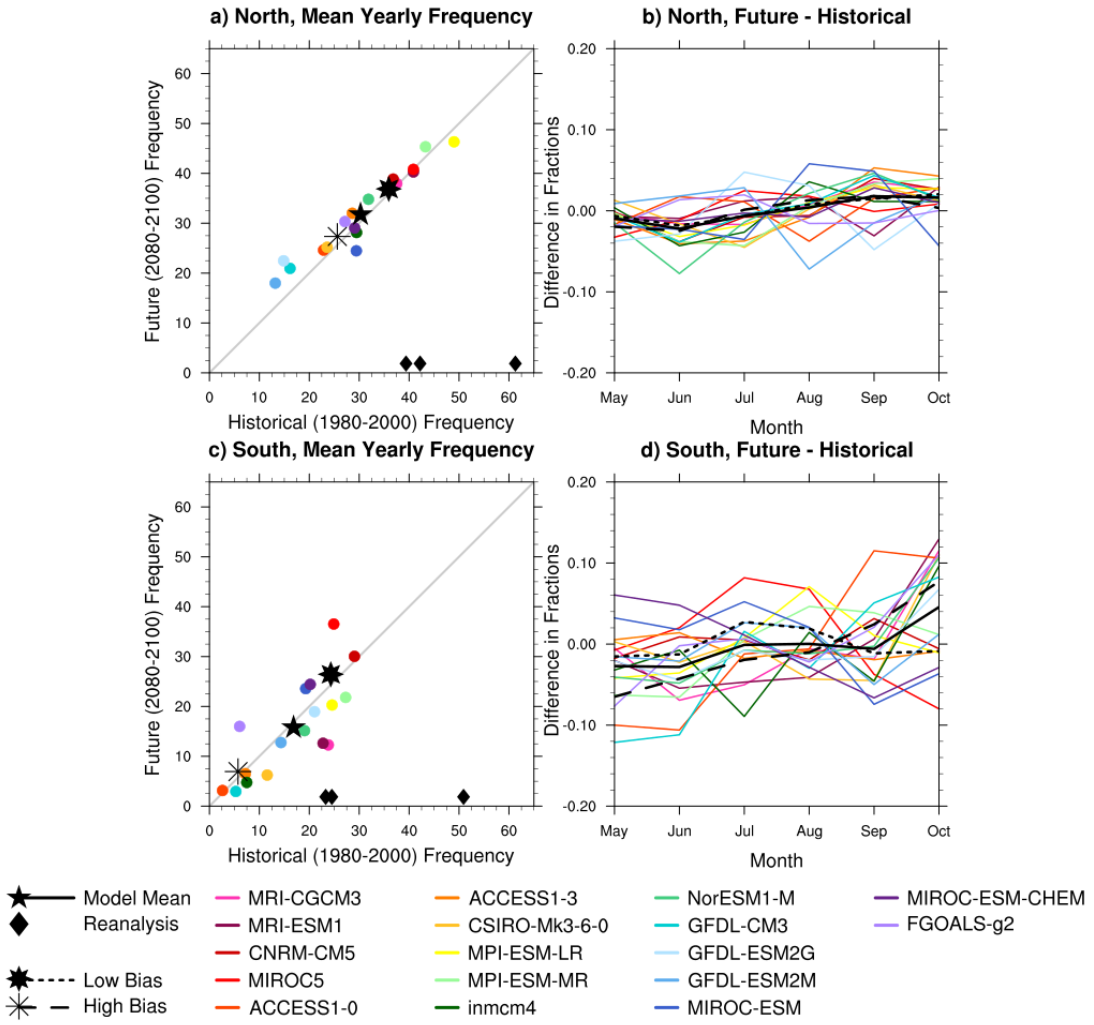



Figure 3.10: Average number of AEWs for each model in the historical and future periods is shown in the left column (a,c) with the grey line representing no change in frequency between the time periods, the black diamonds representing the reanalysis averages, and the stars representing model means. The difference in normalized monthly AEW frequencies (future − historical) is shown on the right (b,d) with the solid black line representing the overall model mean and the patterned black lines representing the least/most biased model mean. Northern track values are displayed in the top row (a,b) with southern track values on the bottom (c,d). Colors are representative of each CMIP5 model with warm (cool) colors corresponding to finer (coarser) resolution models.

Table 3.1: Average frequency of northern track AEWs during the historical and future periods for each model along with the raw difference (future − historical) and the percent change.

| **Model** | **Historical** | **Future** | **Raw Change** | **Percent Change** |
|---|---|---|---|---|
| MRI-CGCM3 | 37.5 | 38.0 | +0.4 | +1.14% |
| MRI-ESM1 | 40.9 | 40.3 | −0.6 | −1.40% |
| CNRM-CM5 | 36.8 | 38.9 | +2.0 | +5.56% |
| MIROC5 | 40.9 | 40.8 | 0.0 | −0.12% |
| ACCESS1-0 | 22.9 | 24.6 | +1.8 | +7.71% |
| ACCESS1-3 | 28.6 | 32.0 | +3.4 | +11.81% |
| CSIRO-Mk3-6-0 | 23.6 | 25.2 | +1.6 | +6.87% |
| MPI-ESM-LR | 49.0 | 46.3 | −2.7 | −5.44% |
| MPI-ESM-MR | 43.3 | 45.3 | +2.0 | +4.73% |
| inmcm4 | 29.5 | 28.1 | −1.3 | −4.52% |
| NorESM1-M | 31.9 | 34.8 | +3.0 | +9.27% |
| GFDL-CM3 | 16.1 | 21.0 | +4.8 | +29.79% |
| GFDL-ESM2G | 14.9 | 22.5 | +7.6 | +51.28% |
| GFDL-ESM2M | 13.2 | 18.0 | +4.8 | +36.46% |
| MIROC-ESM | 29.4 | 24.5 | −5.0 | −16.83% |
| MIROC-ESM-CHEM | 29.1 | 29.0 | 0.0 | −0.16% |
| FGOALS-g2 | 27.1 | 30.3 | +3.2 | +11.75% |
| Overall Model Mean | 30.3 | 31.7 | +1.5 | +0.05% |
| Low Bias Model Mean | 35.9 | 36.6 | +0.7 | +0.02% |
| High Bias Model Mean | 25.6 | 27.1 | +1.5 | +0.06% |

Table 3.2: As in Table 3.1, but for southern track AEWs.

| **Model** | **Historical** | **Future** | **Raw Change** | **Percent Change** |
|---|---|---|---|---|
| MRI-CGCM3 | 23.8 | 12.3 | −11.5 | −48.40% |
| MRI-ESM1 | 22.8 | 12.6 | −10.1 | −44.56% |
| CNRM-CM5 | 29.0 | 30.0 | +1.0 | +3.44% |
| MIROC5 | 24.9 | 36.5 | +11.6 | +46.65% |
| ACCESS1-0 | 2.6 | 3.1 | +0.5 | +20.00% |
| ACCESS1-3 | 7.2 | 6.5 | −0.7 | −9.27% |
| CSIRO-Mk3-6-0 | 11.6 | 6.2 | −5.3 | −46.09% |
| MPI-ESM-LR | 24.6 | 20.3 | −4.3 | −17.44% |
| MPI-ESM-MR | 27.3 | 21.8 | −5.5 | −20.07% |
| inmcm4 | 7.5 | 4.8 | −2.7 | −36.31% |
| NorESM1-M | 19.0 | 15.1 | −3.9 | −20.50% |
| GFDL-CM3 | 5.3 | 3.0 | −2.3 | −44.14% |
| GFDL-ESM2G | 21.0 | 19.0 | −2.1 | −9.95% |
| GFDL-ESM2M | 14.3 | 12.8 | −1.6 | −10.96% |
| MIROC-ESM | 19.3 | 23.6 | +4.3 | +22.22% |
| MIROC-ESM-CHEM | 20.2 | 24.4 | +4.2 | +20.99% |
| FGOALS-g2 | 6.0 | 16.0 | +10.0 | +164.57% |
| Overall Model Mean | 16.9 | 15.8 | −1.1 | −0.06% |
| Low Bias Model Mean | 24.3 | 26.2 | +1.9 | +0.08% |
| High Bias Model Mean | 5.7 | 6.7 | +1.0 | +0.17% |

The GFDL models resolve the fewest AEWs in the historical simulations, but show the largest increases in future AEW frequency. The overall mean change in frequency of AEWs between the past and future is an increase of 1.5 waves per year (+0.05%), with the lowest and highest biased models showing an average increase of 0.7 (+0.02%) and 1.5 (+0.06%) waves per year, respectively. Though the average increases are small, they support the results from Martin and Thorncroft (2015) who showed an increase in AEW activity within the northern region in the future. The future changes are contained between −5.0 and +7.6 waves per year, producing a small spread among the models for the northern region, which also supports the findings by Martin and Thorncroft (2015).

The change in yearly frequencies of the southern track waves are more varied than the northern track with two models (ACCESS1-0 and ACCESS1-3) indicating no change, five models showing frequency increases up to 11.6 additional waves per year (+46.65%), and ten models showing decreases up to 11.5 fewer waves per year (−48.40%). The mean of all the models predicts an average decrease of 1.1 waves per year (−0.06%), with the lowest and highest biases models showing an increase of 1.9 (0.08%) and 1.0 waves per year (+0.17%), respectively. The disagreement regarding future changes in yearly frequency of the southern track waves, aligns with the inconsistencies in future trends of precipitation (Skinner and Diffenbaugh, 2013) and EKE (Martin and Thorncroft, 2015) within the southern region.

As far as seasonal frequency is concerned, the models in the future show a seasonal cycle of nearly identical structure to that of the historical period for both the northern and southern track AEWs (Fig. D.1b,d). Fig. 3.10b shows future changes in the seasonal cycle of the northern track. Roughly half of the models simulate decreases in normalized frequency in the early summer and increases in normalized frequency in late summer, broadening the August peak. The other half of the models show the opposite trend. The opposing changes appear to cancel

each other out, resulting in an overall model mean, as well as a high biased and low biased model mean, that predict negligible changes in the seasonality of northern AEWs in the future. The shape of the distribution and the location of the August peak coincide with the findings by Martin and Thorncroft (2015), but Martin and Thorncroft (2015) show a more pronounced seasonal cycle in EKE for the future northern track waves. Though this study does not support a more sharply defined seasonal cycle in future AEW frequency, it is not necessarily expected that the future trends in the seasonal frequency of AEWs match those of EKE.

The most noticeable future change in the southern track seasonal frequency distribution occurs at the end of the season (Fig. 3.10d). In October, there is an average increase in frequency by 4.6% in the future (i.e. an increase of 5% means the fraction of waves occurring in October could have increased from 5% to 10%, or 20% to 25%, etc). The spread of the models is large, yielding an overall model mean with a decrease ($-2.8\%$) in normalized frequency in May and June, approximately constant frequency from July to September, and an increase ($+4.6\%$) in frequency during October. A similar, but more drastic pattern is found through the changes of the highest bias models— a decrease of $-6.5\%$ in May, $-4.3\%$ in June, $-1.9\%$ in July, $-1.0\%$ in August, and increases of $+2.5\%$ in September, and $+7.7\%$ in October. The mean of the low biased models still shows a shift in seasonality, but not as far towards the later months, with decreases near $-1.5\%$ in May and June, increases near $+2.5\%$ in July and August, and decreases near $-1.0\%$ in September and October. The decreased frequency in early summer is consistent with the decline in EKE in May and June (Martin and Thorncroft, 2015). A shift in the seasonality of the southern track AEWs towards the later summer months could have implications in shifting the timing of the Atlantic TC season towards later dates as well.

A final note of comparison between the northern and southern distributions is the smaller spread between the models when simulating the seasonality of northern track AEWs (between −7.7% and +5.8%) and the larger range of the southern track AEWs (between −12.1% and +12.9%). This outcome again points to the consistency in future trends within the northern track and the disagreement/contradiction among the models in representing changes to southern track AEWs.

### 3.4.2 Track Characteristics

The distribution of northern track AEW genesis in the future shows similar characteristics within the models to those from the past, yielding individual model differences between −7.6% and +6.5% (Fig. 3.11a) and an overall model mean that never exceeds a change of +/−1.3% for any longitude bin. The low and high biased models also mimic the changes of the overall model mean, not changing by more than +/−1.8% and +/−3.1%, respectively. The multi-model means show the genesis location of northern AEWs is not changing in the future. This result can be attributed to the fact that much of the genesis is linked to topography which will remain constant in the future.

As for the southern track, the future distribution of AEW genesis looks largely similar to that from the historical simulations with a spread in future projected differences that straddle the zero line (never exceeding changes greater than +/−1.7%), as shown in Fig. 3.11d. Once again, the genesis locations of southern track AEWs are not showing significant changes in the future. There is more variation in the low (+/−2.7%) and high (+/−3.5%) biased model means, but the locations of these changes do not show any clear patterns in changes to genesis locations. Also note the span of the future changes in the southern track waves show more variability between the individual models (−21.5% to +17.3%), compared to the

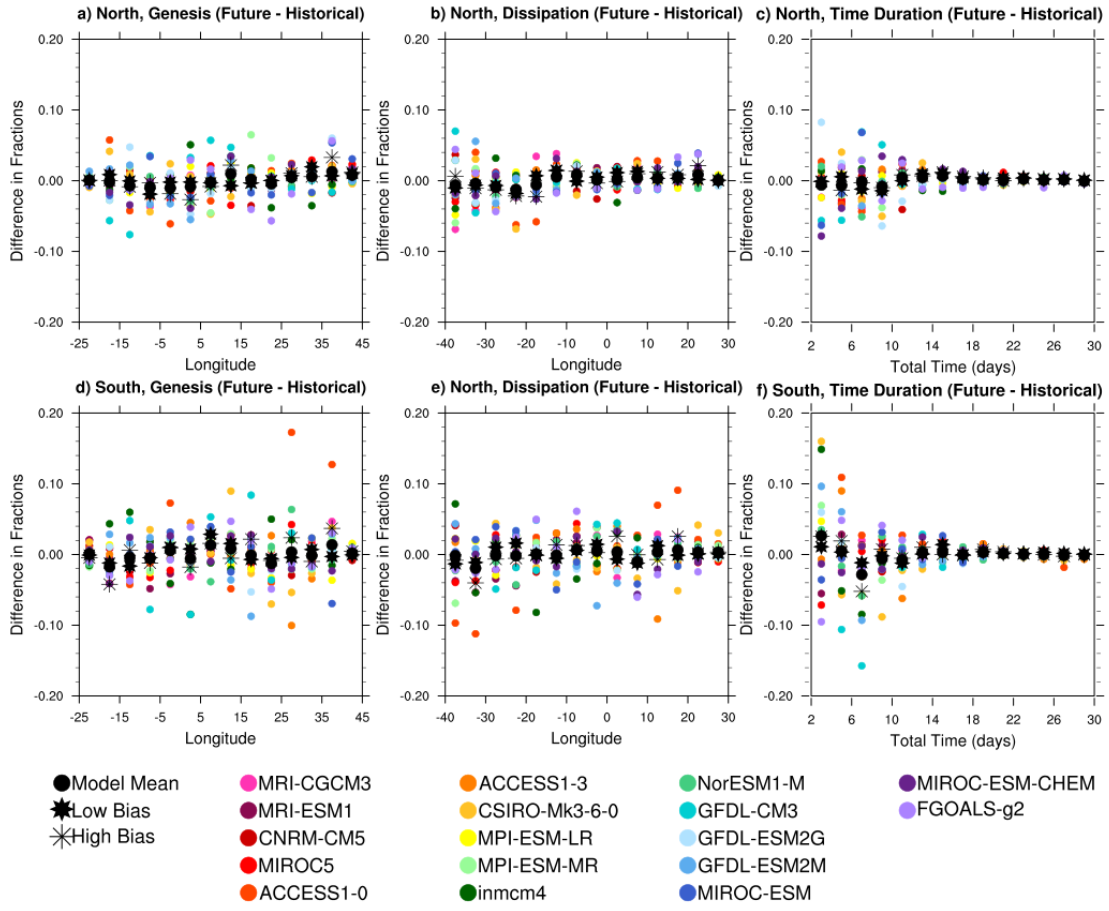



Figure 3.11: Difference in normalized frequencies of AEW genesis (left column; a,d), dissipation (middle column; b,e), and time duration (right column; c,f) in the CMIP5 models in each 5° longitude bin between the historical (1980-2000) and future (2080-2100) periods (future − historical). Black dots representing the overall model mean and stars represent the average of the most/least biased models. Northern track values are displayed in the top row (a,b,c) with southern track values on the bottom (d,e,f). Colors are representative of each CMIP5 model with warm (cool) colors corresponding to finer (coarser) resolution models.

northern track waves, which is also consistent with the results from the other track characteristics presented so far.

Consistent with the similarities in genesis location between the past and future, the distribution of dissipation location retains its structure between both time periods, with the multi-model mean for future projections residing close to zero changes in the dissipation location of northern or southern track AEWs (Fig. 3.11b,e). For each individual longitude bin, the fractional difference in dissipation frequency does not exceed $+/-1.2\%$ in the northern track or $+/-1.9\%$ in the southern track. The low biased models follow similar trends compared to the overall model mean, not exceeding changes of $+/-1.9\%$ and $+/-1.5\%$ in the northern and southern tracks, respectively. There is more variation in the changes within the highly biased models ($+/-2.3\%$ in the northern and $+/-4.1\%$ in the southern), but there is no definite pattern in the location of these changes that indicate a more favored location for dissipation. The variation between the models is also greater in the southern region, ranging from future changes of $-11.2\%$ to $+9.1\%$, whereas the northern region models only span from $-6.8\%$ to $+7.0\%$.

The AEW duration shows small changes when considering the multi-model mean in the future. In every two-day bin of duration for the northern track (Fig. 3.11c), the overall multi-model mean of future differences in AEW lifespan, as well as the low and high biased model means, do not exceed $+/-1.5\%$. The majority of the duration bins of the southern track (Fig. 3.11f) indicate future changes contained within $+/-0.8\%$ ($+/-1.2\%$ for low biased models). However, an overall mean increase of $+2.7\%$ is expected for southern AEWs lasting between 2 and 4 days and a decrease of $-2.8\%$ is projected for AEWs with a 6-8 day lifespan. These changes show a shift in the southern track AEWs towards shorter time durations, which may have consequences in their ability to attain sufficient strength or travel far enough into the Atlantic to trigger Atlantic TCs. However, the changes in

the overall mean time duration could also be attributed to the models containing the highest biases. The mean of the five highest biased models shows an increase of +2.4% for southern AEWs of 2-4 day time span and a decrease of −5.3% for AEWs lasting 6-8 days.

For the changes in each individual model (of both the northern and southern track), the longest lasting AEWs show the smallest changes and the smallest model-to-model variation in the future due to the consistency of nearly zero AEWs lasting longer than 20 days in the past or future periods. The largest fluctuations in future change are associated with AEWs that exist between 2 and 12 days, with the southern track waves showing more disagreement (changes dispersed from −21.2% to +28.8%) between models compared to the northern track waves (changes contained by −7.8% to +8.3%).

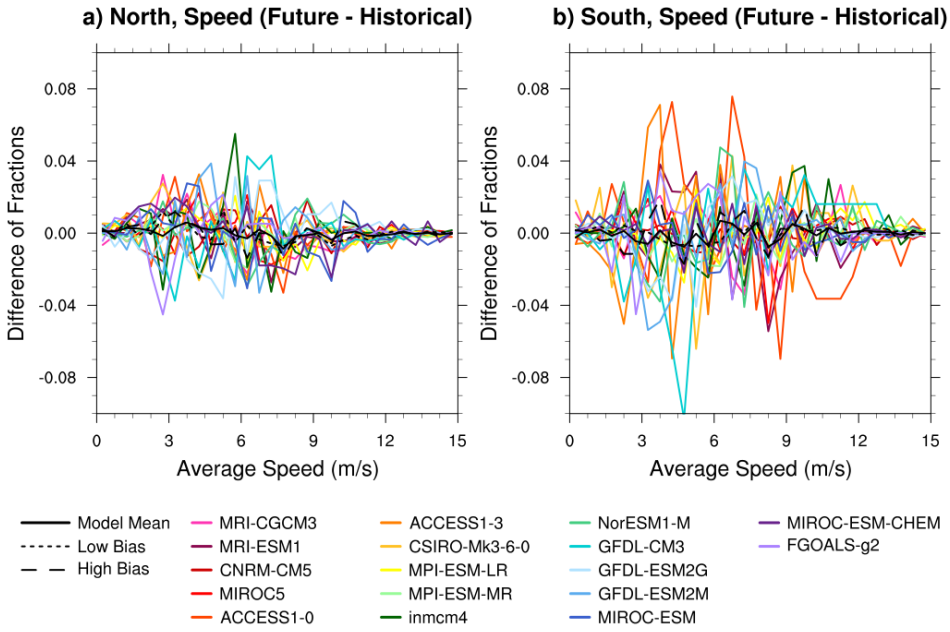



Figure 3.12: Difference in normalized frequencies of AEW speed (future − historical) with the the solid black line representing the overall model mean and the patterned black lines representing the model mean of those with most/least bias. Northern track values are displayed in (a) and southern track values in (b). Colors are representative of each CMIP5 model with warm (cool) colors corresponding to finer (coarser) resolution models.

The differences between the historical and future distributions of the speed of AEWs (Fig. 3.12a) show changes in the positive and negative directions, bounded between $-4.5\%$ and $+5.5\%$, which yields an overall model mean, as well as a low and high biased model mean, with small oscillations around zero (less than $+/-0.9\%$). There is no consistent agreement on which values of average speed will increase or decrease in frequency in the future.

The differences between the frequencies of the historical and future southern track AEW speeds (Fig. 3.12b) in individual models have greater magnitudes (between $-10.3\%$ and $+7.6\%$) than those in the northern track. However, the mean differences also fluctuate around zero (less than $+/-0.8\%$), providing no clear indication of future changes to southern track AEW speeds.

### 3.4.3 Intensity

The changes in CV averaged over each 20 year time period are displayed in Fig. 3.13 (a,c) and Tables 3.3 and 3.4. The northern and southern AEWs show changes that fall close to the grey line representing only small changes between the average CV in the past and future time periods. The overall model mean, as well as the least biased models, show the average CV of the northern track AEWs increases by $0.03\text{x}10^{-5}$ $s^{-1}$ in the future ($+4.74\%$). Twelve of the models support increasing average CV (up $+0.10\text{x}10^{-5}$ $s^{-1}$ in MIROC5), while only three models show a slight decrease ($-0.02\text{x}10^{-5}$ $s^{-1}$) in average intensity. The southern track AEWs possess greater disagreement in the changes of future average intensity. Seven models show future decreases in average CV up to $-0.04\text{x}10^{-5}$ $s^{-1}$, seven models show no change, and two models predict future increases (up to $+0.12\text{x}10^{-5}$ $s^{-1}$ in FGOALS-g2 and $+0.16\text{x}10^{-5}$ $s^{-1}$ in MIROC5). This yields an increase of $+0.01\text{x}10^{-5}$ $s^{-1}$ for the overall model mean ($+1.33\%$) and $+0.03\text{x}10^{-5}$ $s^{-1}$ for the mean of the lowest biased models ($+5.75\%$).

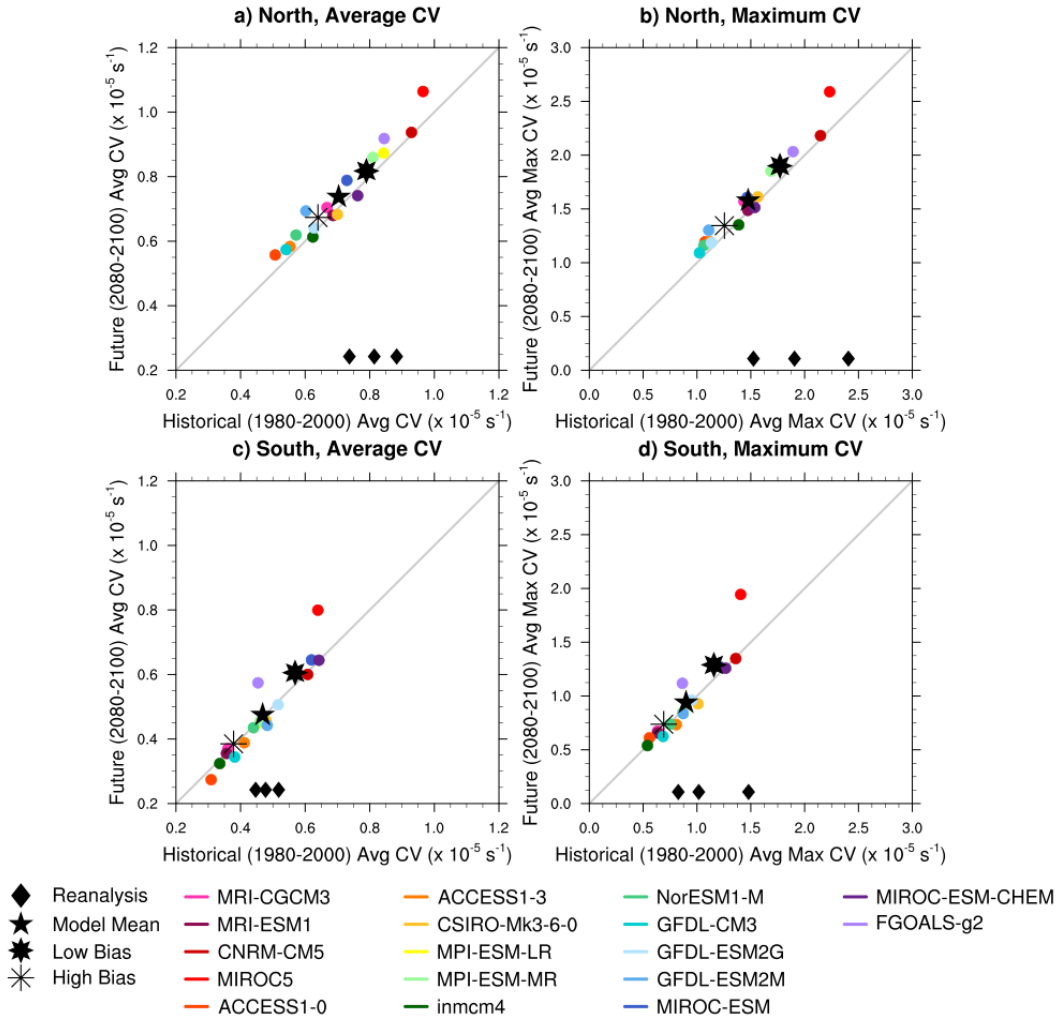



Figure 3.13: Difference in yearly average CV (left column; a,c) and yearly average maximum CV (right column; b,d) between the historical (1980-2000) and future (2080-2100) periods (future − historical) with the grey line representing no change in intensity between the time periods, the black diamonds representing the reanalysis averages, and the stars representing model means. Northern track values are displayed in the top row (a,b) with southern track values on the bottom (c,d). Colors are representative of each CMIP5 model with warm (cool) colors corresponding to finer (coarser) resolution models.

Table 3.3: Average CV (x$10^{-5}$ $s^{-1}$) of northern track AEWs during the historical and future periods for each model along with the raw difference (future − historical) and the percent change.

| **Model** | **Historical** | **Future** | **Raw Change** | **Percent Change** |
|---|---|---|---|---|
| MRI-CGCM3 | 0.67 | 0.70 | +0.04 | +5.48% |
| MRI-ESM1 | 0.69 | 0.68 | −0.01 | −0.89% |
| CNRM-CM5 | 0.93 | 0.94 | +0.01 | +0.87% |
| MIROC5 | 0.96 | 1.06 | +0.10 | +10.27% |
| ACCESS1-0 | 0.51 | 0.56 | +0.05 | +9.88% |
| ACCESS1-3 | 0.55 | 0.58 | +0.03 | +5.49% |
| CSIRO-Mk3-6-0 | 0.70 | 0.68 | −0.02 | −2.45% |
| MPI-ESM-LR | 0.84 | 0.87 | +0.03 | +3.58% |
| MPI-ESM-MR | 0.81 | 0.86 | +0.05 | +6.18% |
| inmcm4 | 0.62 | 0.61 | −0.01 | −1.71% |
| NorESM1-M | 0.57 | 0.62 | +0.05 | +8.27% |
| GFDL-CM3 | 0.54 | 0.57 | +0.03 | +6.07% |
| GFDL-ESM2G | 0.63 | 0.64 | +0.01 | +2.14% |
| GFDL-ESM2M | 0.60 | 0.69 | +0.09 | +15.16% |
| MIROC-ESM | 0.73 | 0.79 | +0.06 | +8.16% |
| MIROC-ESM-CHEM | 0.76 | 0.74 | −0.02 | −2.80% |
| FGOALS-g2 | 0.84 | 0.92 | +0.07 | +8.72% |
| Overall Model Mean | 0.70 | 0.74 | +0.03 | +4.74% |
| Low Biased Mean | 0.79 | 0.81 | +0.02 | +3.05% |
| High Biased Mean | 0.64 | 0.67 | +0.03 | +4.66% |

Table 3.4: As in Table 3.3, but for southern track AEWs.

| **Model** | **Historical** | **Future** | **Raw Change** | **Percent Change** |
|---|---|---|---|---|
| MRI-CGCM3 | 0.36 | 0.37 | +0.01 | +2.60% |
| MRI-ESM1 | 0.36 | 0.36 | 0.00 | −0.27% |
| CNRM-CM5 | 0.61 | 0.60 | −0.01 | −1.24% |
| MIROC5 | 0.64 | 0.80 | +0.16 | +25.05% |
| ACCESS1-0 | 0.31 | 0.27 | −0.03 | −11.26% |
| ACCESS1-3 | 0.41 | 0.39 | −0.02 | −5.56% |
| CSIRO-Mk3-6-0 | 0.48 | 0.46 | −0.02 | −4.56% |
| MPI-ESM-LR | 0.46 | 0.45 | −0.01 | −2.93% |
| MPI-ESM-MR | 0.46 | 0.46 | 0.00 | −1.01% |
| inmcm4 | 0.34 | 0.32 | −0.01 | −3.44% |
| NorESM1-M | 0.44 | 0.44 | 0.00 | −1.10% |
| GFDL-CM3 | 0.38 | 0.34 | −0.04 | −9.90% |
| GFDL-ESM2G | 0.52 | 0.51 | −0.01 | −1.93% |
| GFDL-ESM2M | 0.48 | 0.44 | −0.04 | −8.36% |
| MIROC-ESM | 0.62 | 0.65 | +0.03 | +4.12% |
| MIROC-ESM-CHEM | 0.64 | 0.64 | 0.00 | +0.26% |
| FGOALS-g2 | 0.45 | 0.57 | +0.12 | +26.51% |
| Overall Model Mean | 0.47 | 0.47 | +0.01 | +1.33% |
| Low Biased Mean | 0.57 | 0.60 | +0.03 | +5.75% |
| High Biased Mean | 0.38 | 0.38 | 0.00 | +0.70% |

Table 3.5: Average maximum CV (x$10^{-5}$ $s^{-1}$) of northern track AEWs during the historical and future periods for each model along with the raw difference (future − historical) and the percent change.

| **Model** | **Historical** | **Future** | **Raw Change** | **Percent Change** |
|---|---|---|---|---|
| MRI-CGCM3 | 1.44 | 1.57 | +0.13 | +9.24% |
| MRI-ESM1 | 1.47 | 1.49 | +0.01 | +0.98% |
| CNRM-CM5 | 2.15 | 2.18 | +0.03 | +1.59% |
| MIROC5 | 2.23 | 2.59 | +0.36 | +15.98% |
| ACCESS1-0 | 1.07 | 1.19 | +0.12 | +11.13% |
| ACCESS1-3 | 1.12 | 1.20 | +0.08 | +7.03% |
| CSIRO-Mk3-6-0 | 1.56 | 1.61 | +0.05 | +3.08% |
| MPI-ESM-LR | 1.74 | 1.88 | +0.15 | +8.48% |
| MPI-ESM-MR | 1.69 | 1.85 | +0.16 | +9.72% |
| inmcm4 | 1.39 | 1.35 | −0.04 | −2.60% |
| NorESM1-M | 1.06 | 1.16 | +0.10 | +9.10% |
| GFDL-CM3 | 1.02 | 1.09 | +0.07 | +6.72% |
| GFDL-ESM2G | 1.13 | 1.19 | +0.05 | +4.65% |
| GFDL-ESM2M | 1.11 | 1.30 | +0.19 | +17.35% |
| MIROC-ESM | 1.47 | 1.61 | +0.14 | +9.54% |
| MIROC-ESM-CHEM | 1.54 | 1.51 | −0.02 | −1.57% |
| FGOALS-g2 | 1.89 | 2.03 | +0.14 | +7.42% |
| Overall Model Mean | 1.48 | 1.58 | +0.10 | +6.88% |
| Low Biased Mean | 1.77 | 1.89 | +0.12 | +6.62% |
| High Biased Mean | 1.26 | 1.33 | +0.08 | +6.13% |

Table 3.6: As in Table 3.5, but for southern track AEWs.

| **Model** | **Historical** | **Future** | **Raw Change** | **Percent Change** |
|---|---|---|---|---|
| MRI-CGCM3 | 0.63 | 0.67 | +0.04 | +6.38% |
| MRI-ESM1 | 0.63 | 0.66 | +0.02 | +3.46% |
| CNRM-CM5 | 1.36 | 1.35 | −0.01 | −0.88% |
| MIROC5 | 1.41 | 1.94 | +0.54 | +38.32% |
| ACCESS1-0 | 0.56 | 0.61 | +0.05 | +9.54% |
| ACCESS1-3 | 0.81 | 0.73 | −0.07 | −9.11% |
| CSIRO-Mk3-6-0 | 1.01 | 0.93 | −0.08 | −8.10% |
| MPI-ESM-LR | 0.86 | 0.84 | −0.02 | −2.54% |
| MPI-ESM-MR | 0.87 | 0.85 | −0.02 | −1.79% |
| inmcm4 | 0.54 | 0.54 | 0.00 | −0.19% |
| NorESM1-M | 0.75 | 0.74 | −0.01 | −1.75% |
| GFDL-CM3 | 0.69 | 0.62 | −0.06 | −8.90% |
| GFDL-ESM2G | 0.95 | 0.96 | +0.01 | +0.93% |
| GFDL-ESM2M | 0.87 | 0.84 | −0.03 | −4.01% |
| MIROC-ESM | 1.20 | 1.28 | +0.08 | +6.74% |
| MIROC-ESM-CHEM | 1.27 | 1.26 | −0.01 | −0.64% |
| FGOALS-g2 | 0.86 | 1.12 | +0.25 | +29.36% |
| Overall Model Mean | 0.90 | 0.94 | +0.04 | +4.42% |
| Low Biased Mean | 1.16 | 1.28 | +0.12 | +10.38% |
| High Biased Mean | 0.69 | 0.73 | +0.03 | +4.96% |

Considering the maximum CV (Fig. 3.13b and Table 3.5), the northern track AEWs have an overall mean increase in average maximum CV by $0.10\text{x}10^{-5}$ $s^{-1}$ (+6.88%), with the lowest biased models predicting an increase of $0.12\text{x}10^{-5}$ $s^{-1}$ (+6.62%) and the highest biased models predicting an increase of $0.08\text{x}10^{-5}$ $s^{-1}$ (+6.13%). Only two individual models show future decreases (up to $-0.04\text{x}10^{-5}$ $s^{-1}$) and the other 15 models have increases that peak at $+0.36\text{x}10^{-5}$ $s^{-1}$ within MIROC5. These results support the studies that predict future northern track AEWs with greater intensity (Skinner and Diffenbaugh, 2014; Martin and Thorncroft, 2015). The individual models of the southern track have less agreement in the future trends of average maximum CV (Fig. 3.13d and Table 3.6). Eight models indicate decreases (up to $-0.08\text{x}10^{-5}$ $s^{-1}$), three models show no change, and the remaining six models predict increases extending to $+0.25\text{x}10^{-5}$ $s^{-1}$ in FGOALS-g2 and $+0.54\text{x}10^{-5}$ $s^{-1}$ in MIROC5. This spread amongst the models yields an overall model mean of $+0.04\text{x}10^{-5}$ $s^{-1}$ (+4.42%), but the lowest biased models average $+0.12\text{x}10^{-5}$ $s^{-1}$ (+10.38%) in future average maximum CV. Though the least biased models point to increasing maximum intensity in the future, the disagreement among the complete set of model simulations, along with the comparatively small overall mean increase leaves uncertainty surrounding the future trends in the maximum intensity of southern track AEWs.

The greatest future changes in the average intensity and average maximum intensity for both the northern and southern track AEWs occur within the MIROC5 model. MIROC5 shows increases in AEW intensity when measured by either average CV or average maximum CV (Fig. 3.13). MIROC5 is also the least biased model in representing the northern and southern track AEWs.

In addition to the mean changes in intensity, the changes to the intensity distribution are also examined, as shown in Fig. 3.14. The difference between the future and historical distributions of northern track average CV (Fig. 3.14a) yield

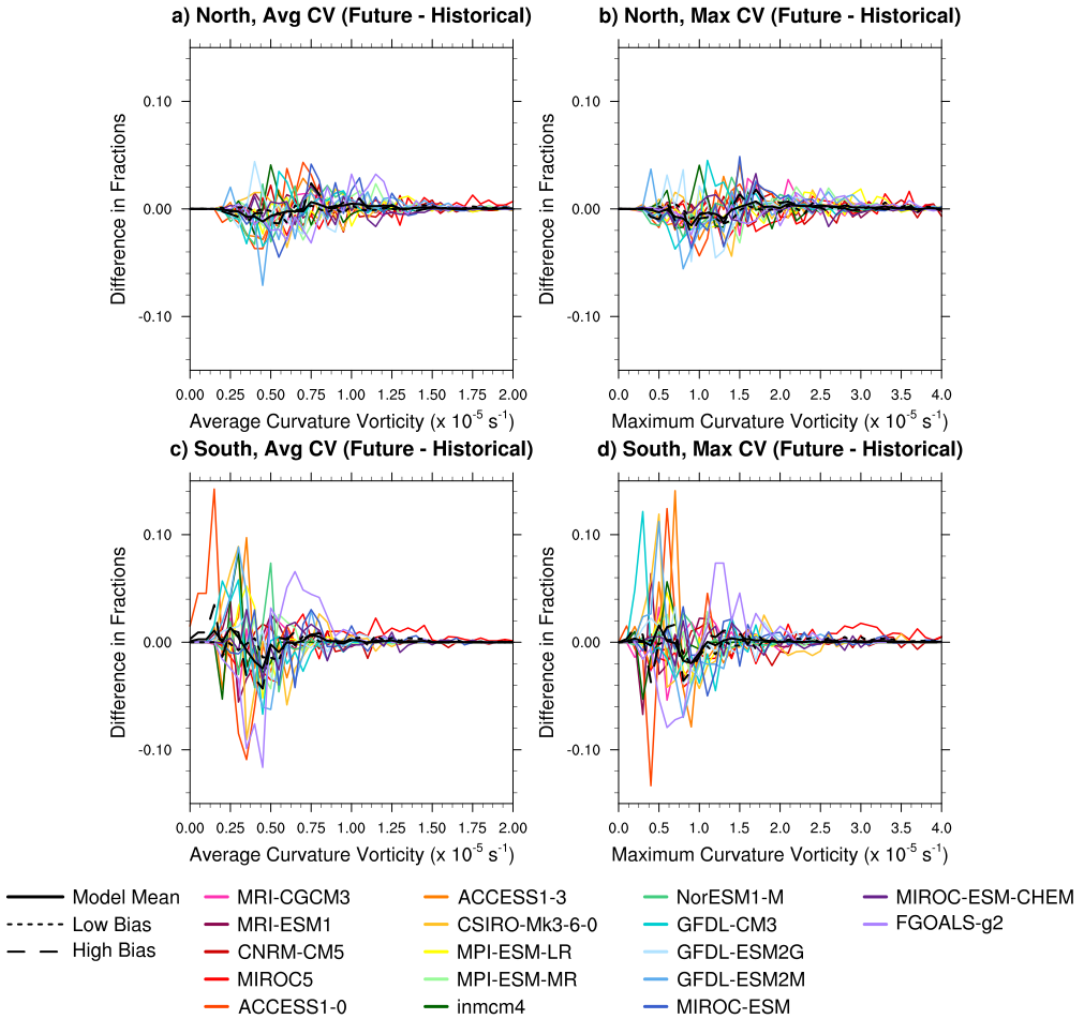



Figure 3.14: Difference in normalized frequency of average CV (left column; a,c) and maximum CV (right column; b,d) between the historical (1980-2000) and future (2080-2100) periods (future − historical). Northern track values are displayed in the top row (a,b) with southern track values on the bottom (c,d). The solid black line represents the overall model mean and the patterned black lines represent the model mean of those with most/least bias. Colors are representative of each CMIP5 model with warm (cool) colors corresponding to finer (coarser) resolution models.

a mean difference close to zero, with some signal of decreases (−1.2%) in the frequency of average CV near 0.5x10$^{-5}$ s$^{-1}$ and increases (+0.6%) near 0.75x10$^{-5}$ s$^{-1}$. These are differences among fractional frequencies; therefore, if there is a decrease in part of the distribution, there must be increases in another. In this case, the slight increases in the larger average CV values indicate that the future AEWs may be somewhat more intense on average, which would agree with results from Skinner and Diffenbaugh (2014) and Martin and Thorncroft (2015). The increase in frequency of AEWs with average CV near 0.75x10$^{-5}$ s$^{-1}$, though, is seen more clearly through the highest biases models (+2.4%) and not exhibited by the lowest biased models (+0.3%).

The projections for the future differ more substantially between individual models in the southern track, as shown by Fig. 3.14c. FGOALS-g2 and ACCESS1-0 show decreases of 11% in AEWs with average CV near 0.40x10$^{-5}$ s$^{-1}$, but FGOALS-g2 projects increases (+6%) near 0.70x10$^{-5}$ s$^{-1}$ (increasing future intensity) and ACCESS1-0 shows the increases (+12%) at lower average CV values of 0.20x10$^{-5}$ s$^{-1}$ (decreasing future intensity). The lack of robust signal from the models results in an overall decrease (−2.4%) in average CV near 0.40x10$^{-5}$ s$^{-1}$, but increases in both more intense and less intense average CV values. Once again, the signals of the future changes are primarily due to the highest biased models which show a 3.5% increase at 0.20x10$^{-5}$ s$^{-1}$ and a 4.3% decrease at 0.40x10$^{-5}$ s$^{-1}$, indicating more waves with decreased average intensity.

Among the individual models, there are some changes in maximum CV between the historical and future simulations of the northern track AEWs (Fig. 3.14b). The overall model mean and the high and low biased model means have a small decrease (−1.5%) in normalized frequency of AEWs with maximum CV between 0.75x10$^{-5}$ s$^{-1}$ and 1.25x10$^{-5}$ s$^{-1}$. This decrease is accompanied by slight increases (+0.7%) in AEWs with a maximum CV around 1.75 x10$^{-5}$ s$^{-1}$. Though these signals are

small, they support the hypotheses by Skinner and Diffenbaugh (2014) that the maximum intensity of northern track AEWs will increase in the future.

For the southern track (Fig. 3.14d), some models (FGOALS-g2, ACCESS1-0, inmcm4, MRI-ESM1) indicate future increases in maximum AEW strength and others (ACCESS1-3, GFDL-CM3, GFDL-ESM2M, CSIRO-Mk3-6-0) project decreases. While extreme changes in one direction from certain models are negated by extreme changes in the opposite direction from other models, the model mean projects a decrease ($-2.0\%$) in maximum CV near $0.75\text{x}10^{-5}$ $s^{-1}$ and an increase ($+1.5\%$) at $0.50\text{x}10^{-5}$ $s^{-1}$, which is also supported by the means of the high and low biased models. These changes yield future waves in the southern regions that have weaker average maximum intensity than those in the historical period.

# Chapter 4

# Summary and Conclusions

Previous studies have used EKE (Martin and Thorncroft, 2015) or spectral analysis of meridional wind (Skinner and Diffenbaugh, 2013) to detect future changes in AEW activity. However, this study has utilized an objective tracking technique to trace AEWs in reanalyses and CMIP5 models within a historical (1980-2000) and a future (2080-2100) analysis period for the first time. Establishing historical biases and comparing the changes in AEW track characteristics reveals the extent to which AEWs will change in the future. A more detailed understanding of future projections of AEWs can give insight into trends in future Sahel rainfall and downstream TC genesis.

Overall, the CMIP5 models posses the smallest historical biases in their distributions of monthly normalized AEW frequency and average AEW duration compared to the mean of the reanalyses in both the northern and southern regions. The highest model biases of the northern region arise from the inability of the models to detect the favored dissipation region on the continental side of the coast and the secondary peak in genesis just offshore which are both features within the reanalyses. The largest model biases of the southern track are attributed to the skewness of AEW lifetime. The reanalysis mean has a greater skewness value indicating more AEWs in the reanalyses that exist for the longest lifetimes compared to those of the models. The historical biases between the models and the

reanalyses are most likely due to differences in resolution and parameterizations, including convection, microphysics, carbon, vegetation, and planetary boundary layer.

The least biased models in simulating northern track AEWs are MIROC5, MIROC4h, MRI-ESM1, MRI-CGCM3, CSIRO-Mk3-6-0, and CNRM-CM5, while the most biased models are ACCESS1-0, NorESM1-M, MIROC-ESM-CHEM, GFDL-ESM2G, and MIROC-ESM. The separation between small and large biases in the northern track aligns well with the differences in model grid spacing. The least biased models are those with the finest grid spacings and the most biased models are correlated with coarse grid spacing. For the southern track AEWs, the models that simulate AEWs with the smallest total error are MIROC5, MPI-ESM-MR, MPI-ESM-P, CRNM-CM5, GFDL-ESM2G, and MIROC-ESM and the models containing the highest overall bias compared to the reanalyses mean are ACCESS1-0, ACCESS1-3, inmcm4, FGOALS-g2, MIROC4h, and GFDL-CM3. The separation between most and least bias in the southern track AEWs is not distinctly linked to resolution, as the least biased models fall in the mid-range of grid spacing and the most biased models contain both the finest- (MIROC4h) and coarsest- (FGOALS-g2) resolution models. This could be because the accuracy of the convective parameterizations is essential in the model representations of the southern track AEWs, making the model resolutions appear to be less important. However, in the northern track, as the AEWs are drier with weaker convection, the simulated convection is less important in determining the most/least biased models, making the model resolution appear to be the driving factor in decreasing biases. It is interesting to note that in both the northern and southern regions, MIROC5 is the least biased model and ACCESS1-0 is the most biased model. CNRM-CM5 is also one of the least biased models in both regions. MIROC4h is

one of the least biased models in the northern track, but one of the most biased models in the southern track, and vice versa for GFDL-ESM2G.

An additional direction for this study includes the use of statistical bias corrections to account for the model biases compared to the reanalyses. Eliminating the biases related to the parameterizations of the models within the historical period could perhaps decrease some of the discrepancies among the set of models and result in more clear future trends, especially for the southern track.

It must be mentioned that this study relies on the average of three reanalyses (CFSR, ERA-Interim, JRA-55) to portray the reality of the historical period. However, there are inconsistencies among the reanalyses. Within the CMIP5 models, historical biases in the frequency or intensity of resolved AEWs compared to the reanalysis mean could be attributed to the differing resolutions of the models, but there are also discrepancies in the year-to-year variability between the three reanalyses (see Figs. 3.3(a,c) and 3.7). For example, in 1999 there is a local maxima in average yearly frequency within ERA-Interim and JRA-55, but CFSR is showing a local minima (Fig. 3.3a). In 1997, there is a local minima in average maximum CV within CFSR (Fig. 3.7b), where a local maxima occurs for ERA-Interim. The yearly variabilities in the reanalyses generally align more closely on the basis of intensity compared to frequency. These differences in yearly variability among the reanalyses contribute to the limitations involved in using a reanalysis average to determine model biases. Improvements could result from the inclusion of additional reanalysis or observational datasets.

These historical biases could be better understood through the evaluation of other variables. Surface temperature and outgoing longwave radiation could provide insight into the ability of the models to simulate spatial temperature gradients and the amount/intensity of convection which impacts the genesis and intensity of AEWs. Differences in the reanalyses and the historical simulations regarding

precipitation would be useful in detecting moisture biases and biases in the position and extent of the West African Monsoon which may affect the frequency of AEWs.

Further information regarding the root of the biases could be revealed by a comparison of the reanalyses to the historical AMIP (atmosphere only) simulations. Richter and Xie (2008) show that the CMIP5 models have difficulties detecting the cold tongue of the Gulf of Guinea which may affect the latitudinal temperature gradient, the AEJ strength, or the ability of AEWs to propagate into the main development region for Atlantic TCs. Investigating the track characteristics of AEWs within AMIP simulations may help determine if the sea surface temperatures are responsible for the northern track AEW dissipation just off the West African coast or the lack of southern track AEWs reaching 35°W. The use of observed sea surface temperature forcings within the AMIP models could also provide information regarding the role of the land-sea temperature contrast in the changing frequency and intensity of AEWs.

Results from prior studies (e.g. Martin and Thorncroft, 2015) indicate more robust changes in the northern track AEWs, including decreases in the total frequency of AEWs, but increases in the frequency of the strongest AEWs, and a more distinct seasonal cycle. The southern track AEWs, however, show larger variations among the models yielding no specific conclusions regarding future changes.

The total frequency of AEW tracks resolved within the objective tracking algorithm shows a lack of agreement regarding changes in the southern track AEWs but shows an increase of 1.5 waves per year, on average, in the northern track in the future period. The monthly distribution of AEW frequency is roughly constant between the past and future time periods for the northern AEWs. Contrastingly, the southern track AEWs indicate a subtle shift in the frequency distribution towards the later months. This trend is supported by Martin and Thorncroft (2015)

who documented a 10% reduction in AEW activity using EKE during the early summer months. Especially since the southern track AEWs are often precursors for Atlantic TCs, a shift in the seasonal cycle could result in a later beginning or later end to the typical TC season.

The average and maximum CV of the northern track AEWs indicate increases in the frequency of the more intense waves, consistent with studies by Skinner and Diffenbaugh (2014) and Martin and Thorncroft (2015). The intensity changes of the southern track AEWs, though, show a lack of a robust agreement, as also discovered by Skinner and Diffenbaugh (2014). The changes in southern track average CV indicate very little change to average AEW intensity; whereas, the changes in average maximum CV show a shift towards slightly weaker AEWs in the future. Weaker southern track AEWs in the future could impact Atlantic TC genesis, since the low-level intensity of the AEW has been linked to the tendency of the AEW to develop into a TC (Thorncroft and Hodges, 2001). The southern track AEWs, however, have their peak amplitudes near 700 hPa, which was not analyzed in this study. To gain a more complete understanding of the intensity changes of southern track AEWs, the methods of this study should be extended to include an analysis of AEWs at 700 hPa.

The future projections in AEW genesis and dissipation locations, as well as the total AEW durations, show consistency between the historical and future periods for both northern and southern track AEWs. This result is expected since many AEWs are triggered by convection and rising motion due to Africa's topography which will remain unchanged in the future, but it suggests that the presence of intense convection in these genesis regions also maintains consistency in the future. Typically a greater percentage of the southern track AEWs have been found to reach the main development region for TCs in the Atlantic (Hopsch et al., 2010). It is curious to note that this study produces a greater percentage of northern

track AEWs reaching the furtherest west longitude bin and also having a greater frequency of the longest duration waves (measured by either net longitude or total time). This contradiction could be a result of the exclusion of the 700 hPa level from this study or the inability of the models to simulate two distinct AEW tracks.

The separation between northern and southern AEW regions in this study was forced by specifying the latitude band (either north or south of the AEJ) to be used within the tracking algorithm. While this study identifies AEWs that exist on the north and south sides of the AEJ at low levels, the objective tracking method can only provide the longitude coordinates of the tracks. For example, whether the northern AEWs lie 2° or 10° north of the AEJ is not reported. Through the use of this tracking technique, it remains a possibility that the northern and southern AEWs are located close enough to the AEJ, hence close enough to each other, that they appear to be merged into one main track over the African continent. It has not yet been established whether the CMIP5 models can resolve two distinctly separate AEW tracks or whether they are merged together. This question would be answered through the use of a 3D tracking technique.

A 3D, "automatic" tracking method called TRACK has been used in previous studies (Thorncroft and Hodges, 2001; Hodges et al., 2003; Hopsch et al., 2007). TRACK identifies local maxima in relative or curvature vorticity and creates latitude/longitude tracks of AEWs (Thorncroft and Hodges, 2001). The TRACK algorithm initially identifies AEWs as closed contour maxima in the vorticity field and will trace the AEWs by minimizing their "cost function" of the motion, while also confining the greatest displacement distance permitted in a single time step. The TRACK algorithm has shown promise when the resulting tracks are compared to those from the best track data from the National Hurricane Center. This tracking method is beneficial because it provides both the latitudinal and longitudinal locations of the AEWs, rather than just the longitude location in a given latitude

band as done in the objective tracking algorithm used in this study. This enables a clearer view of whether the AEW resides on the northern or southern side of the AEJ and if the model even resolves separate storm tracks over the continent or if they are merged together, which would affect TC genesis within the models.

It is important to note that this study shifts the location of the northern and southern regions depending on the shift in the mean summertime AEJ latitude location in the future. While the reported changes still provide insight into the future changes of AEWs north and south of the AEJ, they do not uncover future changes within a constant latitude band. Perhaps the north/south latitudinal shifts of the AEWs yield the greatest future changes which are overlooked when the northern and southern regions are shifted with the AEJ.

A consistent theme throughout the future projections of each characteristic in this study is the uniformity of the models in the northern region and the disagreement between the models in the southern region. This pattern is also cited as a result of Skinner and Diffenbaugh (2014) and Martin and Thorncroft (2015) and has not been alleviated by tracking individual waves, making it hard to deduce trends of the southern track AEWs. With the southern track located near the inter-tropical convergence zone, these AEWs are more often associated with increased convection and moisture which remains a struggle for the models to resolve accurately.

# Bibliography


Adachi, Y., et al., 2013: Basic performance of a new earth system model of the meteorological research institute (MRI-ESM1). *Papers in Meteorology and Geophysics*, **64**, 1–19.

Bain, C. L., K. D. Williams, S. F. Milton, and J. T. Heming, 2014: Objective tracking of African easterly waves in Met Office models. *Quarterly Journal of the Royal Meteorological Society*, **140**, 47–57.

Bentsen, M., et al., 2013: The Norwegian earth system model, NorESM1-M—part 1: Description and basic evaluation of the physical climate. *Geoscientific Model Development*, **6**, 687–720.

Berry, G. J. and C. Thorncroft, 2005: Case study of an intense African easterly wave. *Monthly Weather Review*, **133**, 752–766.

Bi, D., et al., 2013: The ACCESS coupled model: description, control climate and evaluation. *Australian Meteorological and Oceanographic Journal*, **63**, 41–64.

Brammer, A. and C. D. Thorncroft, 2015: Variability and evolution of African easterly wave structures and their relationship with tropical cyclogenesis over the Eastern Atlantic. *Monthly Weather Review*, **143 (12)**, 4975–4995.

Burpee, R. W., 1972: The origin and structure of easterly waves in the lower troposphere of North Africa. *Journal of the Atmospheric Sciences*, **29**, 77–90.

Burpee, R. W., 1974: Characteristics of North African easterly waves during the summers of 1968 and 1969. *Journal of the Atmospheric Sciences*, **31**, 1556–1570.

Camargo, S. J., 2013: Global and regional aspects of tropical cyclone activity in the CMIP5 models. *Journal of Climate*, **26**, 9880–9902.

Carlson, T. N., 1969: Some remarks on African disturbances and their progress over the tropical Atlantic. *Monthly Weather Review*, **97**, 716–726.

Chen, T.-C., S.-Y. Wang, and A. J. Clark, 2008: North Atlantic hurricanes contributed by African easterly waves north and south of the African easterly jet. *Journal of Climate*, **21**, 6767–6776.

Cook, K. H., 1999: Generation of the African easterly jet and its role in determining west African precipitation. *Journal of Climate*, **12**, 1165–1184.

Diaconescu, E. P., P. Gachon, J. Scinocca, and R. Laprise, 2015: Evaluation of daily precipitation statistics and monsoon onset/retreat over Western Sahel in multiple data sets. *Climate Dynamics*, **45**, 1325–1354.

Diedhiou, A., S. Janicot, A. Viltard, and P. de Felice, 1998: Evidence of two regimes of easterly waves over West Africa and the tropical atlantic. *Geophysical Research Letters*, **25 (15)**, 2805–2808.

Donner, L. J., et al., 2011: The dynamical core, physical parameterizations, and basic simulation characteristics of the atmospheric component AM3 of the GFDL global coupled model CM3. *Journal of Climate*, **24**, 3484–3519.

Dunne, J. P., et al., 2012: GFDL's ESM2 global coupled climate–carbon earth system models. part I: Physical formulation and baseline simulation characteristics. *Journal of Climate*, **25**, 6646–6665.

Dwyer, J. G., S. J. Camargo, A. H. Sobel, M. Biasutti, K. A. Emanuel, G. A. Vecchi, M. Zhao, and M. K. Tippett, 2015: Projected twenty-first-century changes in the length of the tropical cyclone season. *Journal of Climate*, **28**, 6181–6192.

Emanuel, K. A., 2013: Downscaling CMIP5 climate models shows increased downscaling CMIP5 climate models shows increased tropical cyclone activity over the 21st century. *Proceedings of the National Academy of Sciences*, **110**, 12 219–12 224.

Fink, A. H. and A. Reiner, 2003: Spatiotemporal variability of the relation between African easterly waves and west African squall lines in 1998 and 1999. *Journal of Geophysical Research*, **108**, 4332–4348.

Giorgetta, M. A., et al., 2013: Climate and carbon cycle changes from 1850 to 2100 in MPI-ESM simulations for the coupled model intercomparison project phase 5. *Journal of Advances in Modeling Earth Systems*, **5**, 572–597.

Grist, J. P., 2002: Easterly waves over Africa. part I: The seasonal cycle and contrasts between wet and dry years. *Monthly Weather Review*, 198–211.

Hagos, S. M. and K. H. Cook, 2008: Ocean warming and late-twentieth-century Sahel drought and recovery. *Journal of Climate*, **212**, 3797–3814.

Hall, N. M. J., G. N. Kiladis, and C. D. Thorncroft, 2006: Three-dimensional structure and dynamics of African easterly waves. part II: Dynamical modes. *Journal of the Atmospheric Sciences*, **63**, 2231–2245.

Hodges, K. I., B. J. Hoskins, J. Boyle, and C. Thorncroft, 2003: A comparison of recent reanalysis datasets using objective feature tracking: Storm tracks and tropical easterly waves. *Monthly Weather Review*, **131**, 2012–2037.

Hopsch, S. B., C. D. Thorncroft, K. Hodges, and A. Aiyyer, 2007: West African storm tracks and their relationship to Atlantic tropical cyclones. *Journal of Climate*, **20**, 2468–2483.

Hopsch, S. B., C. D. Thorncroft, and K. R. Tyle, 2010: Analysis of African easterly wave structures and their role in influencing tropical cyclogenesis. *Monthly Weather Review*, **138**, 1399–1419.

Kiladis, G. N., C. D. Thorncroft, and N. M. J. Hall, 2006: Three-dimensional structure and dynamics of African easterly waves. part I: Observations. *Journal of the Atmospheric Sciences*, **63**, 2212–2230.

Knapp, K. R., M. C. Kruk, D. H. Levinson, H. J. Diamond, and C. J. Neumann, 2010: The international best track archive for climate stewardship (IBTrACS). *Bulletin of the American Meteorological Society*, **91**, 363–376.

Kobayshi, S., et al., 2015: The JRA-55 reanalysis: General specifications and basic characteristics. *J. Meteor. Soc. Japan*, **93**, 5–48.

Landsea, C. W., 1993: A climatology of intense (or major) Atlantic hurricanes. *Monthly Weather Review*, 1703–1713.

Landsea, C. W. and W. M. Gray, 1992: The strong association between Western Sahelian monsoon rainfall and intense Atlantic hurricanes. *Journal of Climate*, **5**, 435–453.

Martin, E. R. and C. Thorncroft, 2015: Representation of African easterly waves in CMIP5 models. *Journal of Climate*, **28**, 7702–7715.

Mathon, V., H. Laurent, and T. Lebel, 2002: Mesoscale convective system rainfall in the Sahel. *Journal of Applied Meteorology*, **41**, 1081–1092.

McCrary, R. R., D. A. Randall, and C. Stan, 2014a: Simulations of the West African monsoon with a superparameterized climate model. part I: The seasonal cycle. *Journal of Climate*, **27**, 8303–8322.

McCrary, R. R., D. A. Randall, and C. Stan, 2014b: Simulations of the West African monsoon with a superparameterized climate model. part II: African easterly waves. *Journal of Climate*, **27**, 8323–8341.

Mekonnen, A., C. D. Thorncroft, and A. Aiyyer, 2006: Analysis of convection and its association with African easterly waves. *Journal of Climate*, **19**, 5405–5421.

National Geophysical Data Center, 2006: 2-minute gridded global relief data (ETOPO2) v2. *National Geophysical Data Center, NOAA*.

Pasch, R. J. and L. A. Avila, 1994: Atlantic tropical systems of 1992. *Monthly Weather Review*, **122**, 539–548.

Rappaport, E. N., 2014: Fatalities in the united states from atlantic tropical cyclones: New data and interpretation. *Bulletin of the American Meteorological Society*, **95**, 341–346.

Reed, R. J., D. C. Norquist, and E. E. Recker, 1977: The structure and properties of African wave disturbances as observed during phase III of GATE. *Monthly Weather Review*, 317–333.

Richter, I. and S.-P. Xie, 2008: On the origin of equatorial Atlantic biases in coupled general circulation models. *Climate Dynamics*, **31**, 587–598.

Rotstayn, L., M. Collier, Y. Feng, H. Gordon, S. O'Farrell, I. Smith, and J. Syktus, 2010: Improved simulation of Australian climate and ENSO-related rainfall variability in a GCM with an interactive aerosol treatment. *International Journal of Climatology*, **30**, 1067–1088.

Ruti, P. M. and A. Dell'Aquila, 2010: The twentieth century African easterly waves in reanalysis systems and IPCC simulations, from intra-seasonal to inter-annual variability. *Climate Dynamics*, **35**, 1099–1117.

Saha, S., et al., 2010: The NCEP climate forecast system reanalysis. *Bull. Amer. Meteor. Soc.*, **91**, 1015–1057.

Simmons, A., S. Uppala, D. Dee, and S. Kobayashi, 2007: Era-Interim: New ECMWF reanalysis products from 1989 onwards. *ECMWF Newsletter*, **110**, 25–35.

Skinner, C. B. and N. S. Diffenbaugh, 2013: The contribution of African easterly waves to monsoon precipitation in the CMIP3 ensemble. *Journal of Geophysical Research: Atmospheres*, **118**, 3590–3609.

Skinner, C. B. and N. S. Diffenbaugh, 2014: Projected changes in African easterly wave intensity and track in response to greenhouse forcing. *Proceedings of the National Academy of Sciences of the United States of America*, **111 (19)**, 6882–6887.

Taylor, K. E., R. J. Stouffer, and G. A. Meehl, 2012: An overview of CMIP5 and the experiment design. *Bulletin of the American Meteorology Society*, **93**, 485–498.

Thorncroft, C. and K. Hodges, 2001: African easterly wave variability and its relationship to Atlantic tropical cyclone activity. *Journal of Climate*, **14**, 1166–1179.

Thorncroft, C. D., N. M. J. Hall, and G. N. Kiladis, 2008: Three-dimensional structure and dynamics of African easterly waves. part III: Genesis. *Journal of the Atmospheric Sciences*, **65**, 3596–3607.

Vellinga, M., M. Roberts, P. L. Vidale, M. S. Mizielinski, M.-E. Demory, R. Schiemann, J. Strachan, and C. Bain, 2016: Sahel decadal rainfall variability and the role of model horizontal resolution. *Geophysical Research Letters*, **43 (1)**, 326–333.

Ventrice, M. J., C. D. Thorncroft, and M. A. Janiga, 2012: Atlantic tropical cyclogenesis: A three-way interaction between an African easterly wave, diurnally varying convection, and a convectively coupled atmospheric kelvin wave. *Monthly Weather Review*, 1108–1124.

Voldoire, A., et al., 2013: The CNRM-CM5.1 global climate model: description and basic evaluation. *Climate Dynamics*, **40**, 2091–2121.

Volodin, E., N. Dianskii, and A. Gusev, 2010: Simulating present-day climate with the INMCM4.0 coupled model of the atmospheric and oceanic general circulations. *Izvestiya, Atmospheric and Oceanic Physics*, **46**, 414–431.

Wang, S.-Y. and R. R. Gillies, 2011: Observed change in sahel rainfall, circulations, african easterly waves, and atlantic hurricanes since 1979. *International Journal of Geophysics*, **2011**, Article ID 259 529.

Watanabe, M., et al., 2010: Improved climate simulation by MIROC5: Mean states, variability, and climate sensitivity. *Journal of Climate*, **23**, 6312–6335.

You, Q., J. Min, W. Zhang, N. Pepin, and S. Kang, 2015: Comparison of multiple datasets with gridded precipitation observations over the Tibetan Plateau. *Climate Dynamics*, **45**, 791–806.

Yukimoto, S., et al., 2012: A new global climate model of the meteorological research institute: MRI-CGCM3—model description and basic performance. *Journal of the Meteorological Society of Japan*, **90A**, 23–64.

Zhou, T., F. Song, and X. Chen, 2013: Historical evolution of global and regional surface air temperature simulated by FGOALS-s2 and FGOALS-g2: How reliable are the model results? *Advances in Atmospheric Sciences*, **30**, 638–657.

# Appendices

# Appendix A

# Sensitivity Tests for Objective Tracking Algorithm

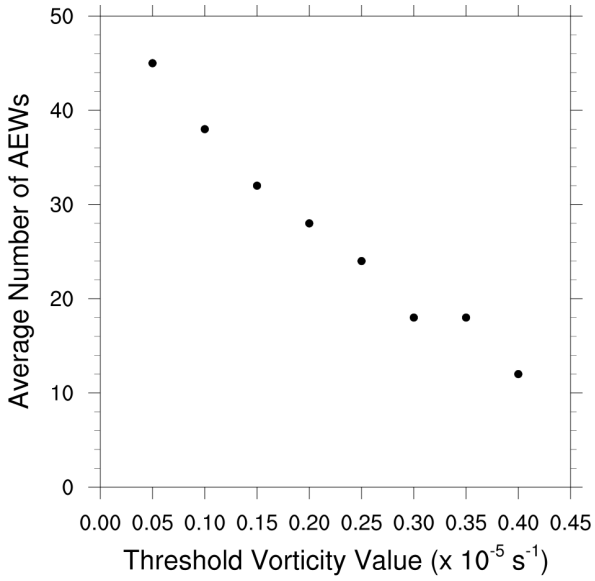



Figure A.1: Sensitivity test to determine the threshold CV that yields 30-40 AEWs per season (May-October) (Thorncroft and Hodges, 2001; Fink and Reiner, 2003; Hopsch et al., 2010; Bain et al., 2014) between 1980 and 2000 within JRA-55 reanalysis.

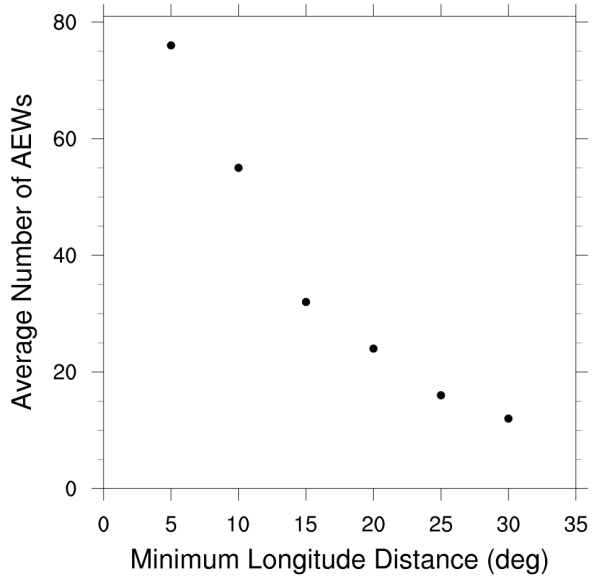



Figure A.2: Sensitivity test to determine the setting of minimum longitude distance that yields 30-40 AEWs per season (May-October) (Thorncroft and Hodges, 2001; Fink and Reiner, 2003; Hopsch et al., 2010; Bain et al., 2014) between 1980 and 2000 within JRA-55 reanalysis.

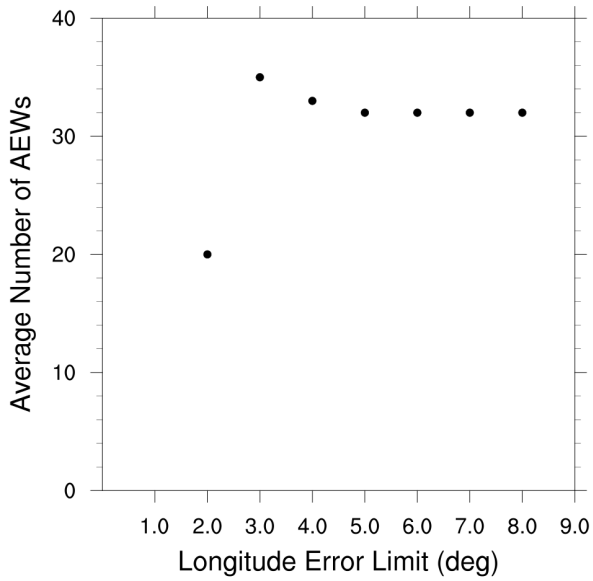



Figure A.3: Sensitivity test to determine the longitude error limit that yields 30-40 AEWs per season (May-October) (Thorncroft and Hodges, 2001; Fink and Reiner, 2003; Hopsch et al., 2010; Bain et al., 2014) between 1980 and 2000 within JRA-55 reanalysis.

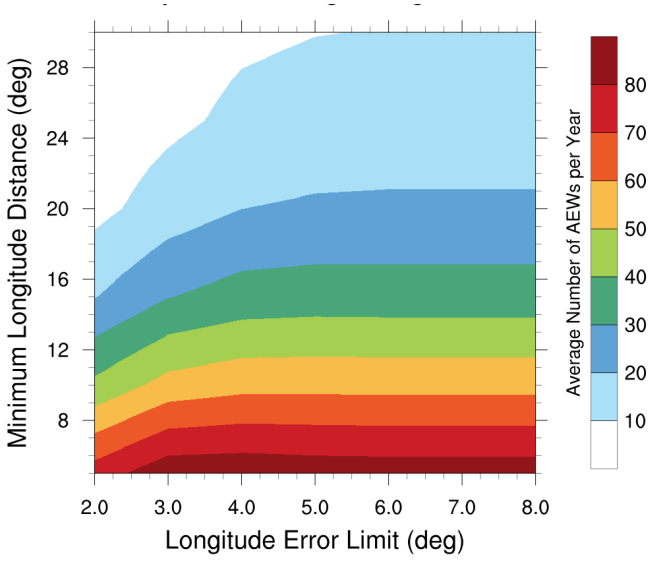



Figure A.4: Sensitivity test to determine the combination of minimum longitude distance and longitude error limit that yield 30-40 AEWs per season (May-October) (Thorncroft and Hodges, 2001; Fink and Reiner, 2003; Hopsch et al., 2010; Bain et al., 2014) between 1980 and 2000 within JRA-55 reanalysis.

# Appendix B

## Net Longitude Distance

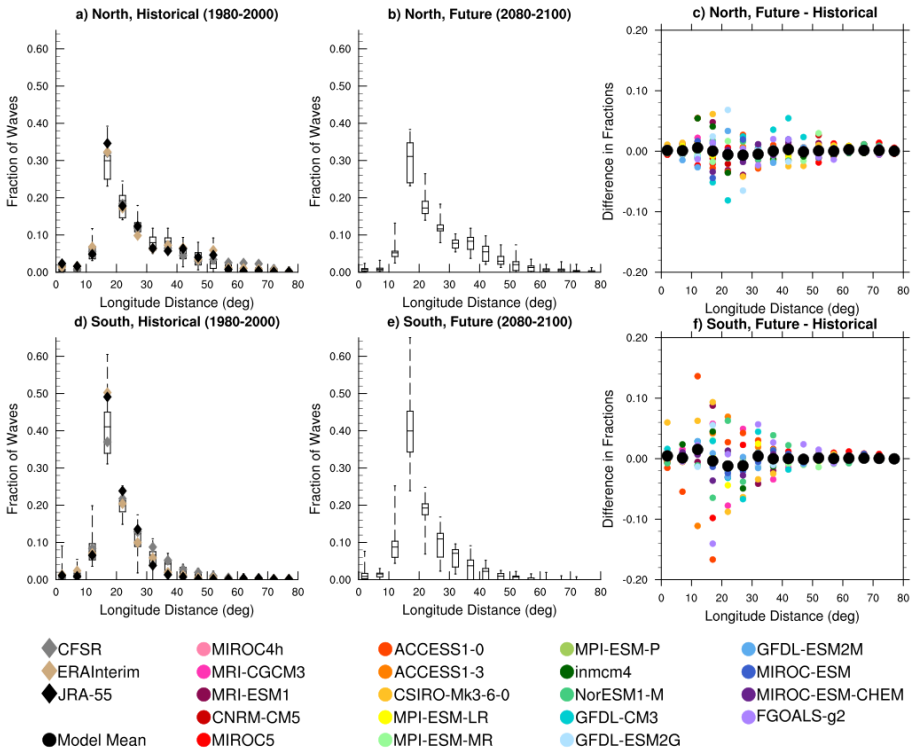



Figure B.1: Box plots (a,b,d,e) of the frequency of AEW net longitude in each 5° longitude bin, normalized by the total number of AEWs resolved by each model individually during the historical period (left) and future period (middle). The difference in normalized frequencies (future − past) is shown on the right (c,f). Northern track values are displayed in the top row with southern track values on the bottom. Diamond markers (a,d) represent each reanalysis. Colored dots (c,f) are representative of each CMIP5 model with warm (cool) colors corresponding to finer (coarser) resolution models.

# Appendix C

# Monthly Distribution of Average CV

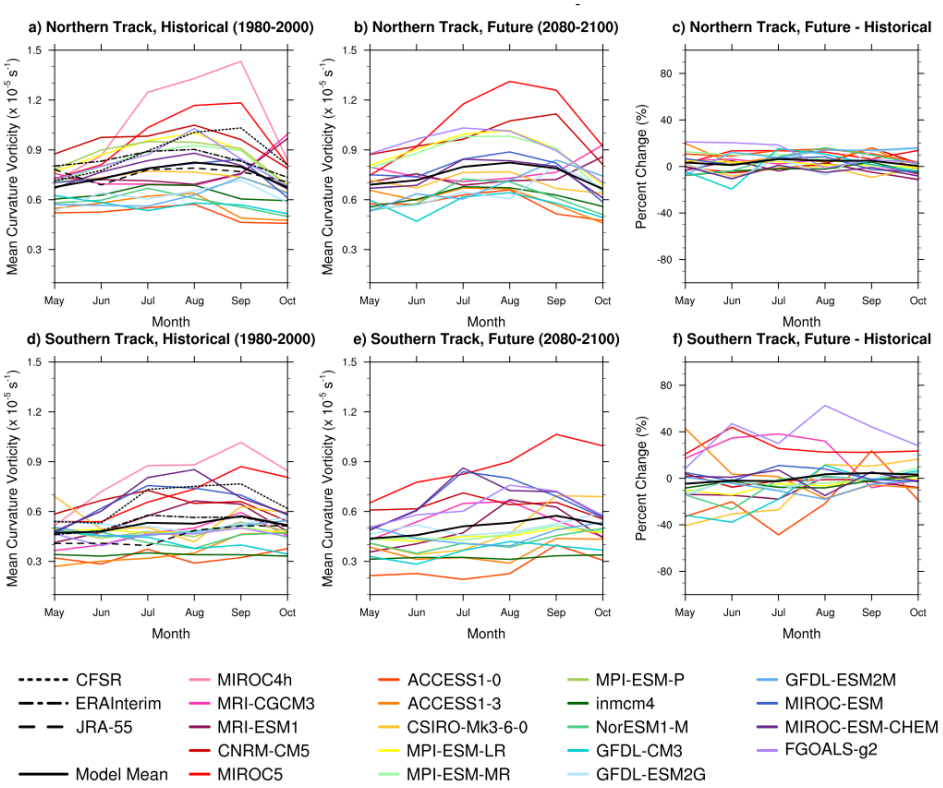



Figure C.1: Average CV of AEWs resolved each month during the historical period (left) and future period (middle). The percent change from the past to the future is shown on the right. Northern track values are displayed in the top row with southern track values on the bottom. Patterned black lines represent each reanalysis. Solid black line is the model mean. Colors are representative of each CMIP5 model with warm (cool) colors corresponding to finer (coarser) resolution models.

# Appendix D

# Distribution of Future AEW Characteristics

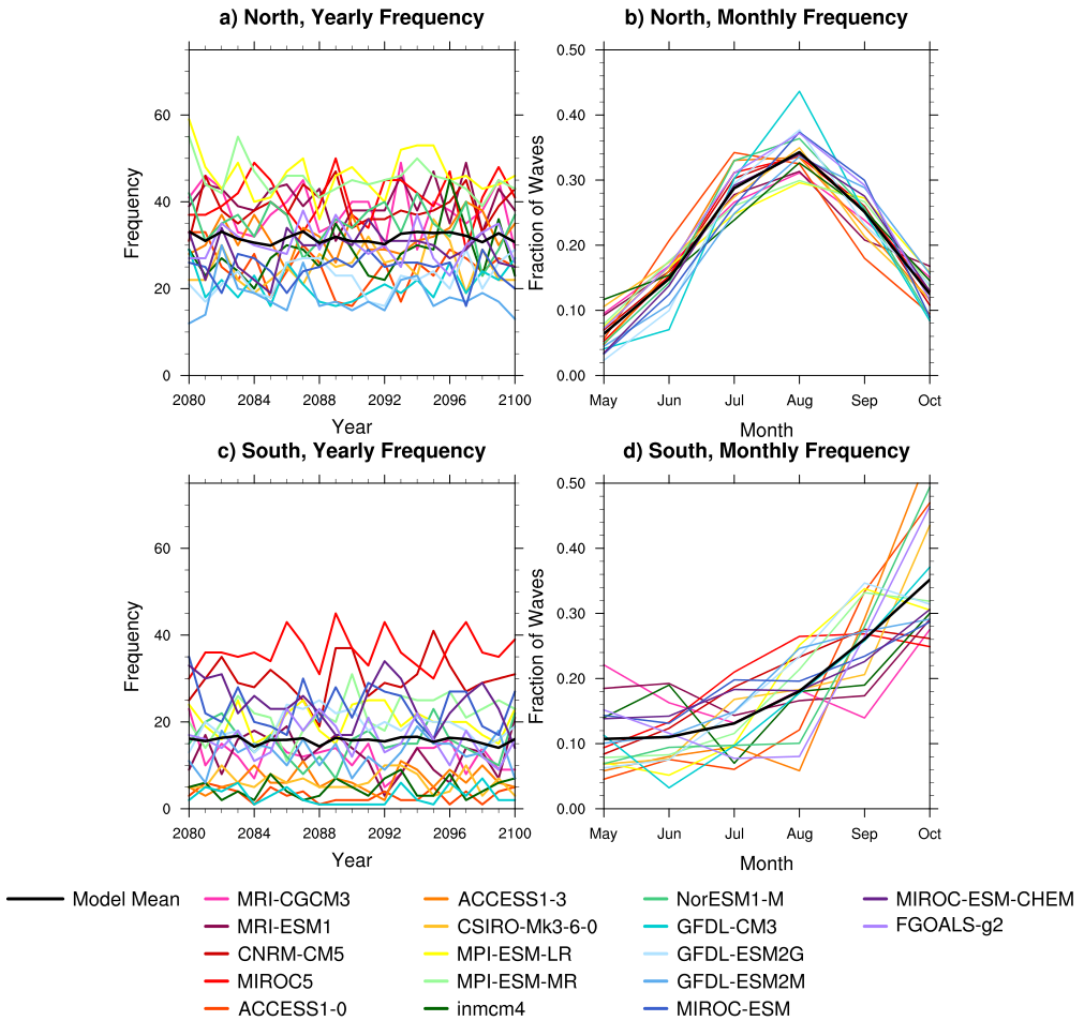



Figure D.1: Yearly frequency of AEWs (left column; a,c) and monthly frequency normalized by the total number of AEWs resolved by each model individually (right column; b,d) during the future period (2080-2100). Northern track values are displayed in the top row (a,b) with southern track values on the bottom (c,d). Solid black line is the model mean. Colors are representative of each CMIP5 model with warm (cool) colors corresponding to finer (coarser) resolution models.

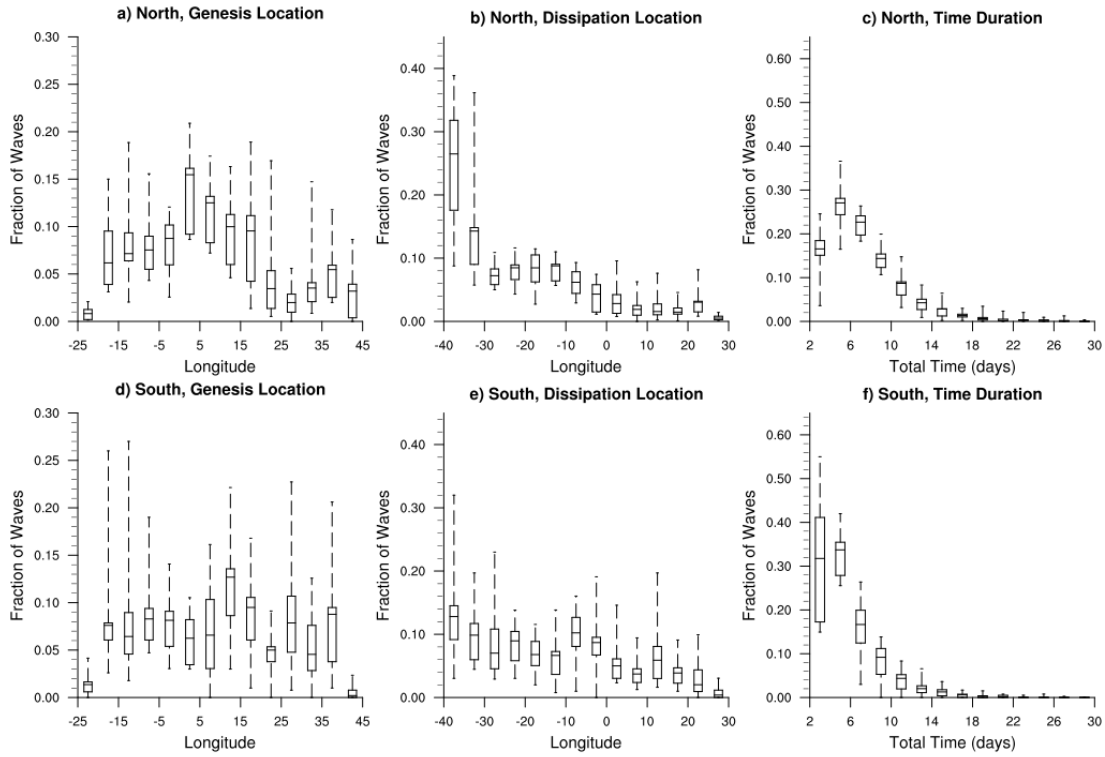



Figure D.2: Box plots of the frequency of AEW genesis (left column; a,d), dissipation (middle column; b,e), and time duration (right column; c,f) in the CMIP5 models in each 5° longitude bin, normalized by the total number of AEWs resolved by each model individually during the future period (2080-2100). Northern track values are displayed in the top row (a,b,c) with southern track values on the bottom (d,e,f).

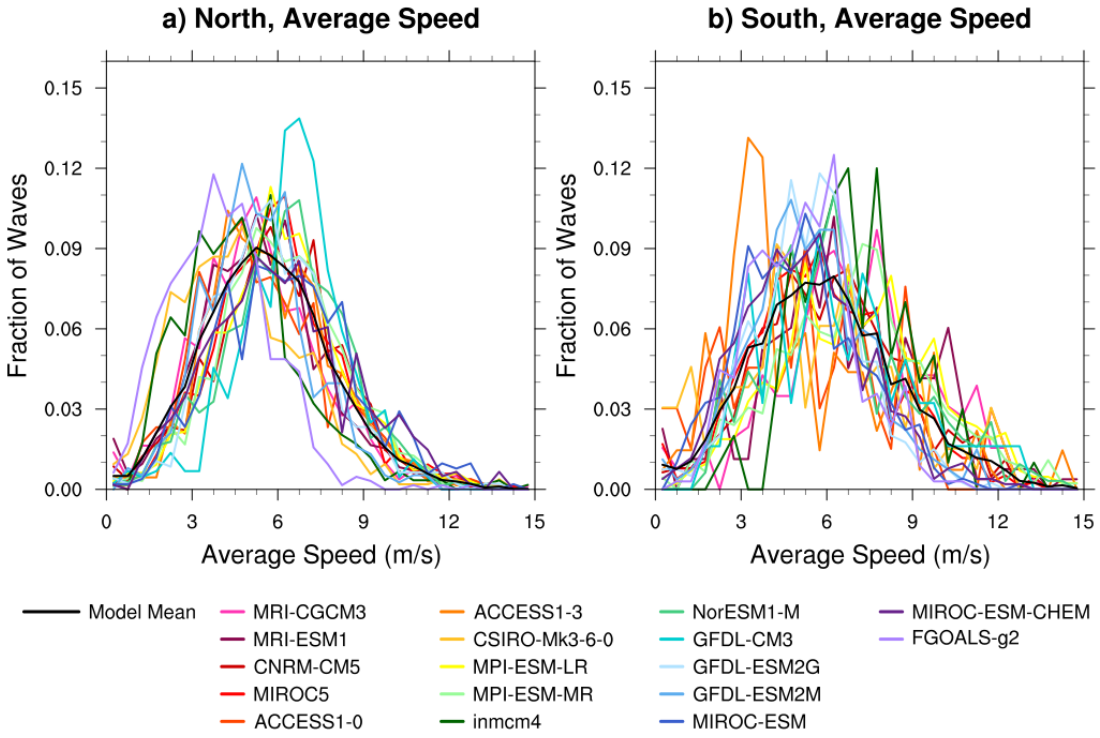



Figure D.3: Frequency of the average speed of each AEW, normalized by the total number of AEWs resolved by each model individually during the future period (2080-2100). Northern track values are displayed in (a) with southern track values in (b). Solid black line is the model mean. Colors are representative of each CMIP5 model with warm (cool) colors corresponding to finer (coarser) resolution models.

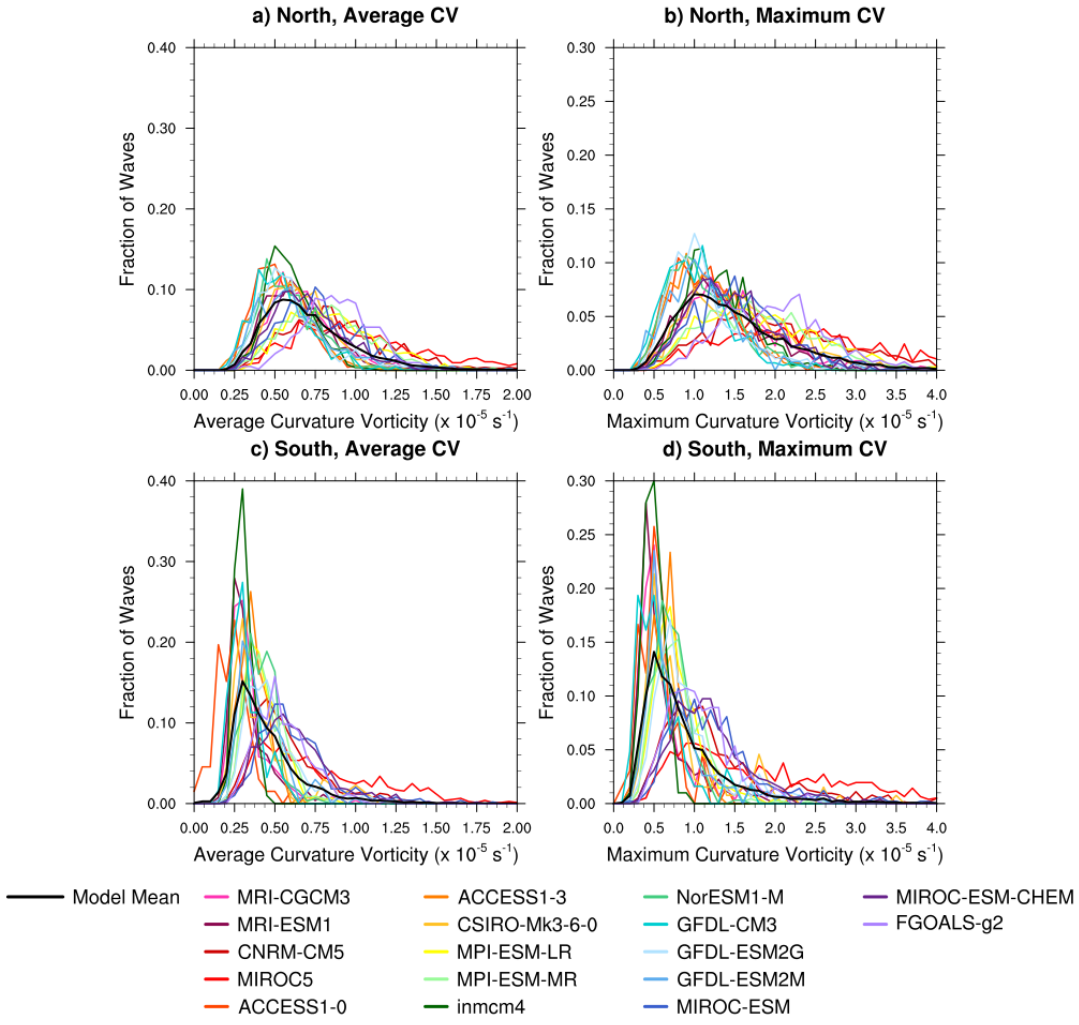



Figure D.4: Frequency of the average CV (left column; a,c) and maximum CV (right column; b,d) of each AEW, normalized by the total number of AEWs resolved by each model individually during the future period (2080-2100). Northern track values are displayed in the top row (a,b) with southern track values on the bottom (c,d). Solid black line is the model mean. Colors are representative of each CMIP5 model with warm (cool) colors corresponding to finer (coarser) resolution models.

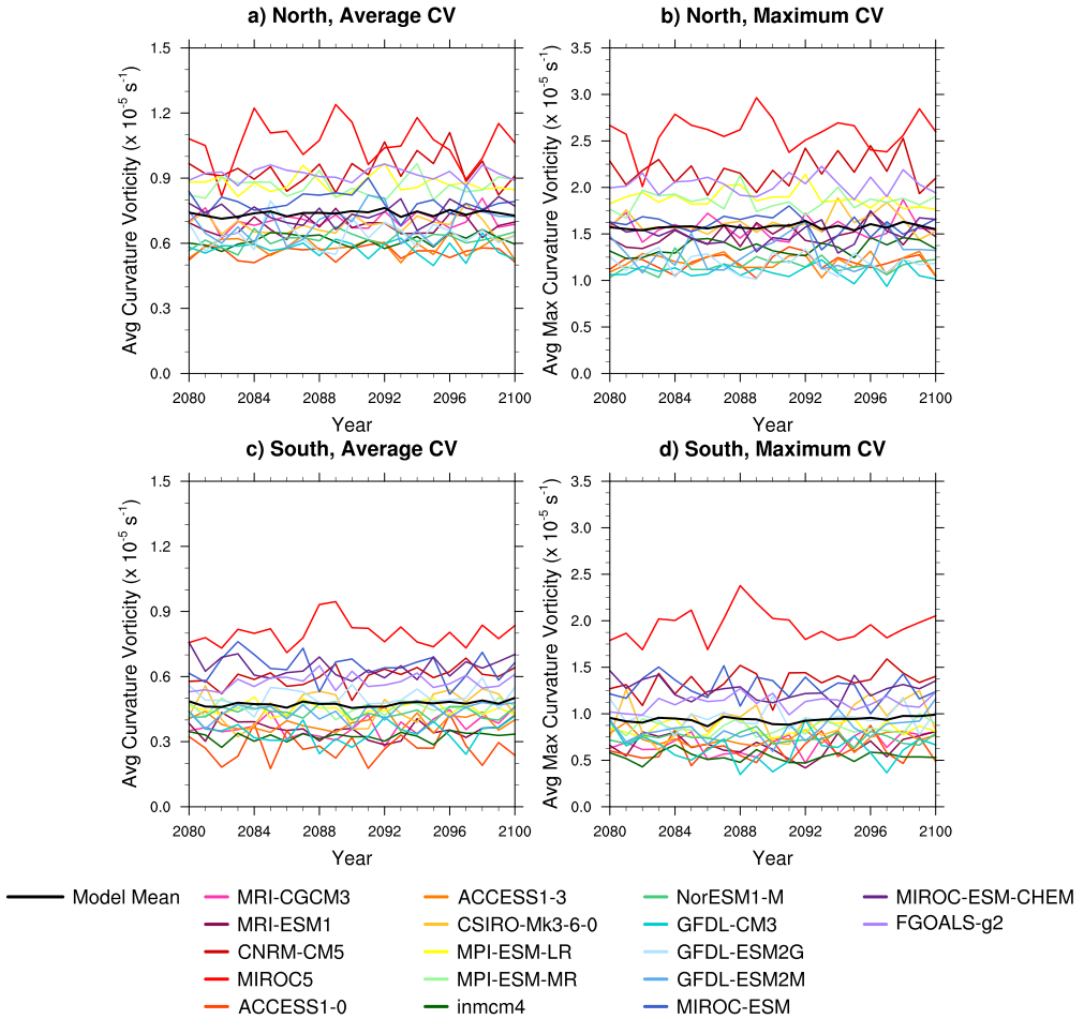



Figure D.5: Yearly average CV (left column; a,c) and yearly maximum CV (right column; b,d) of each AEW, during the future period (2080-2100). Northern track values are displayed in the top row (a,b) with southern track values on the bottom (c,d). Patterned black lines represent each reanalysis. Solid black line is the model mean. Colors are representative of each CMIP5 model with warm (cool) colors corresponding to finer (coarser) resolution models.